Inaugural-Dissertation

zur

Erlangung der Doktorwürden

der

Naturwissenschaftlich-mathematischen

Gesamtfakultät

der

Ruprechts-Karls-Universität Heidelberg

vorgelegt von

M.Sc. Désirée Sauter, geb. Schirmer

aus Nußloch

Tag der mündlichen Prüfung:

12. März 2021

PNIPAM-Containing Droplets: The Route Towards an Artificial Cytoskeleton Assembly Based on Synthetic and Natural Components

Gutachter:

Prof. Joachim P. Spatz

Physikalisch-Chemisches Institut

Ruprecht-Karls-Universität Heidelberg

Max-Planck-Institut für Medizinische Forschung

Heidelberg

Prof. (apl) Reiner Dahint

Physikalisch-Chemisches Institut

Ruprecht-Karls-Universität Heidelberg

„In der Wissenschaft gibt es nie ein Erreichen des Ziels.
In der Wissenschaft gibt es immer nur Etappenziele.“
– Henning M. Beier –

– Für meine Familie und meinen wundervollen Ehemann Eric –

ZUSAMMENFASSUNG

Obwohl Zellen die minimalen Bausteine des Lebens darstellen, weisen diese schon eine erheblich Komplexität auf. Es verwundert daher nicht, dass Forscher immer mehr dazu übergehen, reduzierte Systeme zur Erforschung und Implementierung von zellulären Prozessen in künstlichen Zellen zu verwenden. Die Konzeption solcher Systeme kann mit Hilfe der synthetischen Biologie, genauer von sogenannten *Bottom-up*-Verfahren bewerkstelligt werden. Obwohl diese Verfahren die Implementierung von zellulären Prozessen anhand von synthetischen Materialien erlauben, werden derzeit vor allem natürliche Systeme wie der Aktomyosinkomplex für die Rekonstruktion von Zellfunktionen verwendet. Obgleich dies schon eine Reduktion der Komplexität darstellt, benötigen natürliche Systeme immer noch spezialisierte Bedingungen und aufwendige Puffer. Die ultimative Reduktion der Komplexität bei der Rekonstitution von zellulären Prozessen kann deshalb nur mithilfe von synthetischen Materialien realisiert werden.

Während dieser Doktorarbeit wurde deshalb ein künstliches Zytoskelett basierend auf wärmeempfindlichen Poly(N-isopropylacrylamid) (PNIPAM) zur Implementierung von Bewegung in künstlichen Zellen etabliert. Dafür wurde zunächst ein Kompositmaterial bestehend aus PNIPAM und stäbchenförmigen Goldpartikeln hergestellt und dieses bezüglich seiner chemischen und physikalischen Eigenschaften untersucht. Im Anschluss wurde das künstliche Zytoskelettmaterial in Wasser-in-Öl Tröpfchen eingekapselt. Die Tröpfchen wurden dabei entweder durch ein selbst-synthetisiertes Tensid auf PNIPAM-Basis oder durch ein kommerziell erhältliches Fluortensid stabilisiert. Neben der Reversibilität des Phasenübergangs von PNIPAM, der sowohl im makroskopischen Gelen, als auch in Tröpfchen-basierten synthetischen Zellen gezeigt werden konnte, konnte die induzierbare Deformation der Tröpfchen aufgrund dieses Vorgangs bei Temperaturänderung nachgewiesen werden. Folglich kann eine Temperaturerhöhung zur kontrollierten Manipulation der Tröpfchen genutzt werden. Zusätzlich wurde das implementierte Zytoskelettmaterial in Kombination mit fluorophilen Oberflächen, die zu erhöhter Oberflächen-Tröpfchen Reibung führten, verwendet, um die Migration von asymmetrischen Tröpfchen gezielt zu stimulieren.

Die Herstellung dieser die Zellpolarisation nachahmenden Tröpfchen wurde dabei durch die gezielte Fusion von stabilen und instabilen Tröpfchen während der Polymerisation erreicht. Im Anschluss an die Untersuchung der PNIPAM-induzierten Tröpfchenmigration, wurde das künstliche Zytoskelettmaterial mit dem natürlichen Zytoskelettprotein Aktin durch einen sequenziellen Pico-Injektionsansatz in Emulsionströpfchen erstmalig kombiniert und somit die Biokompatibilität des implementierten Systems gezeigt.

Durch das implementierte künstliche Zytoskelett konnte mittels der Kontrolle der Phasenübergangsprozesse von PNIPAM die Mobilität der Tröpfchen-basierten synthetischen Zellen durch deren dynamische Verformung erreicht werden. Zusätzlich konnte die Biokompatibilität des Systems durch die Kombination von natürlichen und synthetischen Zytoskelettkomponenten gezeigt werden. Die Toleranz des PNIPAM-Systems auch gegenüber spezialisierten Puffersystemen könnte die Bandbreite des *Bottom-up*-Werkzeugkastens der synthetischen Biologie erweitern und den Aufbau hybrider zellulärer Module verbessern. Daher stellt der entwickelte Ansatz einen wichtigen Meilenstein in der Entwicklung von *Bottom-up*-Anwendungen in der synthetischen Biologie dar.

Abstract

Although cells represent the smallest building blocks of life, they are already exhibiting a high level of complexity. It is therefore not surprising that researchers tend to utilize simplified systems for investigating, but also reconstituting, cellular processes in artificially constructed cells. The conception of those artificial cells can be done using bottom-up biological approaches. Currently, the reconstitution of cellular process is achieved using natural or nature-derived components like the actomyosin-complex for the reconstitution of cellular motility. Although a reduction of complexity can be accomplished in this way, natural systems still require specialized conditions and sophisticated buffers. Ultimately, the reduction of complexity can only be realized by the reconstitution of cellular processes using completely synthetic materials.

In this thesis, a completely artificial cytoskeleton based on thermo-responsive poly(N-isopropylacrylamide) (PNIPAM) to trigger motility of synthetic cells was established. To this end, a PNIPAM-based composite material containing gold nanorods was generated and its physiochemical behavior was characterized. The composite material was introduced and assembled inside water-in-oil emulsion droplets that have been stabilized by either a custom-made PNIPAM-containing surfactant (PNS) or a commercially available fluorosurfactant (CS). Besides the reversibility of the PNIPAM phase transition in bulk and droplet-based synthetic cells, the on-demand inducible deformation of droplets due to this phase transition was shown. Additionally, droplet migration was triggered using asymmetric PNIPAM-containing droplets in combination with fluorophilic-coated surfaces. The production of those cell polarization-mimicking droplets was achieved via targeted fusion of stable and unstable droplets during polymerization. Following the assessment of PNIPAM-mediated droplet motility, for the first time, the artificial cytoskeleton material was combined with the natural cytoskeleton protein actin by a sequential pico-injection approach thus elucidating the biocompatibility of the presented system.

Herein, a versatile PNIPAM-based artificial cytoskeleton for synthetic cell applications was designed and implemented.

The control over the PNIPAM volume transition processes allowed to achieve the motility of the droplet-based synthetic cells by their dynamic deformation. The biocompatibility of the system by combining natural and synthetic cytoskeleton components could be shown. The tolerance of the PNIPAM system also towards specialized buffer systems, might expand the bandwidth of the bottom-up synthetic biology tool kit, enhancing the assembly of hybrid cellular modules. Therefore, the developed approach represents an important milestone in the development of bottom-up synthetic biology applications.

TABLE OF CONTENT

Introduction and Motivation

1 Introduction

1.1 General Introduction to (Synthetic) Life

Life is a highly complex phenomenon and definitions of life are controversially discussed amongst different research groups [1]. If one is looking for the definition of life in an encyclopedia, following definition can be found:

> *"Life, living matter and, as such, matter that shows certain attributes that include responsiveness, growth, metabolism, energy transformation, and reproduction. […] Life comprises individuals, living beings, assignable to groups (taxa). Each individual is composed of one or more minimal living units, called cells, and is capable of transformation of carbon-based and other compounds (metabolism), growth, and participation in reproductive acts."* [2]

Already at least 3.77 billion years ago life emerged on Earth which can be evidenced in forms of fossilized microorganisms found in hydrothermal vent precipitates [3]. Although there are general ideas *when* life emerged on this planet and how it should be defined, the more interesting question *how* life evolved on earth is still not fully understood. Nevertheless, scientists do agree that very specialized environmental conditions were required for the formation of first organic building blocks and therefore the creation of life on earth [4]. Although much is already known about life in general and the minimal living units, the cells, the creation of living material from synthetic matter from scratch in the laboratory is still not achieved to the present day. Nevertheless, great achievements in terms of compartmentalization, metabolic activity, informational control or establishing cell-like functions in synthetic cells using natural components such as lipids, cytoskeleton proteins or DNA have been made in the last decades using bottom-up synthetic biology [5]. Though, all of these approaches have the use of natural or nature-derived components in common, which not only require specialized and very precise conditions, but also contradicts how life evolve from inanimate matter.

Therefore, to overcome the restrictions of natural systems, I aimed for the reconstitution of cellular functions using completely synthetic materials. Additionally, I showed the assembly of hybrid synthetic cells comprised of synthetic and natural components. In the following, the basic concepts of natural and synthetic cells, as well as used materials, methods and theoretical backgrounds are depicted in more detail.

1.2 Living Cells: The Complexity of the Minimal Building Blocks of Life

In the following sections, I will describe some of the basic structures and functions of the natural cellular system with a particular focus on eukaryotic cells and their cytoskeleton.

1.2.1 Structure of the Eukaryotic Cell

By definition, eukaryotic cells separate their genetic information from the cytoplasm and keep their DNA in an internal compartment called nucleus, which is surrounded by a double-layered membrane which is commonly called nuclear envelop (**Figure 1.1**) [6]. Besides the nucleus, several other membrane-enclosed structures are present in the eukaryotic cell that are among others responsible for the synthesis of proteins, the supply of energy or the digestion of compounds that are no longer useful or harmful for the cell.

Furthermore, eukaryotic cells exhibit a large network of protein filaments crossing through the cytoplasm, which together with attached proteins form a system of ropes and motors that gives the cell its mechanical stability, controls the shape and is responsible for the motion of the cell [6]. These cytoskeleton proteins are also accompanied by specialized protein complexes forming contacts to the extracellular environment by forming contacts to the extracellular matrix (ECM) or other cells.

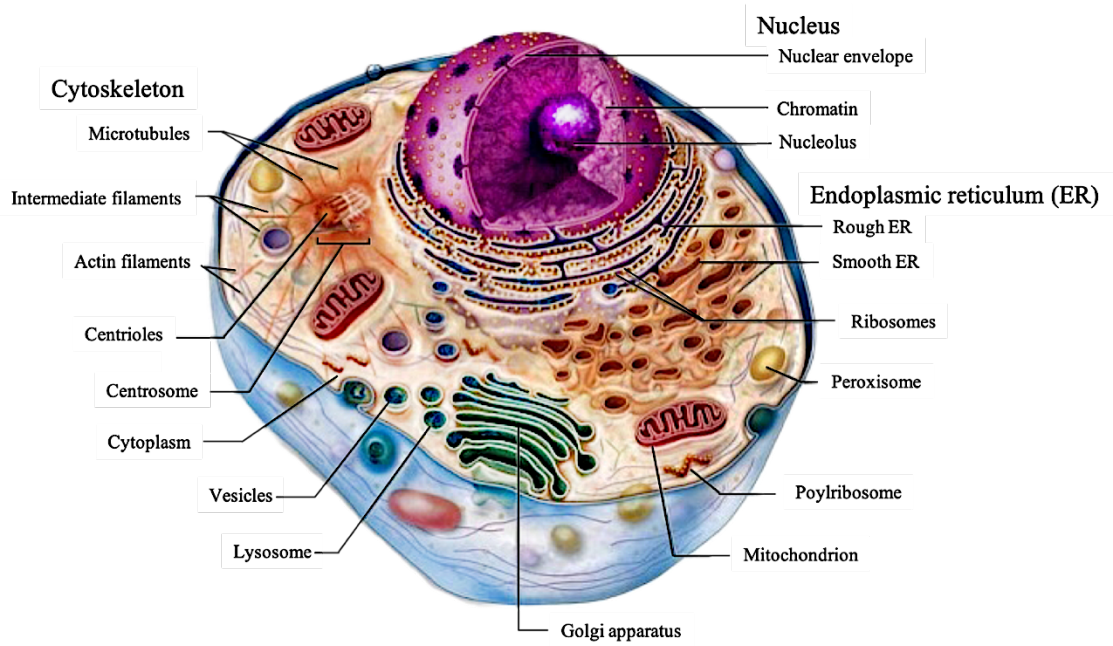

FIGURE 1.1 *SCHEMATIC ILLUSTRATION OF AN EUKARYOTIC CELL*
The eukaryotic cell is surrounded by a plasma membrane which separates the cytoplasm from the extracellular environment. Within the cell, several highly organized and specialized compartments like the nucleus, the endoplasmic reticulum, the Golgi apparatus or mitochondria are present. Besides that, a cell crisscrossing filament network, the cytoskeleton, which is responsible for the structure and motion of the cell is included within the cell cytoplasm. Adapted and modified from [137].

Besides the already complex inner architecture of a single cell, cells form tissues and organs in multicellular organisms to facilitate complex biological processes. To do so, cells constantly undergo dynamic rearrangements and establish stable cell-cell contacts to adapt to their environment. This rearrangement is accomplished by the dynamic polymerization and depolymerization of cytoskeleton polymers, which are described in the next section in more detail.

1.2.2 CYTOSKELETON ASSEMBLY

Within the cytoplasm of the eukaryotic cell, different protein filaments form a distinctive network responsible for the mechanical properties and responses of the cell. This filament network is called the cytoskeleton and is, in case of an eukaryotic cell, comprised of three cytoskeleton polymers – actin filaments, intermediate filaments and microtubules (**Figure 1.2**) whereby actin and tubulin are additionally accompanied by motor proteins [7]. Both actin and intermediate filaments can be found throughout the cell, with actin filaments mainly located around the cell periphery in the cortex underlying the plasma membrane and in stress fibers [8] and intermediate filaments in the perinuclear region from

which they spread towards the cell surface anchoring to cell-cell or cell-extracellular matrix (ECM) junctions [9]. Microtubules are comprised of long, stiff polymers and form a network radiating from the centrosome or the microtubule-organizing center (MTOC) to the edge of the cell [7]. Besides the intermediate filaments, the two other cytoskeleton polymers are polar and provide tracks for molecular motor proteins [10], while the intermediate filaments are rather transported by the motor proteins [11].

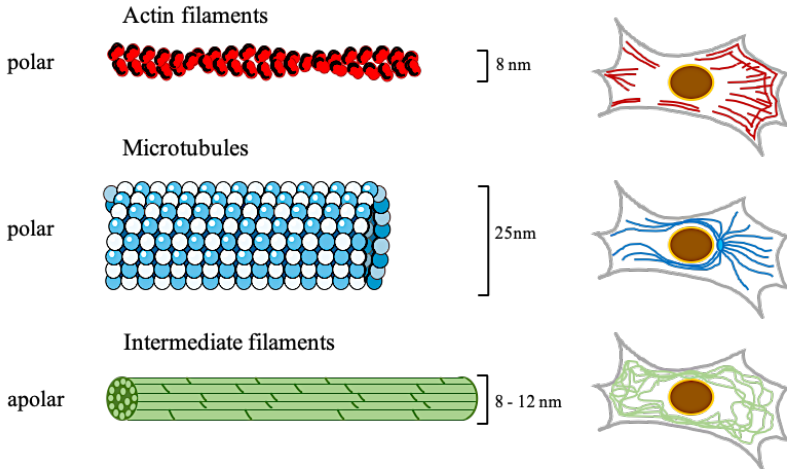

FIGURE 1.2 *CYTOSKELETON PROTEINS AND THEIR DISTRIBUTION IN THE CELL*
Architecture and distribution of the three cytoskeleton-forming proteins within the cell. Actin fibers (red) are helical flexible polymer structures that can form linear bundles or two-dimensional networks. Although actin fibers are widely distributed within the cell, actin is mostly found in the cortex underlaying the plasma membrane and in stress fibers [6]. Microtubules (blue) are rigid, hollow protein cylinders made out of α- and β-tubulin. The centrosome, which is located adjacent to the nucleus serves as the initiation point of microtubule formation [14]. Intermediate filaments (green) are rope-like structures comprised of intermediate filament proteins. They can either be located beneath the nuclear membrane or extend across the cytoplasm, giving cells their mechanical strength, which is important for intracellular transport processes and cell division [6]. Adapted and modified from [6].

1.2.2.1 ACTIN FILAMENTS

Actin filaments are formed by polymerization of globular actin monomers (G-actin) into long fibers (F-actin) that form a helical structure with a width of around 8 nm (**Figure 1.2**). The polymerization of G-actin is happening primarily at the barbed (+)-end of the filament in an adenosine triphosphate (ATP)- and Mg^{2+}-dependent manner while depolymerization is mainly occurring at the pointed (-)-end (**Figure 1.3**) [138]. In vitro, this treadmilling process is caused by different affinities of ATP- and ADP-loaded G-actin monomers to the filament structure. ADP-loaded G-actin monomers with a lower binding affinity are hereby generated during the incorporation of ATP-loaded G-actin with subsequent ATP hydrolysis . However, if the exchange of ADP with ATP is happening constantly due to a sufficient amount of G-actin, polymerization is occurring with different

rates at both sides, even though the barbed ends have a higher affinity to G-actin. Although if a critical concentration is reached, actin filaments are only growing at the barbed end, while depolymerization is taken place at the pointed end with the same rate [139].

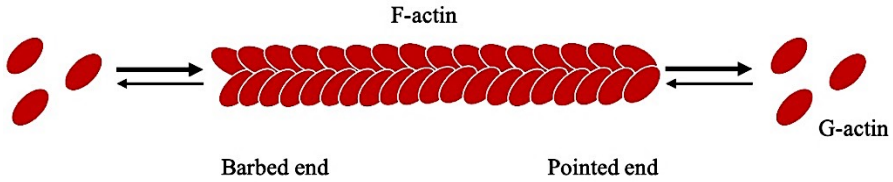

FIGURE 1.3 *POLYMERIZATION PATTERN OF ACTIN FILAMENTS*
Actin is forming filamentous structures by polymerization of G-actin in an ATP consuming process. The actin polymerization *in vivo* and *in vitro* is hereby mainly occurring at the barbed end [6].

Contractility of the actin network is induced by sliding of actin filaments and myosin motors and is used for many processes within the cell including organization of the extracellular matrix, migration or cell-shape changes [8]. The myosin superfamily is a large and diverse protein family that can be group in many classes. Myosins are the only known actin-based motor proteins [12]. Most myosin proteins can be assigned to class II and make up the major contractile proteins of cardiac, smooth and skeletal muscles. Importantly, those myosin II proteins that resemble their muscle counterpart are also presented in every eukaryotic non-muscular cell [13]. Non-muscular myosin II forms dimers that assemble into bipolar filaments. Those filaments bind F-actin in a distinct orientation through their head domain and the ATPase activity of the head domain is leading to conformational changes that are contracting actin filaments in an anti-parallel manner [140]. In order to translate this contraction into cell motility, the force generated by the cell needs to be transferred onto the substrate by cell-substrate contacts. The cell-moving machinery is therefore comprised of two self-assembling molecular systems, the actin cytoskeleton as force-producing engine and the cell-adhesions - multimolecular complexes spanning the plasma membrane and mediating a mechanical link between the cytoskeleton and the extracellular substrate [26].

The migration process of cells can hereby divided into four steps: first the formation of protrusions on the leading edge of the cells, followed by the adhesion to the ECM, the generation of traction stresses against the formed adhesions and ultimately the release of rear adhesions and cell body contraction [142]. Besides dramatic changes in cell

morphology, an effective spatiotemporal control over adhesion sites, F-actin assembly and disassembly and various different signaling molecules like the Rho family GTPases are required [143]. Focal adhesion (FA) sites represent hereby the anchoring points for contacts between cells and the ECM [184]. Those FAs are comprised of clustered integrins, which are transmembrane receptors that interact with multivalent adhesive ECM proteins on the outside of the cell and the cytoskeleton on the inside [185].

1.2.2.2 Microtubules

Like actin filaments, microtubules are built from compact, globular subunits forming a helical structure with two distinct ends (**Figure 1.2**). Also in the case of microtubules, the subgroups are asymmetrical and bind in a head-to-tail arrangement to each other. In contrast to actin, microtubules are consisting of two globular subunits, α- and β-tubulin, which are assembling into a heterodimer that is further polymerized into protofilaments upon guanosine triphosphate (GTP) hydrolysis (**Figure 1.4**) [14]. To provide both strength and adaptability, microtubules are built of thirteen protofilaments that are forming a hollow cylinder with a diameter of 25 nm that can resist thermal breakage [6].

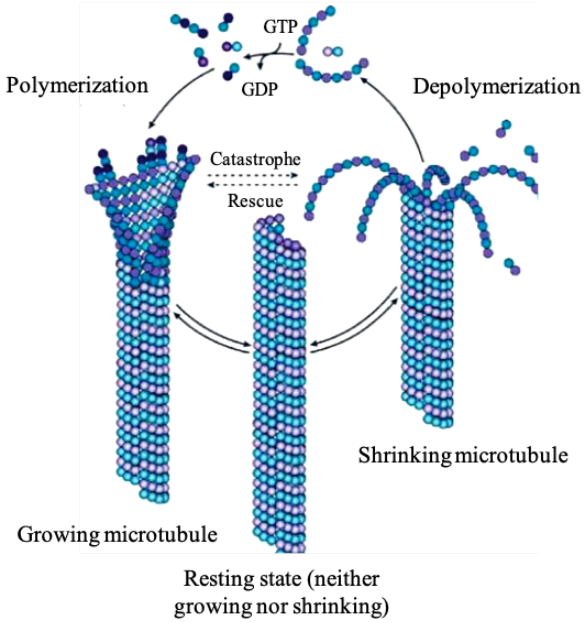

Figure 1.4 *Microtubule Formation and Depolymerization*
Microtubules are composed of α- and β- subunits which are shown in blue and violet, respectively. The subunits are forming a heterodimer which is than polymerized into linear protofilaments. Thirteen of these filaments are than forming a hollow cylinder. The polymerization process is powered by GTP hydrolysis [14]. Adapted and modified from [15].

Based on their structure, microtubules are more rigid than actin filaments thus functioning as highways for motor protein-mediated transport of cargo through the cell. The motor proteins kinesin and dynein are thereby walking along the protofilaments in opposed directions, dynein to the (-)- end and kinesin mostly to the (+)-end [7], except some kinesin motor proteins in budding yeast cells which can move bidirectional [186]. These motor proteins are powered by the hydrolysis of ATP.

1.2.2.3 Intermediate Filaments

In contrast to actin filaments and microtubules, intermediate filaments do not participate in cell movement or cargo transport but play a fundamental role in providing mechanical strength to cells and tissues [14]. Contrary to actin filaments and microtubules, the polymerization process of intermediate filaments starts with the formation of tetramers (**Figure 1.5**). For the formation of a unit-length filament, eight tetramers assemble and several of those unit-length filaments interact end-to-end to form the mature filaments [7].

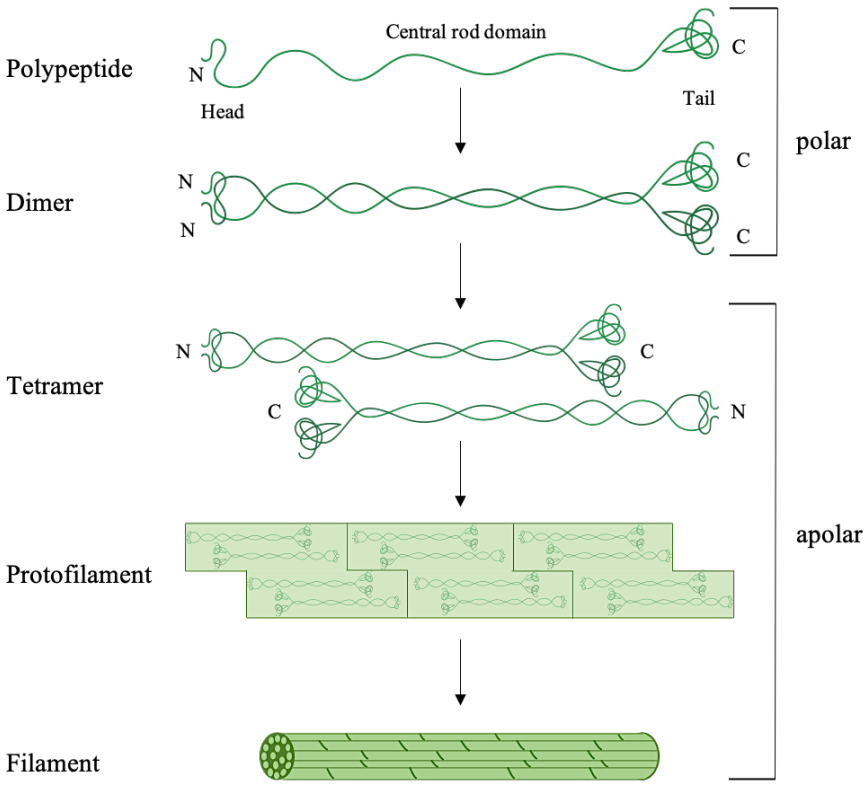

Figure 1.5 *Assembly of Intermediate Filaments*
The formation of intermediate filaments is grouped in several steps. First, the central rod domains of two polypeptides forming a coiled-coil structured dimer. Those dimers than associate in an anti-parallel manner to form tetramers. The tetramers assemble end-to-end to form protofilaments and laterally the mature filaments. Adapted and modified from [14].

Since the tetramers are already formed in an anti-parallel manner, the resulting filaments are apolar, in contrast to actin filaments and microtubules that have a distinct plus or minus end. Intermediate filaments form an elaborate network within the cytoplasm providing the mechanical integrity of the cell [141].

Although only the cytoskeletal components of a eukaryotic cell were highlighted in more detail, the complexity of a cell and the interplay between many different functional units could be illustrated. This remarkable cellular complexity and the associated inability to study the effect or role of specific parts within, forced scientists into turning their attention to artificial cells as substitutes. Therefore, the different approaches of producing synthetic cells and their application will be examined in more detail in the following section.

1.3 Artificial Cells – Synthetic Compartments with a Variety of Applications

Artificial cells are cell-like analogues that possess certain properties of natural cells. They can be engineered using synthetic biology approaches. Synthetic biology describes hereby a multidisciplinary field of research that aims for the creation of new biological systems or the redesign of already known biological processes. To achieve this, various aspects of materials science, molecular biology, chemistry, biotechnology, genetic engineering and other disciplines will be brought together [144]. Since artificial cells are minimal and well-defined systems, they can be used to study and understand natural biophysical dynamics with slight interference from natural complexity [16]. Besides the implementation as highly controllable substitute for natural cells, the applications of artificial cells can be extended into the field of pharmaceutics and biotechnology with applications in drug delivery [17, 18], as blood cell substitute [19, 20], for gene therapy [21], the treatment of enzyme defects [22], for diagnostics [23, 24], fundamental research and many more [25]. The definition of artificial cells is not strict within the field, in the following section the classification is therefore based on their intrinsic characteristics [27].

1.3.1 Classification of Artificial Cells

Based on their intrinsic characteristics, artificial cells can be classified into two groups – typical and non-typical artificial cells.

1.3.1.1 Typical Artificial Cells

Typical artificial cells are comprised of natural components, exhibit cell-like structures and at least some of the key features of a natural cell, meaning they can either self-reproduce, have a metabolism or can evolve [27]. Additionally, they have a membrane and can interact with their environment in a dynamic manner [28]. Despite a lot of efforts, the integration of all these characteristics into one artificial cell has not yet been accomplished. However, the integration of several simplified characteristics have been achieved so far [28]. Still, the research on this particular type of synthetic cell is quite promising since it might provide ways not only for a better understanding of cellular processes but might also be able to achieve a connection between living and non-living material ultimately creating life.

1.3.1.2 Non-Typical Artificial Cells

On the other hand, non-typical artificial cells are engineered materials mimicking one or more features of a natural cell [27]. They can imitate surface characteristics, functions or the shape of a natural cell [29]. Natural components are often used to implement the cell-like functions in the artificial cells. But also synthetic analogues like amphiphilic polymers and surfactants as lipid substitute [30], micro- and nano-particles [31] or capsules as cell bodies are used [32, 33].

Independent of the classification and type of synthetic cells, there are two main approaches for the production of synthetic cells: the top-down and the bottom-up approach [34]. Both approaches are discussed in more detail below.

1.3.2 Synthetic Biological Approaches for the Production of Artificial Cells

1.3.2.1 Top-Down Approach

The construction of artificial cells using the top-down approach is accomplished by the reduction of the complexity of an initial system [35]. This means that for example the genome of a cell of interested is reduced in such a way that the genes of interest are still maintained while all others genes are knocked-out. Also the formation of a synthetically constructed genome such as plasmids and the introduction into an artificial cell is part of the top-down approach [36]. Independent of the type of genome, either naturally or synthetically constructed, the minimal system needed is highly dependent on the environment, meaning that all components that can no longer be synthesized by the artificial cell itself need to be provided [27]. So far, only minimal organisms like bacteria or viruses were constructed in this way, whereas minimal eukaryotic cells have not be built yet due to their higher complexity [27]. Nevertheless, also the construction of more complex organism might be possible in the future using the top-down approach.

1.3.2.2 Bottom-Up Approach

In contrast to the top-down approach described before, the bottom-up approach is aiming to create an artificial cell from scratch using non-biotic components [37]. This approach is accompanied by an increase in terms of complexity in a step-by-step procedure. An advantage of this method is the fact that, in addition to natural components like proteins or cytoskeleton complexes, synthetic materials [38, 39] and semisynthetic materials like DNA origami [40, 41] can also be used to establish functions in the artificial cell, which leads to an increase in flexibility when it comes to manufacturing an artificial cell. It is therefore not surprising that a large number of artificial cells have already been produced using this method [27, 145, 146, 147]. Nevertheless, the field is still in its infancy but might be the key for the construction of life in the laboratory. Since also life has evolved from non-living matter, the bottom-up approach might function as bridge between the animate and inanimate matter allowing for the understanding of the origin of life [27]. A graphical comparison of both described approaches is shown in **Figure 1.6**.

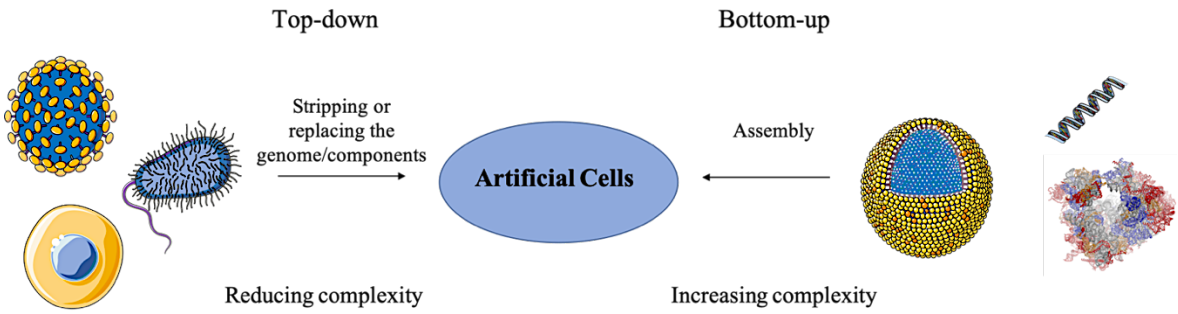

Figure 1.6 *Graphical Illustration of the Top-Down and Bottom-Up Approach*
While the top-down approach is using natural systems and reducing the complexity by stripping or replacing the genome or other components of a cell to create minimal artificial cells, the bottom-up approach is constructing minimal cells from scratch using natural or synthetic components to implement cell-like functions. Both approaches can be used in a complementary manner for the construction and understanding of life. Adapted and modified from [27].

Within this thesis, bottom-up synthetic biology was used to implement an artificial cytoskeleton for synthetic cell applications based on a thermosensitive hydrogel material. In the following, the characteristics and compositions of hydrogels are shown in more detail with a focus on stimuli-responsive gels.

1.4 Hydrogels – Three-Dimensional Solvent-Infused Polymer Networks

Hydrogels are a unique class of three-dimensional crosslinked polymeric networks [42]. They exhibit uncommon physical properties such as viscosity, density, elasticity and volume, which can be dramatically changed based on temperature, solvent characteristics or polymer chain [43]. Hydrogels consist of crosslinked hydrophilic polymer chains with the capacity of binding large amounts of water without dissolving [51]. This makes them suitable for various applications in the fields of drug delivery [44, 45], diagnostics [46], tissue engineering [47, 48], wound healing [49], as actuators [50], in fundamental research or other medical/biological fields [148, 149, 150]. Besides their interesting properties with liquid-like behavior on the molecular length scale and solid-like behavior in the macroscopic range [62], hydrogels can be tuned in a wide range, for example, when it comes to composition, crosslinking, size, functionalization or mechanical properties [52]. The classification of hydrogels is depicted in more detail in the following section.

1.4.1 Classification of Hydrogels

Hydrogels are an interesting class of materials, which can be fine-tuned in various ways. However, since they can be modulated over a wide range of criteria, they are classified according to distinct criteria. A potential scheme of classification is shown in **Figure 1.7**.

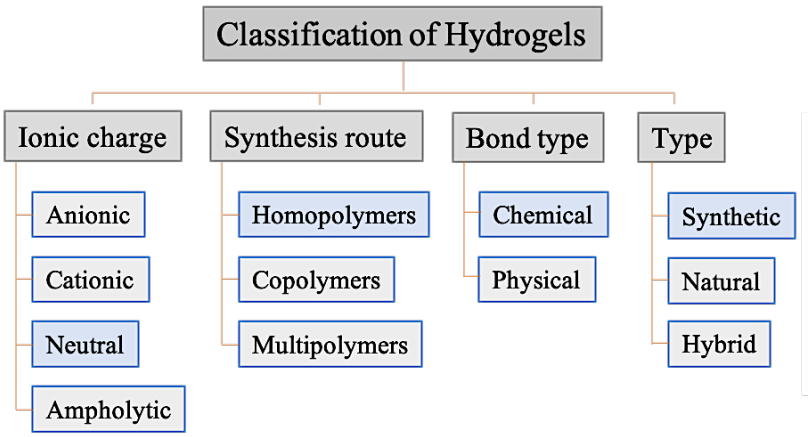

Figure 1.7 *Parameter-Based Classification of Hydrogels*
Mapping and arrangement of some hydrogel characteristics. Characteristics describing used PNIPAM-based hydrogel material are depicted with a blue box, while the other characteristics are shown in grey. Adapted and modified from [42].

1.4.1.1 Ionic Charge

Based on the incorporation of negatively or positively charged, uncharged or zwitterionic molecules into the polymer network structure, hydrogels with a different overall net charge can be prepared. Although neutral and ampholytic polymers might possess the same net charge, the gels do show different behavior, regarding for example swelling rates [53].

1.4.1.2 Synthesis Route

Dependent on the number of different monomer units used for the fabrication, homo-, co- or multi-polymer hydrogels can be obtained. While homopolymeric hydrogels are comprised of only one species of hydrophilic monomers [54], copolymers are composed of two or more different monomeric units that are arranged in a random, block or alternating manner [55]. In contrast, multipolymer hydrogels are made of two independent polymeric networks contained in an interpenetrating associate [56, 57]. It

should be noted that at least one of these independent polymer networks must be crosslinked in order to be classified as multipolymeric hydrogel system [52].

1.4.1.3 Bond Type

Hydrogels are formed by crosslinking of the polymeric chain to prevent dissolving. Based on the nature of the formed bonds, the gels can be divided in chemically or physically crosslinked networks [57]. While chemically linked hydrogels exhibit covalent bonds, physical crosslinked gels possess transient linkage that can be formed by hydrogen bonds, ionic or hydrophobic interactions [52].

1.4.1.4 Type

Besides the crosslinking, the number of different monomers or the net charge of the formed hydrogels, also the source of the used materials is suitable as classification model [58]. In this case, a distinction is made between natural and synthetic components. Many natural components are, for example, sugars like chitosan, dextran or hyaluronic acid, but also proteins like collagen, gelatin or fibrin or even DNA can be used for the fabrication of hydrogels [42]. Synthetic hydrogels are often formed using precursors containing double bonds that are polymerized in a radical polymerization process. But also non-radical reactions like the reaction between different functional groups can be used for the assembly of hydrogels.

In the presented work, crosslinked poly-(N-isopropylacrylamide) (PNIPAM) gels were produced by free-radical polymerization, a specific type of chain-growth polymerization. The different chain extension polymerization methods are therefore listed in more detail below.

1.4.2 Chain-Growth Polymerization Techniques

The preparation of hydrogels is a combined process between the formation of the polymer chains from monomers and their crosslinking to form the network. This can be achieved using chain-growth methods that can be divided into free-radical or radical addition, anionic, cationic or coordination polymerization [59].

1.4.2.1 Free-Radical Polymerization

A wide variety of unsaturated organic compounds can be polymerized to high molecular weight polymers by means of radical polymerization. A scheme of the polymerization mechanism by the example of the underlying NIPAM polymerization is shown in **Figure 1.8**.

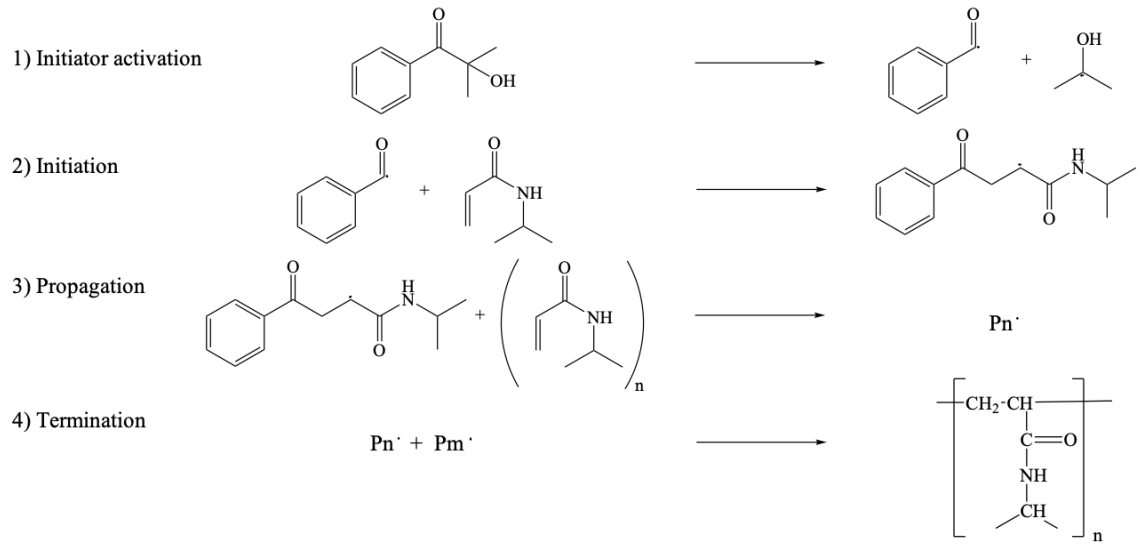

Figure 1.8 *NIPAM Polymerization*
NIPAM polymerization is following a free-radical polymerization mechanism. The advantage of this method is a wide compatibility with a variety of conditions. However, the stereo control of the resulting polymers is difficult or impossible to control.

The polymerization starts by the generation of radicals through decomposition of an initiator molecule (1). The initiator activation can be accomplished using different methods like thermal decomposition, redox reactions, ionizing radiation, persulfate dissociation or photolysis [60]. The activated initiator can then react with the monomers in the fast occurring initiation (2) and propagation (3) steps. At some point, the polymerization process gets terminated (4) either by the combination or disproportionation of radicals or the reaction with unrelated molecules like solvent molecules. Generally, the whole process between initiation and termination is quite fast and varies in the range of around one second [59]. Despite the relatively simple model of the reaction processes, it can be seen that several variable steps are included in the process leading to polydisperse polymerization products with hardly controllable polymer weight or structure distributions [59].

1.4.2.2 Ionic and Coordination Polymerization

Ionic addition polymerization involves the polymerization of monomers using either anionic or cationic initiator molecules. Although not as widely used as the free-radical polymerization approach, ionic polymerization has some relevance even for the large-scale production of for examples tires or grease additives [59] since the resulting product is much more controllable.

Coordination polymerization is using transition metal salts or complexes to catalyze the polymerization process [59]. One of the most prominent coordination polymerization methods is the heterogeneous Ziegler-Natta polymerization where titanium tetrachloride is used as catalyst and magnesium chloride as support [61].

Nevertheless, not every polymerization method is suitable for every monomer. Therefore, the polymerization method always needs to be adjusted to the used compounds.

1.5 Stimuli-Responsive Polymer Gels

Hydrogels can respond to a wide range of external stimuli by a change of shape/size or changes in their optical, electric or mechanical properties [62]. The nature of the stimulus can hereby be classified as physical (influences the systems molecular interaction) or chemical/biological (directly affects the interactions between the polymer chains or with other components) [62]. Potential stimuli to trigger polymer transition are for instance pH [63], mechanical force [64], electric/magnetic fields [65, 66, 67], enzymes [69], light [70] or temperature [68].

During the last decades, stimuli-responsive hydrogels are of utmost interest among researchers. It is therefore not surprising that the number of publications on this class of materials is constantly increasing. Therefore, selected types of stimuli-responsive (smart) hydrogel systems are introduced here in more detail.

1.5.1 Thermo-Responsive Hydrogels

Thermo-responsive hydrogels are likely the most investigated stimuli-responsive gel materials [42]. Since temperature is easy to regulate, these hydrogels can be used for *in*

vitro, as well as *in vivo* studies [62]. Upon stimulation, thermo-responsive polymer gels show a temperature-dependent swelling behavior, which can be divided into positive or negative temperature response. A positive temperature sensitivity hereby means an increase in swelling with rising temperature, while a negative temperature sensitivity is causing the opposite behavior, namely the shrinkage of the material [71]. The temperature upon which this change occurs is the so-called critical solution temperature or volume phase transition temperature involving a change in the phase between polymer and solvent within the system [62]. This change can either take place below the critical temperature, i.e. the system has an upper critical solution temperature (UCST), or above it (lower critical solution temperature (LCST)). In some cases also both behaviors can be observed.

1.5.1.1 Upper Critical Solution Temperature (UCST)

The upper critical solution temperature (UCST) is described as the temperature above which the components of a system are miscible in every rate [73]. In case of polymers exhibiting UCST behavior, the thermos-responsiveness mainly depends on strong supramolecular interactions between the side groups of the respective polymer that are easily influenced by the solvent, the polymer concentration and molecular weight, as well as salts [72].

1.5.1.2 Lower Critical Solution Temperature (LCST)

In contrast to the UCST, the lower critical solution temperature (LCST) is defined as the temperature above which the components of a system are not miscible in every composition anymore or as the minimum of the binodal of the phase diagram (**Figure 1.9**) [74]. Among thermo-responsive polymers, those exhibiting a LCST behavior are the most studied [72] because of their temperature-induced transition from hydrophilic to hydrophobic [74]. During this transition, the hydrogen bonds formed between the side groups of the polymer chain and the water molecules get weakened, following by partial dehydration of the polymer chains and aggregation. This effect can be explained based on the Gibbs free energy term (**eq. 1.1**). The interactions between water molecules and the polymer chains are leading to a favorable enthalpy of mixing but a less favorable entropy of mixing due to a higher degree of organization resulting in a net negative free energy and a spontaneous mixture of the polymer and water. Upon temperature increase, the entropy

term becomes predominant resulting in a positive net free energy and therefore a demixing of the polymer and solvent [74].

$$\Delta G_{mix} = \Delta H_{mix} - T\Delta S_{mix} \qquad \text{(eq. 1.1)}$$
$$T < LCST : \Delta G_{mix} < 0 \; ; T > LCST : \Delta G_{mix} > 0$$

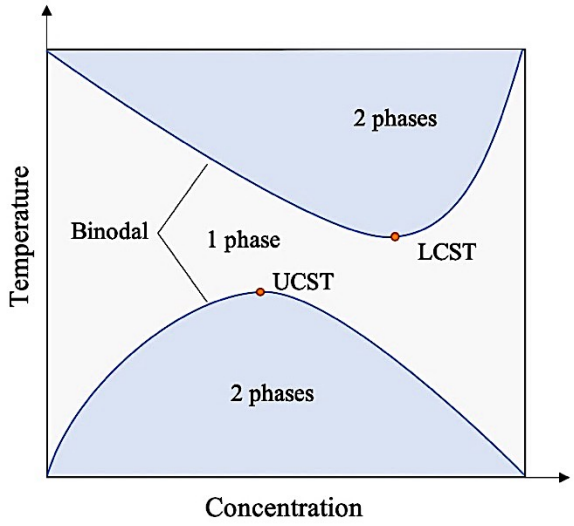

FIGURE 1.9 *PHASE DIAGRAM OF A BINARY MIXTURE*
The phase diagram is showing the UCST (maximum of the binodal) and the LCST point (minimum of the binodal) of a thermo-responsive polymer. Adapted and modified from [72].

Accordingly, the LCST behavior of thermo-responsive polymers is an entropy-driven process upon which the polymer is changing its structure from a coil to a globular state. This is leading to the minimization of interactions between the hydrophilic polymer and the water molecules thus favoring the expulsion of water from the polymer structure.

1.5.1.3 CLOUD POINT OR PHASE TRANSITION TEMPERATURE

Although often used interchangeably with the LCST, the phase transition temperature T_T, refers to temperature correlated to a specific polymer concentration at which the phase transition and therefore a clouding of the solution is happening. In contrast, the LCST is representing the minimal temperature of the binodal curve of the phase diagram [74]. Nevertheless, T_T is an important parameter of a thermo-responsive polymer and is easily experimentally determined by measuring the turbidity of a polymer solution.

1.5.1.4 PNIPAM-Based Hydrogels

Among the extensively studied LCST polymers, poly-(N-isopropylacrylamide) (PNIPAM) is the most investigated and best characterized one because of its relative low LCST in water (~ 32 °C) [75]. Like a variety of other polymers, PNIPAM is generated from the NIPAM monomer by a free radical polymerization process that is depicted in **Figure 1.8**. It consists of hydrophilic and hydrophobic parts, which are responsible for its LCST behavior (**Figure 1.10**) [74]. In PNIPAM-based crosslinked hydrogels up to 90 wt% water can be stored below the LCST, whereas at high temperatures most of the water is expelled causing a great change in gel volume [76]. Additionally, the T_T and other features of PNIPAM can be easily tuned by co-polymerization with various different other monomers [77]. A highly swollen state in combination with an easily tunable LCST close to the physiological temperature predestinates PNIPAM as candidate for applications as sensor [78], in drug delivery [79], as artificial actuators or muscles [80, 81, 82] or as selective filter [83].

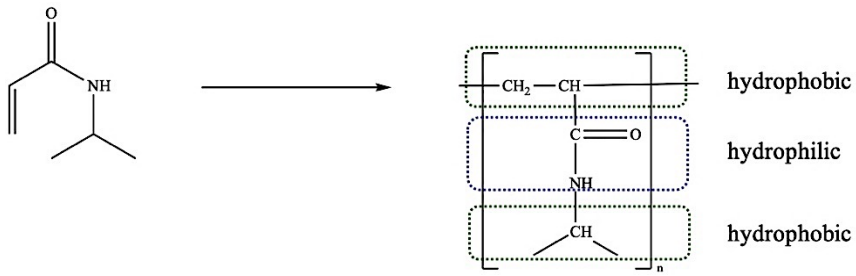

Figure 1.10 *Structure and Hydrophilic/Hydrophobic Classification of PNIPAM*
PNIPAM as amphiphilic polymer exhibits distinct hydrophilic and hydrophobic regions. The backbone of the polymer is hydrophobic while the side chains consist of hydrophilic amide groups and hydrophobic isopropyl groups, respectively. Below the LCST, hydrogen bonds between water molecules and the amide groups of the side chains are formed leading to a highly swollen hydrogel. Above the LCST, an entropy-driven change from a coil to a globular state with expulsion of the majority of the hydrogel-bound water occurs which is leading to a massive decrease in the hydrogel volume.

1.5.2 Multi-Stimuli-Responsive Hybrid Gels: PNIPAM/Gold Nanorods Composite Gels

By incorporating other functional monomers [84, 85, 86, 87], metallic [88, 89] or magnetic nanoparticles [90, 91] or other materials, e.g. silica particles [92, 93], hybrid gels responding to several stimuli can be generated.

The inclusion of gold nanorods into the thermo-responsive PNIPAM hydrogel structure allows, for example, the triggering of the volume transition of the polymer

network either by direct heating or by light-induced heating. The basis for heating with light as a stimulus is the fact that gold nanoparticles can heat up strongly due to plasmon resonance. Plasmons are defined as collective oscillations of the free electrons in metals, which means, according to the Fermi liquid model in analogy to plasma, plasmons can be described as electron clouds that are coherently displaced from their equilibrium position around the lattice composed of positively charged metal cores (**Figure 1.11**) [94]. Although light-induced excitation of plasmons in the bulk matter below the metal skin depth is not allowed due to never crossing plasmon and photon energy dispersion curves, nanoparticles are an exception due to their size, so that localized surface plasmons can form [95].

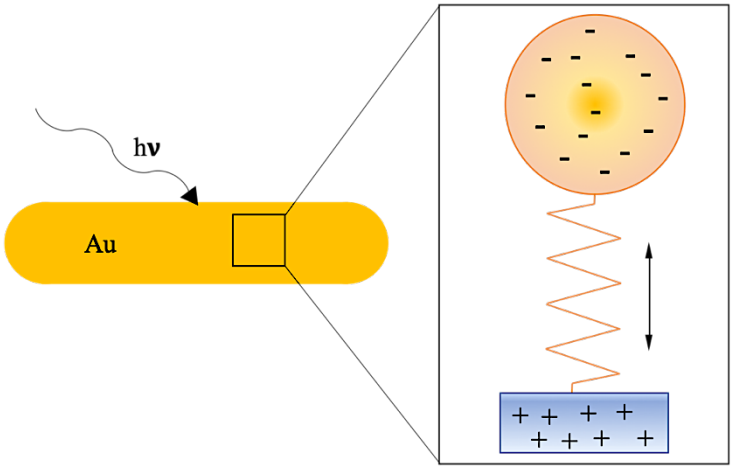

FIGURE 1.11 *GRAPHICAL ILLUSTRATION OF PLASMONS IN GOLD NANORODS*
Localized surface plasmons in gold nanorods can be approximated as a spring-mass harmonic oscillator, where the free electron density is the counterpart to mass in the classical description of the harmonic oscillator [94].

The surface plasmon resonance can be tuned by a reduction of the symmetry of the used nanoparticles. For example, using rod-shaped particles will lead to the presence of a second plasmon band in the absorption spectrum compared to one band visible in the spectrum of spherical particles [96]. Since the second absorption maximum of the rods can be shifted to the IR region of the light spectrum, the combination with biological systems is possible due to less radiation damage of cells. Applications based on plasmon resonance are numerous ranging from sensing [97], catalysis [98] or energy conversion [99] to optical recording [100] and from biomedical applications [101, 102, 103, 104] to Raman spectroscopy [105].

PNIPAM/golds nanorods composite hydrogels were used in the presented work to induce cell-like motility in artificial cells. The production of those cells was accomplished using microfluidics. In the following, the concepts of microfluidics are described in more detail.

1.6 Microfluidics

1.6.1 General Introduction

Microfluidic technology allows for the manipulation and precise control of fluids in an atto- to nano-liter scale within micrometer-scale channels (0.1 – 100 µm) [106]. It enables the miniaturization of fluidic platforms to centimeter sized chips, thus granting for the reduction of sample amount and a more efficient automated analysis [106].

The first microfluidic applications were developed in the field of chemical analysis in the form of a microscale gas chromatography system in 1979 [107]. With increasingly accurate photolithography, improved etching methods, the establishment of polydimethylsiloxane (PDMS) as the most widely used material for microfluidic device production [108] and developments in the field of photoresists for lithography [109], microfluidics became a highly diverse area of research. Today, the most common sector of microfluidics are lab- or organ-on-a-chip devices [110, 111].

The key features of microfluidics are implemented in various different areas, which range from biological and chemical synthesis and analysis [112, 113] to medical applications like diagnostics [114], drug delivery [115] and artificial organs [116]. Therefore, it is not surprising that microfluidic technology does not only find applications in science, but is also of interest for the industry [117].

1.6.2 Physical Background

The miniaturization of a macroscopic system to a microscopic one, which is done in microfluidics, is not only downscaling the dimensions of the system but also changes the importance of the prevailing forces. While macroscopic fluid systems are predominantly

affected by gravity and inertial forces, microfluidic systems are dominated by the surface tension/interfacial tension and viscous forces [118]. This change in influencing forces is due to an increase in the surface-to-volume ratio in the microfluidic system and therefore a stronger dependence on surface-associated forces [117].

In the following chapters, the concepts of viscous forces and surface/interfacial tension are introduced in more detail.

1.6.2.1 Viscous Forces

In microfluidic devices, different competing phenomena occur that need to be correlated to each other. This can be done by introducing dimensionless numbers which relating those competing phenomena. In microfluidic systems, viscous forces dominated in comparison to inertial forces [119]. The dimensionless number relating those two parameters is the Reynolds number Re which is given below [120]:

$$\mathrm{Re} = \frac{\rho \nu L}{\eta} \qquad \text{(eq. 1.2)}$$

ρ: Density of the fluid; ν: Velocity; L: Linear scale of the system;

η: Dynamic viscosity

Based on this equation it can be seen, that the minimization of a system is automatically causing a decrease of the Reynolds number. If Re is less than 2000, the flow properties of the system change from turbulent to laminar flow [121]. In this laminar flow regime, the fluids following a smooth layered path with adjacent layers sliding past each other with little to no mixing [120]. Besides, neither cross-currents perpendicular to the direction of flow or swirls of the fluid occur [189]. Additionally, the different layers are not moving with the same velocity, but with the layer at the center moving with approximately the double of the flow speed and the layers in contacts with walls are being almost stationary due to the non-slippery condition [190].

In the laminar flow regime, diffusion is the dominating transport process with the Péclet number as relating dimensionless number [122].

Similar to the Reynolds number, the Péclet number has a linear dependence on the scale of the system and an inverted dependence on the diffusion:

$$Pe = \frac{vL}{D} \qquad \text{(eq. 1.3)}$$

v: Velocity; L: Linear scale of the system; D: Diffusion coefficient

1.6.2.2 Surface Tension/Interfacial Tensions

Surface tension describes the tendency of fluids to minimize the surface free energy by modifying the fluid/air interface. This phenomenon results from the difference in energy between the molecules at the interface compared to their counterparts in bulk. Interfacial tension describes the same phenomenon but for interfaces of two immiscible liquids like water and oil [123]. The concept of surface or interfacial tension is of extreme importance when it comes to microfluidics, since it is one dominating force in the miniaturized system, which, for example, provides information on the stability of generated emulsions [124].

Since the surface or interfacial tension tends to curve the fluidic interface in order to balance the pressure difference along the fluid interface, it is linear dependent on those pressure differences and can be described using the Young-Laplace equation [117]:

$$\Delta p = \gamma\left(\frac{1}{R_1} + \frac{1}{R_2}\right) \qquad \text{(eq. 1.4)}$$

Δp: Pressure difference; γ: Surface or interfacial tension;

R_1, R_2: Radii of the curvature of the fluidic interface

An illustration of the equation is shown in **Figure 1.12**.

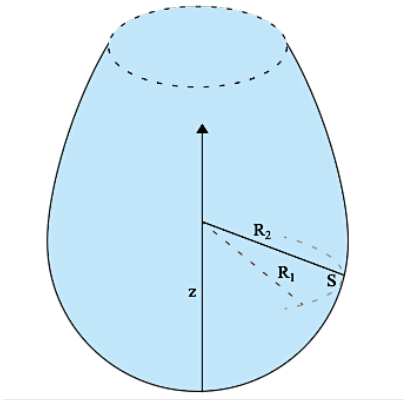

Figure 1.12 *Graphical Illustration of the Young-Laplace Equation in a Pendant Drop Set-up*
R_1 and R_2 are the principal radii of curvature on any point S on the fluidic surface. Adapted and modified from [125].

Surface or interfacial tension can be measured using pendant drop tensiometry based on the shape of a hanging drop. The drop is generated with a needle and either directly suspended in a bulk liquid or in air [123]. The shape of the so generated droplet is both dependent on the surface/interfacial tension, which seeks to minimize the surface area by creating a spherical shape as well as the gravity, which elongates the droplet into its typical pear-shaped form [126]. The Young-Laplace equation can only be solved analytically for the trivial droplet profile of a sphere, which is not applicable in pendant drop measurements. In those cases, the equation needs to be solved numerically, by correlating the surface/interfacial tension to the dimensionless Bond number Bo [123]:

$$Bo = \frac{\Delta\rho g R_0^2}{\gamma} \qquad \text{(eq. 1.5)}$$

$\Delta\rho$: Density Difference between the phases; g: Gravity constant;
R_0: Radius of the droplet at the apex; γ: Interfacial tension

1.6.3 Droplet-Based Microfluidics

Depending on the liquid manipulation methodology, microfluidics can be classified into two groups: continuous microfluidics, which deals with the manipulation of miscible liquids in a microfluidic chip or droplet-based microfluidics, which benefits from immiscible liquids like water and oil by formation of stable emulsions [127].

An emulsion refers to a colloidal mixture of substances that are immiscible in each other [128]. This allows for the production of individual reaction containers with a small volume of several femto- to nanoliters in a high throughput manner without any undesired contamination or evaporation. In order to obtain emulsions, different methods can be used varying from shaking methods [180] to the production in microfluidic chips. By using microfluidic devices, the droplet is produced by cutting the aqueous phase with a stream of oil using flow-focusing junctions. The size of the droplets is thereby mainly determined by the channel dimensions but can also be manipulated by applying different flow rates [130]. Regardless of the chosen production method, emulsions alone are not stable and will undergo phase separation over time. To avoid this, stabilizing surfactants are added to the emulsion [128, 168].

1.6.4 Surfactants

The term surfactant refers to a surface-active, amphiphilic molecule typically containing a hydrophilic head and a hydrophobic tail that can be used for the stabilization of emulsion droplets (**Figure 1.13**) [129].

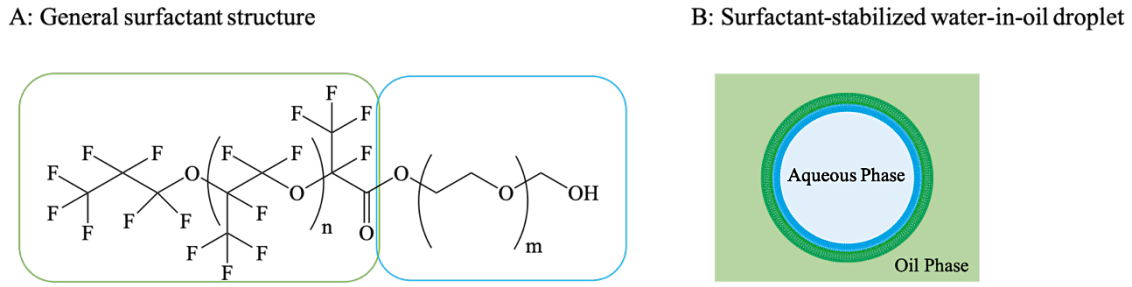

Figure 1.13 *Surfactant Structure and Stabilization of Water-in-Oil Emulsion Droplets using the Example of a PEG-Based Surfactant*
(A) Chemical structure of a PEG-based surfactant. The hydrophilic head group consisting of PEG is represented by a blue box, while the hydrophobic perfluorinated tail is boxed in green. (B) Schematically representation of surfactant-stabilized water-in-oil droplets. The hydrophilic head group comprised of PEG is depicted in blue, the fluorophilic tail is shown in dark green. The fluorinated oil is represented by a light green color and the aqueous phase pictured in light blue.

The composition of a surfactant can be adjusted according to the desired application. The hydrophobic tail, for example, can consist of hydrocarbon- or fluorinated carbon chains, depending on the used carrier oil. As hydrophilic head group, many polar or unpolar molecules can be used [131]. By using head groups that can either be functionalized or are already containing a functional unit, further functionality can be

provided. During droplet formation, surfactants self-assemble at the droplet interface in a dense monolayer, thus lowering the interfacial tension and providing the above-mentioned stabilization of the emulsion [132]. The ability of the surfactant to effectively shield the emulsion droplets from demixing is described by the hydrophilic-lipophilic balance (HLB). This balance is mainly influenced by the chemical composition, the length and the structure of the hydrophobic part of the surfactant [187] (**eq. 1.6**).

$$HLB = 20 * \frac{H_w}{H_w + L_w} \qquad \text{(eq. 1.6)}$$

H_w: Hydrophilic part of the surfactant; L_w: Lipophilic part of the surfactant

The HLB value allows for a rough estimation of the performance of a surfactant and is stated between 0 and 20, where 0 represents a completely lipophilic molecule and 20 a completely hydrophilic surfactant. In order to obtain stable water-in-oil droplets, a surfactant needs to be designed in such a way that a HLB value between 1 and 10 is reached [188].

The absorption process of surfactant molecules from the bulk to the interface can be described using the Gibbs adsorption isotherm (**eq. 1.7**) [133], which directly links the surfactant coverage of the fluid/fluid interface with the interfacial tension allowing for the physical understanding of the stabilizing properties of surfactants.

$$d\gamma = -\sum_i \Gamma_i d\mu_i \qquad \text{(eq. 1.7)}$$

γ: Interfacial tension; μ: Chemical potential; Γ: Surface coverage

The surface coverage is dependent on the chemical and physical properties of the used surfactant, for example the charge or bulkiness. A charged surfactant is hereby for instance lowering the surface coverage due to electrostatic repulsion [134].

However, the Gibbs adsorption equation is only valid for surfactants below a critical concentration, the so-called critical micellar concentration (CMC) [133]. Below this concentration, surfactant molecules are dissolved individually and have a strong impact on the interfacial tension, while above the CMC the surfactant molecules are forming micelles in order to minimize the contact between solvent molecules and the hydrophilic or

hydrophobic part of the surfactant [135]. Despite, the micelles are not influencing the surface tension, which is why a further increase of the surfactant concentration does not have a significant effect on the system. Typical CMC values for water-soluble surfactants are stated between several micromolar (µM) up to hundreds of millimolar (mM) [136] and are influenced by the surfactant properties, like constitution (diblock, triblock surfactant) and structure.

In the context of this work, a droplet-based microfluidic approach was used for the generation of water-in-oil emulsion droplets as a synthetic cell model. Besides the droplet formation, the influence of different surfactants on the droplet behavior was investigated.

2 Motivation

Cell motility is fundamental for establishing and maintaining the proper organization of multicellular organisms and is essential for immune response, wound repair, and tissue homeostasis [151, 152]. Besides the involvement in fundamental physiological processes, motility-mediated mechanism are also playing a crucial role in a variety of disease states. Therefore, the analysis and the deep understanding of those migration processes are of great importance. However, cellular motility involves the complex functional coordination of various proteins, including the cytoskeleton component actin, different signaling molecules and the integrin-based adhesion complexes [153].

In order to study such complex processes, the development of bio-inspired "synthetic cell" model systems, which could serve as platforms for assembling specific sets of minimal components and testing their functional role in initiating cellular-like motility is a key goal. The construction of these artificial cells can be realized in two different ways, either by reducing the complexity of a natural cell or by building a cell from scratch using synthetic materials. Currently, the bottom-up assembly of artificial cells in general and cellular motility in particular is based on nature-derived compounds. While this leads to a certain reduction in complexity, the implementation of synthetic materials can further help to reduce the complexity due to less specialized conditions in terms of sophisticated solvent/buffer requirements. Therefore, the central goal of my interdisciplinary research was the bottom-up reconstitution of cellular motility by means of synthetic materials.

In this thesis, a synthetic cell model system was generated using droplet-based microfluidics. This technology was designed to provide a platform for the high-throughput synthesis of artificial cells. Water-in-oil emulsion droplets as cellular compartments containing a PNIPAM-based network as artificial cytoskeleton were designed and tested to reconstitute basic principles of cellular motility. With this, a flexible minimal system for the implementation of artificial cell dislocation can be provided.

Moreover, the PNIPAM-based system was combined with natural cytoskeleton components to generate a hybrid cytoskeleton complex as proof of principle concept. Besides the demonstration of biocompatibility, the successful combination with a highly specialized natural system might serve as an advanced platform towards synthetic cell systems for fundamental research and potential biomedical applications.

Materials and Methods

3 Materials

In this section, the substances and solutions used for the preparation of surfactants, gold nanorods, bulk hydrogels, droplets and microgels are presented. Unless otherwise stated, all chemicals and solvents were purchased from commercial suppliers (Sigma Aldrich, Carl Roth, Merck, Acros) and used without further purification.

3.1 Chemicals

3.1.1 Surfactant Synthesis

Table 3.1 *Chemicals used for the Synthesis of the PNIPAM-Based Surfactant*

Krytox™ 157 FSH	#157 FSH	Miller Stephenson
Oxalyl chloride	#221015	Sigma Aldrich
Triethylamine	#X875.1	Carl Roth
N,N-dimethylformamide, extra dry (98%)	#326871000	Acros organics

3.1.2 Gold Nanorod Preparation

Table 3.2 *Used Compounds for the Synthesis of Gold Nanorods*

Hexadecyltrimethylammonium bromide (CTAB, 99%)	#52365	Sigma Aldrich
Gold(III) chloride hydrate (99.995%)	#254169	Sigma Aldrich
Silver nitrate (99.999%)	#204390	Sigma Aldrich
Sodium borhydride (>96%)	#71320	Sigma Aldrich
Ascorbic Acid (reagent grade)	#A7506	Sigma Aldrich
5-bromosalicylic acid (90%)	#461814	Sigma Aldrich

3.1.3 PNIPAM Gel Preparation

Table 3.3 *Production of Thermo-Responsive PNIPAM Gels*

N-isopropylacrylamide (NIPAM, 99%)	#731129	Sigma Aldrich
N,N'-methylenebis(acrylamide) (BIS, 99%)	#146072	Sigma Aldrich
2-hydroxy-2-methylpropiophenon (D1173, 97%)	#405655	Sigma Aldrich

3.1.4 PNIPAM Derivates

Table 3.4 *Different PNIPAM Derivates*

Poly(N-isopropylacrylamide), carboxylic acid terminated (M_n=2000 g/mol)	#724815	Sigma Aldrich
Poly(N-isopropylacrylamide), amine terminated (M_n=2500 g/mol)	#724823	Sigma Aldrich

3.2 Solvents

Although LC-MS grade water was used for the majority of experiments, Type 1 water was used for the performance of pendant drop tensiometry measurements. Type 1 water is hereby defined as ultrapure water with distinct properties like a precise resistance (18.2 MΩcm) [154]. A widely used definition of ultrapure water is provided by the American Society for Testing and Materials (ASTM).

TABLE 3.5 *SOLVENTS*

LC-MS grade H_2O	#115333	Merck
Type 1 water (Elga LabWater)		Veolia Water Technologies Deutschland GmbH
Novec 7100 (HFE7100)	#FL-0001-HP-5000	Iolitec
Novec 7500 (HFE7500)	#FL-0004-HP-1000	Iolitec
Fluorinert® FC-40	#FL-0005-HP-1000	Iolitec
Dichloromethane, extra dry (99.9%)	#10487532	Acros Organics
Silicon Oil, viscosity 50 cSt (25 °C)	#378356	Sigma Aldrich

3.3 SURFACTANTS

Besides the self-made PNIPAM surfactant, a commercially available fluorosurfactant from RAN biotechnologies (Beverly, USA) and the DOWSIL™ RSN-0749 resin (Dow Corning Inc., Midland, USA) were used. Concerning the commercial fluorosurfactant, not much information is provided by the company. Therefore, the surfactant was characterized regarding its physical properties (interfacial tension (IFT) values at different temperatures and Krytox level, see **Sections 5.1.2.2.3** and **5.1.2.2.4**). The used DOWSIL™ RSN-0749 resin is a blend of approximately 50 wt% cyclopentasiloxane and 50 wt% trimethylsiloxysilicate. Since this surfactant was just used for the formation of PNIPAM/gold nanorod microgels and was removed after NIPAM polymerization, no characterization was performed.

TABLE 3.6 *COMMERCIALLY AVAILABLE SURFACTANTS*

Commercial Fluorosurfactant	#008-FluoroSurfactant	RAN Biotechnologies
DOWSIL™ RSN-0749 Resin	#4119565	Dow Corning Inc.

3.4 Lipids

Table 3.7 *Lipids for the Coating of Microgels*

1,2-dioleoyl-sn-glycero-3-phosphoethanolamine-N-(lissamine rhodamine B sulfonyl) (ammonium salt) (LissRhodPE)	#810150C	Avanti Polar Lipids
1-palmitoyl-2-oleoyl-sn-glycero-3-phospho-(1'-rac-glycerol) (sodium salt) (POPG)	#840457	Avanti Polar Lipids
1-palmitoyl-2-oleoyl-glycero-3-phosphocholine (POPC)	#850457	Avanti Polar Lipids

3.5 PDMS Devices

Table 3.8 *Preparation of PDMS-Based Microfluidic Chips*

Polydimethylsiloxane Sylgard 184	#1673921	Dow Corning
Extran® MA 01	#107555	Merck Milipore
Ombrello®	# 4260467810529	Moton Automotive
PTFE tubing ($Ø_{ID}$ 0.3 mm, $Ø_{OD}$ 0.6 mm)	#Z609692	Bola

3.6 Observation Chambers

Custom-made observation chambers were used for the analysis of different samples using microscopy. For the assembly, coverslips were mounted on top of microscopy slides using double sided sticky tape (for specifications, see **Table 3.9**). In case of friction experiments, fluorophilic-coated coverslips (RAN Biotechnologies) were used. The fluorophilic surfaces are based on cover glasses from the company The Lab Depot (Cover glasses No. 1, 18 mm x 18 mm, #1401-10).

Table 3.9 *Materials used for the Assembly of Observation Chambers*

Microscopy slide 24 mm x 60 mm, No. 1	#H878.2	Carl Roth
Cover slip 18 mm x 18 mm, No. 1	#0657.2	Carl Roth
Fluorophilic Coverslips 18 mm x 18 mm, No. 1		RAN Biotechnologies
Double sided sticky tape	#05338	Tesa®
Picodent twinsil®	#1300 5000	picodent Dental Produktions- und Vertriebs GmbH

3.7 NIPAM Polymerization Solutions

NIPAM polymerization solutions were prepared using a NIPAM stock solution containing 4 M NIPAM and either 1, 2 or 5 mol% BIS as crosslinking reagent. The noted volumes should be kept as a guide for ratios between the different chemicals.

Table 3.10 *Polymerization Solution: 0.125 M*

Solutions	Volume [µL]	Concentration
Gold nanorod solution	300	9.50×10^5 particles/ml
NIPAM (containing BIS)	12.5	0.125 M
LC-MS grade water	87.5	
Photoinitiator D1173	2.4	0.6 wt%

Table 3.11 *Polymerization Solution: 0.25 M*

Solutions	Volume [µL]	Concentration
Gold nanorod solution	300	9.50×10^5 particles/ml
NIPAM (containing BIS)	25	0.25 M
LC-MS grade water	75	
Photoinitiator D1173	2.4	0.6 wt%

Table 3.12 Polymerization Solution: 0.5 M

Solutions	Volume [µL]	Concentration
Gold nanorod solution	300	9.50×10^5 particles/ml
NIPAM (containing BIS)	50	0.5 M
LC-MS grade water	50	
Photoinitiator D1173	2.4	0.6 wt%

Table 3.13 Polymerization Solution: 1 M

Solutions	Volume [µL]	Concentration
Gold nanorod solution	300	9.50×10^5 particles/ml
NIPAM (containing BIS)	100	1 M
LC-MS grade water	0	
Photoinitiator D1173	2.4	0.6 wt%

3.7 Actin Filaments

Table 3.14 Labeling of Actin Filaments

Actin acetone powder (New Zeeland white rabbit skeletal muscle)	Preparation:	Cornelia Weber
Rhodamine-phalloidin	#00027	Biotium
MgATP (>95%)	#A9137	Sigma Aldrich

3.8 Buffers

Table 3.15 *Double-density AB Buffer*

Solutions	Company	Concentration [mM]	pH
HEPES	Carl Roth	50	7.4
KCl	Sigma Aldrich	50	
$MgCl_2$	Sigma Aldrich	8	
EGTA	Sigma Aldrich	1020	

Table 3.16 GAB Buffer

Solutions	Company	Concentration [mM]	pH
TRIS-HCl	Sigma Aldrich	2	8.0
$CaCl_2$	Sigma Aldrich	0.2	
ATP disodium salt	Sigma Aldrich	0.2	
NaN_3	Sigma Aldrich	0.005%	
DTT	Sigma Aldrich	0.2	

Table 3.17 Polymerization Buffer

Solutions	Company	Concentration [mM]	pH
Tris-HCl	Sigma Aldrich	20	8.0
KCl	Sigma Aldrich	500	
$MgCl_2$	Sigma Aldrich	20	
ATP disodium salt	Sigma Aldrich	10	

4 Methods

In this chapter, methods for the production and characterization of the systems are presented.

4.1 PNIPAM Surfactant

4.1.1 Synthesis

The synthesis of PFPE-PNIPAM diblock surfactant (PNS) followed the procedure reported earlier [155] with several modifications. The synthesis was carried out under nitrogen atmosphere in flame-dried glass ware in two steps. First, PFPE-carboxylic acid (MW= 7000 g/mol) was converted to the acid chloride using oxalyl chloride. In a second step, the acid chloride was coupled to amine-terminated PNIPAM (MW=2500 g/mol).

In a Schlenk flask, 5 ml HFE7100 was cooled to 0 °C with an ice bath and afterwards, oxalyl chloride (0.3 ml, 2.5 mmol, 5.0 eq) was added while stirring. In a second Schlenk flask, PFPE-carboxylic acid (Krytox, 4.56 g, 0.5 mmol, 1.0 eq) was dried under reduced pressure for 30 min to ensure water-free conditions and afterwards dissolved in 5 ml dry HFE7100 containing 1 drop of N,N-dimethylformamide (DMF). The PFPE solution was then added dropwise to the oxalyl chloride solution over a period of 30 min while stirring. Afterwards, the solution was slowly heated to room temperature and stirred for additional 12 h. To remove the excess of oxalyl chloride and to dry the PFPE-acid chloride, the reaction mixture was transferred to a rotary evaporator (40 °C) with taking care that the acid chloride was not in contact with air. After complete removal of the solvent and oxalyl chloride, the residue was again dissolved in 8 ml HFE7100. In another Schlenk flask, amine-terminated PNIPAM (1.43 g, 0.55 mmol, 1.1 eq) was dried under reduced pressure for 30 min and afterwards dissolved in 10 ml dry DCM. Triethylamine (0.1 ml, 0.7 mmol, 1.4 eq) was added to the PNIPAM solution and the mixture was stirred for 30 min to activate the PNIPAM. Afterwards, the PFPE-acid chloride solution was added all at once and the reaction mixture was stirred for 20 h.

After the reaction was finished, the solvent was removed at 40 °C with a rotary evaporator and the crude product was partially dissolved in HFE7100. To remove insoluble parts, the HFE solution was filtered first using a paper filter (1/2 folded, grade 595, Ø 125 mm; Schleicher&Schuell, Germany) and afterwards a syringe filter (0.22 µm, Ø 33 mm; TPP, Switzerland). The solvent was removed using a rotary evaporator (40 °C) and the desired product completely dried at the vacuum line with 87% yield (4.12 g, 0.43 mmol).

4.1.2 Surfactant Characterization

4.1.2.1 FTIR and MALDI-TOF MS Measurements

Fourier-transformed infrared spectroscopy (FTIR) and matrix-assisted laser desorption ionization – time of flight mass spectrometry (MALDI-TOF MS) measurements were performed to assess the purity of the self-made PNIPAM surfactant.

FTIR measurements were performed on a Nicolet Nexus 870 Fourier transform infrared spectrometer (Thermo Electron GmbH, Germany) equipped with a DTGS detector. The pure surfactant was measured in a demountable path-length cell for liquid FTIR (Thermo Scientific, USA) using KBr disks. An average of 100 scans per analysis was collected with a resolution of 2 cm^{-1}.

MS measurements were performed by M.Sc. Martin Schröter (PhD student in the department of Cellular Biophysics, MPI for Medical Research), on a MALDI-TOF MS system (AXIMA Performance, Shimadzu, Japan). In case of PNS, spotting was done on a stainless steel plate by overlaying two times 0.5 µl of a mixture containing dihydroxybenzoic acid (DHB; 50 mg/ml in tetrahydrofuran (THF)) and anthralin (50 mg/ml in THF) in a volume ratio of 1:1 (matrix mix), followed by two times 0.5 µl of a mixture containing DHB (50 mg/ml in THF), anthralin (50 mg/ml in THF) and PNS (5 mg/ml in 1,1,1,3,3,3-hexafluoro-2-propanol (HFIP)) in a volume ratio of 1:1:2 (sample mix). The spot was afterwards lined two times using 0.5 µl matrix mix. In case of amine-terminated PNIPAM, spotting was performed in the same way. However, instead of using matrix mix, 0.5 µl DHB (50 mg/ml in THF) was used and the sample mix contained DHB (50 mg/ml in THF) and amine-terminated PNIPAM (5 mg/ml in THF) in a volume ratio of 1:1.

4.1.2.2 NMR Measurements

For NMR measurements, the surfactant was dissolved in a mixture of 3:0.7 of $CDCl_3$ and 2,2,2-Trifluoroethanol-d_3 due to low solubility of the surfactant in well-established solvents. ^1H and were recorded on a Bruker Ascend™ 400 (400 MHz for ^1H) at room temperature. Chemical shifts are given in ppm and coupling constants in Hz. ^1H spectra were calibrated in relation to residual solvent signals ($CDCl_3$: 7.26 ppm). The following abbreviations were used for ^1H NMR to indicate the signal multiplicity: s (singlet), d (doublet) and m (multiplet).

4.1.2.3 Partitioning Experiment

To examine the accumulation of PFPE carboxylic acid (Krytox) at the water-oil interface, partitioning experiments were performed [161]. For the experiments, the surfactants and Krytox were dissolved in HFE7500.

As calibration standard, 100 µl HFE7500 oil containing Krytox within a concentration range between 0 and 1 mM was added to reaction tubes (PCR tube, Braun GmbH, Germany). For evaluation of Krytox levels in the tested surfactants, 100 µl of a 1 mM surfactant solution was added into a reaction tube. For the commercial fluorosurfactant, a concentration of 1.4 wt% was used. LC-MS grade water containing rhodamine 6G (1 mM Rho6G) was gently added on top of the oil solutions. Due to a 1:1 interaction between Krytox and Rho6G, partitioning of Rho6G molecules in the oil phase was observed. Following 72 h incubation, samples from the oil and aqueous phase were carefully collected, diluted with a factor of 1:10 and transferred into a 96-well plate. The Rho6G content was determined in a plate reader (Tecan Spark, Switzerland) by measuring the absorbance at 530 nm.

4.1.2.4 Interfacial Tension Measurements

To determine the interfacial tension (IFT) of surfactant stabilizing emulsions, pendant drop tensiometry was performed.

For the measurements, all surfactants and Krytox were dissolved in Fluorinert® FC-40 and measured against Type 1 water or a solution of 100 µM PNIPAM-COOH (MW=2000 g/mol) in Type 1 water, which were poured into a plastic cuvette and renewed after every sample. Every surfactant solutions was transferred into a new 1 ml disposable

syringe (Injekt®-F Solo, B. Braun Melsungen, Germany) equipped with a metal canula (0.8 mm x 22 mm blunt/dull, B. Braun Melsungen, Germany). Density of oil phase and aqueous phase were set to 1.9 g ∗ cm^{-3} and 0.99 g ∗ cm^{-3}, respectively.

The measurements were performed using a DSA25 drop shape analyzer (Krüss GmbH, Germany) and droplets were created with an automated metering system. For each sample 10 individual droplets were measured. For measurements at 40 °C, an incubation chamber connected to a heat circulation pump (KISS 202C, Peter Huber Kältemaschinenbau AG, Germany) was used.

The size of the droplets was selected in such a way that 70 individual measurements were possible without loss of the droplets and with maximum volume at the same time. In case stable droplets for 70 single measurements could not be generated, the droplets were measured as long as possible before loss. Between every individual measurement, an interval of 5 s was chosen. The droplets were analyzed using the provided Advance software, which uses the Young Laplace equation to fit droplet shape. The IFT value after 70 single measurements was used for further analysis.

4.2 Gold Nanorods

4.2.1 Synthesis

Gold nanorods were prepared by a modified version of the seeded growth process according to literature [156]. If not stated otherwise, the reaction was carried out in LC-MS grade water in the absence of light and at room temperature.

In brief, for the preparation of the seed solution 5 µl 50 mM $HAuCl_4$ solution was added to 940 µl 0.1 M CTAB solution at 27-30 °C under mild stirring. The solution was slowly stirred without perturbation for 5 min. Afterwards, 60 µl of a freshly prepared 10 mM $NaBH_4$ solution was rapidly injected under vigorous stirring (> 1400 rpm, brown solution). The solution was extensively stirred (> 1400 rpm) for 30 s and afterwards mildly stirred (200 rpm) at 27-30 °C until further use. For the preparation of the growth solution, 45 mg 5-BrSA were dissolved in 50 ml 0.05 M CTAB solution at 65 °C. Once the 5-BrSA was dissolved completely, the solution was cooled to room temperature and afterwards,

480 µl of a freshly prepared 10 mM $AgNO_3$ solution was added under stirring. The solution was stirred for 15 min (400 rpm) and then 500 µl 50 mM $HAuCl_4$ was added (pre-reduction, orange solution). The progress of the pre-reduction was optically monitored at 396 nm with an UV Vis spectrometer (LAMBDA 25, PerkinElmer, USA). To achieve a longitudinal plasmon band centered around 800 nm, the OD at 396 nm needs to be centered between 0.8 and 0.85. Once the desired OD was reached, 150 µl of a fresh 100 mM AA solution was added under vigorous stirring (> 1400 rpm), The solution turned colorless after a few seconds. After stirring for 30 s, 80 µl seed solution was added, the solution stirred for 30 s and the solution afterwards kept undisturbed for 20 h in the absence of light to allow the growth of gold nanorods. The nanorods were then purified via centrifugation (Avanti J-E highspeed centrifuge, Beckmann Coulter, rotor JA 25.50, 14000 rpm, 22 °C, 15 min, two times) and stored at 4 °C in LC-MS grade water in the dark in a glass vial. The nanorods were characterized with UV Vis absorbance spectra and TEM micrographs.

4.2.2 Characterization of Gold Nanorods

4.2.2.1 Transmission Electron Microscopy (TEM)

TEM measurements were performed by Ulrike Mersdorf (Technical assistant, MPI for Medical Research).

Samples were prepared by applying 5 µl gold nanorods solution onto a glow-discharged 200 mesh C-flat holey carbon-coated multihole grid (Protochips, USA) and incubation for 2 min. The grids were afterwards washed five times using double distilled water and negative stained by incubating the grids for 1 min with 0.5 wt% uranyl acetate solution. The negative stained grids were air dried and imaged on a FEI Tecnai G2 T20 twin transmission electron microscope (FEI NanoPort Eindhoven, Netherlands) operated at 200 kV. Electron micrographs were recorded with a FEI Eagle 4k HS, 200 kV CCD camera with a total dose of ≈ 40 electrons/$Å^2$. Images were acquired at 50000 × nominal magnification with 1.24 µm defocus applied.

4.2.2.2 Absorption Spectra

Absorption spectra of gold nanorods were recorded on a LAMBDA 25 UV/Vis spectrometer (PerkinElmer, USA). The nanorods were measured between 300 and 1000 nm in 2 nm steps. For the measurement, 100 µl of the gold nanorod solution was transferred

into a plastic cuvette (Brand™ UV Cuvette, Brand GmbH, Germany). As blank, 100 µl LC-MS grade water was used.

4.2.3 Calculation of Gold Nanorod Concentration

The calculation of the amount of gold nanorods in the solution is based on the physical dimensions determined via TEM micrographs and the absorption values determined at 400 nm [156]. For the calculations, a cylindrical shape of the nanorods was chosen as model. Assuming a length of l = 35 nm and a width of w = 10 nm with an absorption value of A = 0.517140 (λ = 400 nm), the following formulas result in a gold nanorod concentration of $9.50 * 10^5$ particles/ml.

$$V_{Nanorod} = \pi l r^2 = 2.749 * 10^{-15} m^3 \quad \text{(eq. 4.1)}$$

$$m_{Au} = V_{Nanorod} * \rho_{Au} = 5.311 * 10^{-11} kg \quad \text{(eq. 4.2)}$$

$$n_{Au} = \frac{m_{Au}}{M_{Au}} = 2.696 * 10^{-13} mol \quad \text{(eq. 4.3)}$$

$$A = \varepsilon * c * d \rightarrow c = \frac{A}{\varepsilon * d} = 2.560 * 10^{-4} M \quad \text{(eq. 4.4)}$$

$$c_{Au} = n_{Au} * \frac{N_{Nanorods}}{V_{Solution}} \rightarrow N_{Nanorods} = \frac{c_{Au} * V_{Solution}}{n_{Au}} = 9.50 * 10^5 \quad \text{(eq. 4.5)}$$

$r = \frac{w}{2}$; $\rho_{Au} = 1.932 * 10^4 kg * m^{-3}$; $M_{Au} = 196.97\ g * mol^{-1}$; $\varepsilon = 2.02 * 10^3 M^{-1} * cm^{-1}$ [160]; $d = 1cm$

4.3 Microfluidic Device Production

The microfluidic devices used in this thesis were made of polydimethylsiloxane (PDMS, Sylgard 184, Dow Corning, USA) and produced via standard photo- and soft lithography methods. The procedure is summarized below.

4.3.1 Photolithography

The master wafers for the microfluidic devices were prepared by M.Sc. Christoph Frey (PhD student in the department of Cellular Biophysics, MPI for Medical Research). The procedure is described in more detail elsewhere [157]. Shortly, wafers were designed using the computer-aided design (CAD) software QCAD-pro (QCAD Pro 3.17, RibbonSoft GmbH, Switzerland). To manufacture the wafers, a 30 µm thick film consisting of negative photoresist (negative photoresist SU8-3025, MicroChem, USA) was first applied to a silicon wafer using spin-coating. The wafer was then soft-baked on a hot plate at 95 °C for 15 min and afterwards, the CAD design directly printed on the photoresist by using the Tabletop Micro Pattern Generator µPG 101 (Heidelberg Instruments, Germany). For the post-exposure bake, the wafer was heated to 65 °C for 1 min, followed by heating and incubation at 95 °C for 5 min. The non-exposed resist was removed with mr-DEV600 (MicroChemicals, Germany) and hard baking was carried out in an oven at 150 °C for 15 min.

4.3.2 Soft Lithography

For PDMS device preparation, the elastomer and the curing agent were mixed in a 10:1 ratio, poured onto the wafer and afterwards put in a desiccator for 2-3 h to remove air bubbles. The PDMS was cured at 65 °C for 3 h and the devices were cut, pealed-off the wafer, punched with a biopsy puncher (0.5 mm, World Precision Instruments, Germany) to allow connection of polytetrafluoroethylene (PTFE) tubing (0.4 x 0.9 mm, Bola, Germany) and cleaned in an ultrasonic bath afterwards. The cleaning procedure is listed in **Table 4.1**. The cleaned devices were coarse dried using a nitrogen flow, completely dried at 65 °C for 30 min and oxygen plasma-treated (0.4 mbar O_2, 200 W, 35 seconds; PVA TePla 100, PVA TePla, Germany;) to fix them onto cleaned, plasma-treated glass slides (24 mm x 60 mm, Roth). After fixation, the devices were incubated at 65 °C for 24 h to strengthen the PDMS glass bond. PDMS device channels were coated with Ombrello® (Moton Automotive, Germany) in order to render them hydrophobic. To insert electrodes into the microfluidic chip, the device was heated to 80 °C on a hot plate, and a low-melting-point alloy (51% indium, 32.5% bismuth, 16.5% tin, Indalloy, GPS Technologies,

Germany) was melted inside the microchannels designed for the electrodes. Electric wires were afterwards connected to the molten solder.

TABLE 4.1 *CLEANING PROCEDURE FOR MICROFLUIDIC DEVICES*

STEP	CLEANING REAGENT	TEMPERATURE [°C]	TIME [MIN]
1	30% Extran in Type 1 water	65	15
2	Type 1 water	65	15
3	Type 1 water	65	15

4.3.3 USED MICROFLUIDIC DEVICES

Following, the used microfluidic devices are depicted (**Figure 4.1**). The devices were either adapted from literature or self-designed.

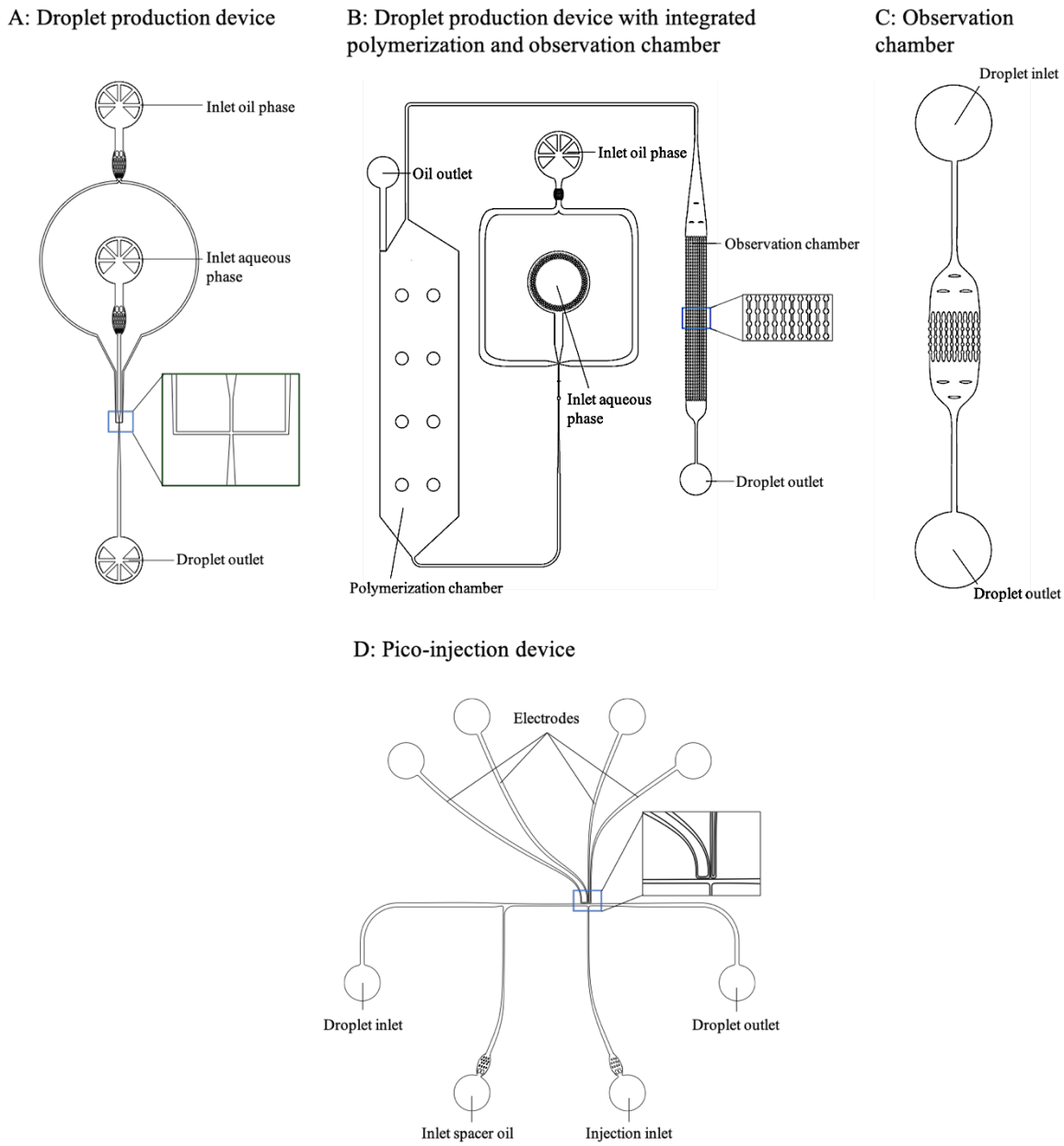

FIGURE 4.1 *SCHEMATIC ILLUSTRATION OF DIFFERENT DROPLET-BASED MICROFLUIDIC DEVICES*
(A) Droplet production device with one aqueous inlet. With a nozzle diameter of 20 µm, the devices are suitable for the production of droplets ranging from around 25 µm to 45 µm depending on the pressure settings. Insert is showing a magnification of the flow-focusing T-junction. (B) Droplet production device with integrated polymerization and observation chamber for on chip polymerization and observation of PNIPAM/gold nanorod gel droplets. The small round observation chambers (30 µm diameter) are connected by narrow channels with a width of 20 µm and a length of 50 µm. Every big observation chamber contains 500 small chambers. The insert is showing a magnification of the small channel-connected chambers. (C) Observation chamber for already polymerized composite gel droplets. The dimensions of the chamber/channel system is equal to the dimension of the chamber shown in (B). The number of chambers is reduced to 50. (D) Pico-injection device for sequential introduction of actin filaments into PNIPAM-containing droplets. The insert is showing the injection unit, which uses an alternating electric field for the poration and destabilization of the surfactant layer.

4.3.3.1 Droplet Production Device

A droplet-production device (**Figure 4.2** A) consisting of one oil and one water inlet was used to generate droplets. The inlets were connected via PTFE tubing (0.3 mm x 0.6 mm, Bohlender™ PTFE tubing, Bola, Germany) to a pressure system (OB1 MK3 pressure controller, Elveflow, France). Monodisperse water-in-oil droplets were produced with pressures ranging from 500 to 1000 mbar and 500 to 980 mbar for the oil phase and the aqueous phase, respectively. The oil channel was constructed in such a way that it encounters the aqueous phase from two opposite directions at the T-junction leading to constriction of the aqueous phase into droplets. The size of the produced droplets depends on the dimensions of the T-junction and the applied pressures. For the production of 30 µm droplets, a channel width at the T-junction of 20 µm and a pressure of 1000 mbar and 950 mbar for the oil and aqueous phase were used, respectively. The outlet of the device was connected to a microtube via PTFE tubing (same as used for the inlets).

4.3.3.2 Production Device with Integrated Polymerization and Observation Chamber

For induction of symmetry breaking and simultaneous observation of non-spherical droplets during temperature changes, a microfluidic device with an observation chamber consisting of 500 small chambers connected with narrow channels was used (**Figure 4.1** B). Besides the observation of droplets, also the production and polymerization of droplets is possible with this device. Note, depending on the used polymerization method, the production with a normal production device and afterwards polymerization outside the device should be preferred. For droplet transfer into the observation chamber, all inlets and outlets despite the oil inlet and the outlet connected to the observation chamber were sealed with picodent twinsil® and the pressure of the oil phase was set to 50 mbar. When enough droplets were entrapped in the observation chamber, all inlets and outlets were sealed with glue and the droplets were analyzed.

4.3.3.3 Observation Chamber Device

If only droplet examination was required, the observation chamber device was used. Therefore, droplets were first produced with a normal production device (**Figure 4.1** A), collected in a small tube, polymerized and afterwards transferred into the observation chamber (**Figure 4.1** C). For droplet transfer, a pressure of 50 mbar was used. If the desired

number of droplets was entrapped within the device, tubing was removed, the inlet and outlet were sealed with picodent twinsil® and the droplets were analyzed afterwards.

4.3.3.4 Pico-Injection Device

For further manipulation of PNIPAM/gold nanorods composite gel filled droplets, a pico-injection device, developed by Abate et al. [162] was used (**Figure 4.1** D). The device consists of an inlet channel for the introduction of pre-formed droplets for the injection. Furthermore, to prevent fusion of the droplets caused by the applied electric field, a separate oil channel is included functioning as separating stream. The injection unit is based on two electrode channels filled with Indalloy and opposite to the electrodes, a channel for the introduction of material into the passing droplets. An alternating electric field (AC, 1 kHz, 250 V) was applied to the electrodes to achieve the destabilization of the surfactant layer and subsequent fusion of the passing droplets with the injected material.

For pico-injection of actin filaments into PNIPAM composite gel filled droplets, a pressure system was used (OB1 MK3 pressure controller, Elveflow, France) and the pressures were set to 500 mbar (droplet channel), 450 mbar (oil spacer) and 230 mbar (actin injection channel). The electric field was generated using a HM 8150 signal generator (HAMEG, Germany) and amplified by 623B-H-CE amplifier (TREK, USA).

4.4 PNIPAM/Gold Nanorods Composite Gels

4.4.1 Gel Preparation

PNIPAM/gold nanorods composite hydrogels were prepared using different polymerization solutions ranging from 0.125 M NIPAM monomer up to 1.0 M in combination with either 1, 2 or 5 mol% BIS and gold nanorods. As photoinitiator, D1173 (0.6 wt%) was used.

For composite hydrogel formation, 100 µl of the respective polymerization solutions was transferred into a well of a 96-well plate and polymerized afterwards (Hamamatsu Lightningcure LC8, 365 nm, 15 cm working distance, 10 min). After

polymerization, 100 µl water was placed onto the hydrogels and the gels were swollen for 24 h.

For experiments containing different salts, a solution of the respective salt up to a final concentration of 30 mM was added to the polymerization solution.

4.4.2 Gel Characterization

4.4.2.1 Determination of Transition Temperature

The transition temperature of the PNIPAM/gold nanorods composite hydrogels was determined using absorption measurements (Tecan Spark, Tecan Group, Switzerland). Towards this end, the swollen hydrogels described above were heated between 27 °C and 37 °C in 1 °C steps. When the temperature was reached, the gels were incubated at the respective temperature for 5 min to allow the system to equilibrate before absorption measurements at 680 nm. After heating was completed, the samples were cooled and measured using the same procedure in reversed order.

If several heating/cooling cycles were measured, the above described plate reader operating protocol was executed several times in a row.

4.4.2.2 Determination of Sol Content

During hydrogel polymerization, a proportion of the used material is not integrated in the hydrogel structure. This so-called sol content can be determined via extraction. Therefore, 100 µl 1 M polymerization solution (see **Table 3.13**) either with or without gold nanorods were prepared in triplicates. Prior to polymerization in 2 ml tubes, the tubes were weighed for later subtraction of the weight. The hydrogels were composed of different crosslinker concentrations, namely 1, 2 and 5 mol% BIS respectively. The hydrogels were polymerized for 25 min (Hamamatsu Lightningcure LC8, 365 nm, 15 cm working distance). After polymerization, the samples were frozen at -80 °C for 2 h before drying for 20 h. Following freeze-drying, hydrogel-containing tubes were weighed again before the dried hydrogels were re-hydrated with 1.5 ml LC-MS H_2O for 20 h and freeze-dried as described above.

After freeze-drying, all samples were weighed again and the sol content was calculated based on following equation:

$$w_{Sol}[\%] = \left(1 - \frac{m_{dry-washed}}{m_{dry-untreated}}\right) * 100\% \quad \text{(eq. 4.7)}$$

4.5 PNIPAM/Gold Nanorods Gel Droplets

4.5.1 Droplet Production

4.5.1.1 One-Pot Assembly

Initially, an aqueous solution was prepared consisting of gold nanorods, NIPAM, BIS and D1173 dissolved in LC-MS grade water in different concentrations. The oil phase either contained commercial PFPE-PEG-based fluorosurfactant (CS) or self-synthesized PNIPAM surfactant (PNS).

For droplets formation, a volume of 50 µl aqueous phase was layered on top of 100 µl of the oil phase. Note that the reaction volume can be adjusted as long as an excess of surfactant solution is used. The sample was vigorously vortexed for 10 s until water-in-oil droplets spontaneously formed according to a protocol found in literature [180]. The droplets can be visualized as a milky emulsion layer on top of the oil phase.

In case of asymmetric droplets, stable (1.4 wt% CS) and unstable (0.7 wt% CS) droplets were prepared, the stable droplets layered on top of the unstable ones and both droplet populations carefully mixed prior to polymerization.

4.5.1.2 Droplet-Based Microfluidics

Droplet-based microfluidic devices were utilized for droplet production. For the purpose of this study, the pressures of the water and oil phase were set to 950 mbar and 1000 mbar, respectively.

The aqueous solution was prepared consisting of gold nanorods, NIPAM, BIS and D1173 dissolved in LC-MS grade water in different concentrations. The oil phase either

contained commercial 5 wt% PFPE-PEG-based fluorosurfactant (CS) or 2.5 mM self-synthesized PNIPAM surfactant (PNS).

4.5.1.3 Polymerization Protocol

Following droplets production, the droplets were collected in a 200 µl reaction tube (BRAND® PCR tubes, Brand GmbH, Heidelberg, Germany), afterwards polymerized for 2 h (Hamamatsu Lightningcure LC8, 365 nm, 15 cm working distance) and either directly used or transferred into another PDMS-based microfluidic device for experiments.

4.5.2 Droplet Analysis

4.5.2.1 Observation Chamber

To be able to document and analyze the behavior of prepared gel droplets, droplets were transferred into observations chambers (**Figure 4.2**) and analyzed using confocal microscopy. The observation chambers were prepared by assembling glass coverslips onto microscopy slides with double sided sticky tape. To prevent the evaporation of the sample, the coverslip was sealed with picodent twinsil®.

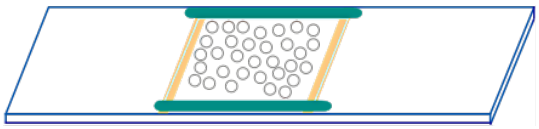

Figure 4.2 *Schematic Illustration of used Observation Chambers for Imaging*
The double-sided sticky tape is depicted in yellow, the glue is shown in green, glass slides are depicted in white with blue border and droplets are shown in grey.

4.5.2.2 Confocal Microscopy

Imaging of PNIPAM/gold nanorods composite hydrogel droplets was performed by means of the 561 nm laser line of an inverted confocal laser scanning microscope (LSM800, Zeiss, Germany), equipped with a Plan-Apochromat 20x/0.8 M27 air objective lens (Zeiss, Germany). Transmitted light images were obtained from the electronically switchable illumination and detection module (ESID). For induction of polymer transition, a stage-top incubator was used (PM 2000 RBT, Pecon, Germany).

4.5.2.3 Cryo Scanning Electron Microscopy (SEM)

For cryo-SEM sample preparation, 3 µl of droplet emulsion solution was dropped onto 0.8 mm diameter gold specimen carriers assembled on a freeze fracture holder (Leica Microsystems, Germany) and immediately immersed into liquid nitrogen. If the heated state of a sample was imaged, the holder and the droplet emulsion solution were directly heated before immersing into liquid nitrogen.

After freezing, the droplets were transferred using an evacuated liquid nitrogen-cooled shuttle (Leica EM VCT100, Leica Microsystems, Germany) into a Leica EM BAF060 freeze fracture and etching system (Leica Microsystems, Germany). For cryo observations, the droplets were fractured with a cooled knife in a 10^{-6}-10^{-7} mbar vacuum chamber at -160 °C. To allow for the sublimation of water, the droplets were heated to - 90 °C for at least 60 min and afterwards coated with 9 nm of carbon by electron beam evaporation.

For image acquisition, the samples were transferred via an evacuated liquid nitrogen cooled shuttle into the imaging chamber of a Zeiss Ultra 55 field emission electron microscope (FE-SEM) equipped with in-lens, secondary electron (SE) and angle selective backscattered electron (ASB) detector (Zeiss SMT, Germany). Top-view imaging was performed under low temperature conditions (top = -115 ± 5 °C) and with a working distance between 3 to 5 mm. Due to low conductivity of the emulsion droplets, low acceleration voltages of 1.5-2.0 kV were used. Signals were detected with the in-lens detector.

4.6 PNIPAM(Au)/Actin Hybrid Droplets

4.6.1 Preparation of Actin Filaments

Actin was purified by Cornelia Weber (Technical assistant, MPI for Medical Research).

In short, actin was extracted and purified from New Zeeland white rabbit skeletal muscle acetone powder based on protocol published by Pardee and Aspudich [163], modified by Kron et al. [164] and stored afterwards in GAB buffer.

Actin labelling and filament stabilization was performed with rhodamine-phalloidin by mixing 27.5 µl G-actin with 10 µl Actin polymerization buffer (10x) and 62.5 µl double density AB buffer. The actin monomers were polymerized for 30 min on ice. Afterwards, 20 µl rhodamine-phalloidin dissolved in methanol (MeOH) was dried and the actin solution was added subsequently. The labeling was performed for 1 h on ice. The labeled actin can be stored at 4 °C in the absence of light up to 1 month.

4.6.2 Droplet Production and Pico-injection of Actin

Prior to the production of hybrid droplets, PNIPAM/gold nanorods composite gel droplets were prepared using microfluidic chips. As oil phase, 5 wt% commercial fluorosurfactant (CS) in FC-40 was used and a solution containing gold nanorods (9.5×10^5 particles/ml), 0.5 M NIPAM, 5 mol% BIS and 0.6 wt% D1173 as aqueous phase. The pressures of the oil and aqueous phase were set to 1000 and 950 mbar, respectively. After production, the droplets were polymerized for 2 h (Hamamatsu Lightningcure LC8, 365 nm, 15 cm working distance).

For the pico-injection of actin filaments, an actin solution containing 20 µM rhodamine-phalloidin labeled actin and 5 mM MgATP was prepared directly before usage by diluting the actin stock (50 µM) with double density AB buffer. The pre-formed gel filled droplets, 5 wt% CS solution and the labeled actin filaments were introduced into a pico-injection device using PTFE tubing. The pressures for the different components were set to 500, 450 and 230 mbar for the droplets, the surfactant solution and the actin solution, respectively. For pico-injection, an alternating electric field (1 kHz, 250 V) was applied. The pico-injected droplets were incubated at 37 °C for 30 min and afterwards kept at 4 °C for 24 h to allow actin bundle formation inside the droplets.

4.6.3 Imaging of Hybrid Droplets

Imaging of PNIPAM/gold nanorods composite hydrogel droplets was performed by means of the 561 nm laser line of an inverted confocal laser scanning microscope (LSM800, Zeiss, Germany), equipped with a Plan-Apochromat 20x/0.8 M27 air objective lens (Zeiss, Germany). Transmitted light images were obtained from the electronically switchable illumination and detection module (ESID). For induction of polymer transition,

a stage-top incubator was used (PM 2000 RBT, Pecon, Germany) and the temperature was set to 40 °C to prevent denaturation of actin filaments.

4.7 PNIPAM/Gold Nanorod Microgels

4.7.1 Synthesis of Microgels

PNIPAM microgels were assembled from a solution containing gold nanorods (9.5 × 10^5 particles/ml), 1 M NIPAM, 5 mol% BIS and 0.6 wt% D1173 as aqueous phase and 5 wt% RSN-0749 in silicon oil. For the production, aqueous phase and oil phase were mixed in a ratio of 1:5 (100 µl aqueous phase + 500 µl surfactant solution) and afterwards either vortexed for 10 s or emulsified using an emulsificator (level 1 – 3, 30 s; T 10 basic ULTRA-TURRAX®, IKA Labortechnik, Germany). Hereinafter, the droplets were polymerized for 2 h (Hamamatsu Lightningcure LC8, 365 nm, 15 cm working distance), washed 5 times with isopropanol to remove the silicon oil and the surfactant and afterwards freeze-dried for 24 h. Afterwards, microgels were coated with lipids.

4.7.2 Lipid Coating of Microgels

For coating of microgels, a lipid solution containing 78.9% POPC, 20% POPG and 0.1% LissRhod PE (c = 3 mM) in chloroform was prepared and added afterwards to the freeze-dried microgels. The solution was gently mixed using a pipette and the chloroform was removed under reduced pressure. Lipid coated microgels were subsequent rehydrated for 24 h using LC-MS water.

4.8 Image Analysis

The analysis and processing of microscopy data was performed using Fiji [158]. To determine the change of droplet area during temperature-induced collapse of

PNIPAM/gold nanorods composite hydrogels, binary images were created from the raw data and the droplet area of at least 15 droplets per condition was analyzed.

4.9 Data Analysis

Plotting and fitting of obtained data was performed using OriginPro 2019 [159]. IR and UV Vis data was plotted with the line plot function, pendant drop and droplet area data with a scatter plot. To determine the transition temperature of hydrogels in bulk, the first derivative was calculated by fitting the data with a sigmoidal “dose response fit”. Calibration curves and other linearizable data was fitted using the linear fit function.

Results and Discussion

5 Results and Discussion

5.1 Water-in-Oil Emulsion Droplets

5.1.1 Implementation of a Cortical Artificial Cytoskeleton Structure

The aim of my thesis was to develop a minimal artificial cell model system in which the conversion of thermal energy into mechanical energy will lead to motility. Therefore, a smart composite material consisting of crosslinked PNIPAM and gold nanorods was realized within droplet-based synthetic cells (**Figure 5.1**). To implement the artificial cytoskeleton in synthetic cells, water-in-oil emulsion droplets were selected as artificial cell model because of their robustness. In addition, the combination of the artificial cytoskeleton with natural actin filaments to proof the biocompatibility of the implemented system and adaption to specialized conditions was conducted.

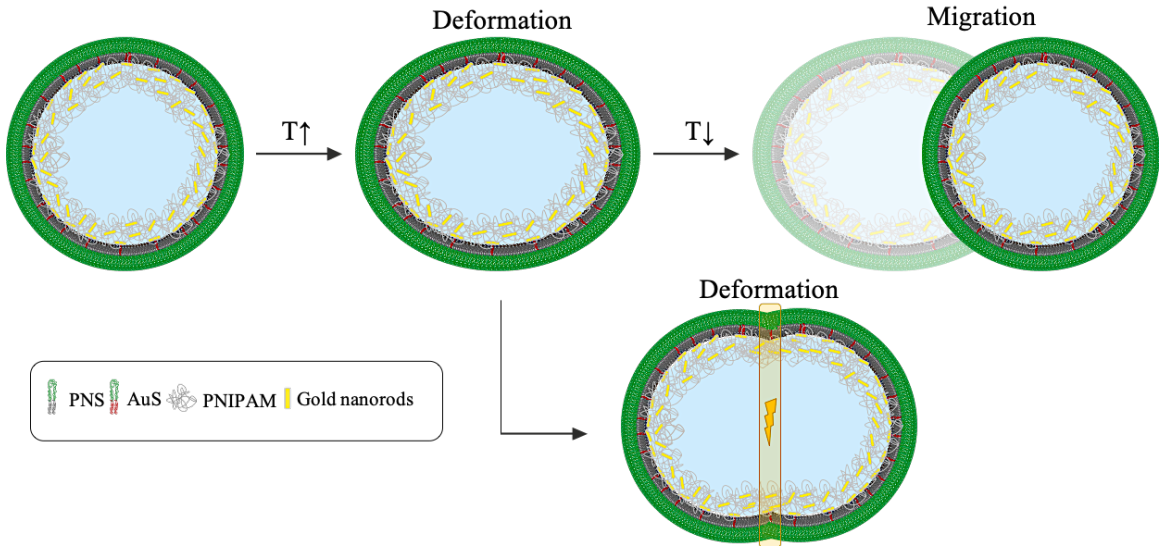

Figure 5.1 *Basic Idea of Artificial Cytoskeleton-Functionalized Synthetic Cells*
Schematic illustration of PNIPAM/Gold nanorod-functionalized water-in-oil emulsion droplets. PNIPAM is shown in grey, surfactants are pictured in green and either grey or red (PNS or AuS, respectively). Gold nanorods are represented in yellow. Temperature changes are indicated by "T" in combination with arrows, triggering of the polymer by light is shown by a yellow box containing a yellow flash. The different response modes of the encapsulated PNIPAM-based cytoskeleton material are shown.

Inspired by cortical actin filaments [165], in a first approach the formation of a thermo-responsive PNIPAM-based cortex was established (**Figure 5.1**) that will be able to deform the assembled water-in-oil droplets. To generate this cortex-like structure, a PNIPAM-based surfactant (PNS) and a thiolated surfactant to covalently immobilize gold nanorods were synthesized (**Figure 5.2**). It was aimed to directly polymerize PNIPAM to the droplets periphery. As anchoring point for the cortex formation, gold nanorods functionalized with a thiolated crosslinker were intended. The enrichment of NIPAM at the droplet periphery prior to polymerization was aimed to establish by PNIPAM/NIPAM interactions guided by PNS. Following, the synthesis and analysis of the thiolated and the gold-linked surfactant are discussed in more detail.

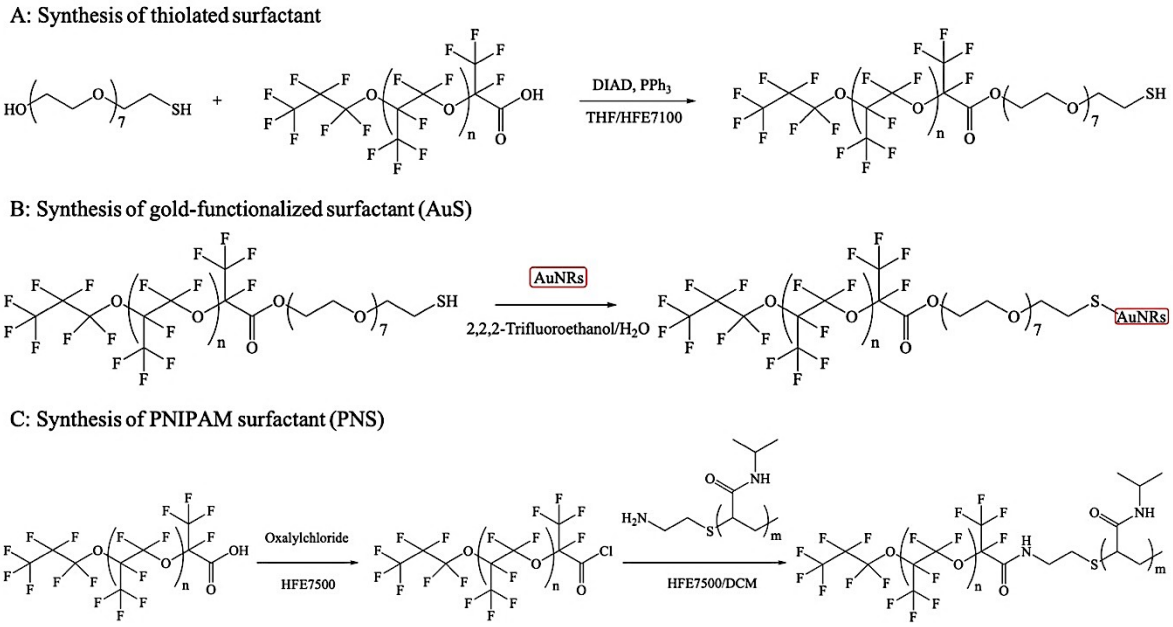

FIGURE 5.2 *SYNTHETIC PROCEDURE FOR SURFACTANT PREPARATION*
Representative reaction schemes of the synthesized surfactants with neglection of potential side reactions. For all Krytox coupling reactions, pre-activation of the carboxylic acid with oxalyl chloride was performed. If not stated otherwise, the molecular weight of the used Krytox was 7000 g/mol. (A) The thiolated surfactant is produced by coupling thiol-PEG to Krytox in a Mitsunobu reaction. (B) For obtaining the gold-linked surfactant, earlier synthesized gold nanorods (red box) are covalently linked to the previously described thiolated surfactant. (C) Synthesis of PNIPAM surfactant (PNS) by coupling Krytox to amine-terminated PNIPAM. The molecular weight of the used PNIPAM-derivate was 2500 g/mol.. All presented surfactants could be successfully synthesized.

5.1.1.1 THIOLATED SURFACTANT

The synthesis of the thiolated surfactant is based on a version of the Mitsunobu reaction, in which sterically hindered substrates are converted via ultrasonication (**Figure 5.2** A) [166]. The mild reaction conditions and the specificity of the reaction ensured that

only the hydroxylic group undergoes reaction while the more reactive thiol stays intact. Additionally, the production of the thiolated surfactant via NHS chemistry was also performed. For this purpose, glutaryl chloride was first functionalized on both sides with N-hydroxysuccinimide (NHS). This linker was then to be coupled to cysteamine hydrochloride to generate the hydrophilic part of the surfactant. However, the successful coupling between cysteamine and linker was never shown, hence this production method was not considered further. Consecutively, the surfactant was obtained by coupling bifunctionalized PEG (amine and thiol functionalization) directly to Krytox by the Mitsunobu reaction. For the reaction, the educts were dissolved in the minimum amount of solvent and sonicated under N_2 atmosphere overnight.

The successful reaction between Krytox and the bifunctionalized PEG was confirmed by FTIR spectroscopy (see **Appendix Figure SI 1**). Additionally, the ability to stabilize water-in-oil droplets was tested. To this end, droplets were prepared (2.5 mM surfactant) and incubated for 72 h. Following incubation for 72 h, the droplets were still stable meaning that the thiolated surfactant indeed stabilizes water-in-oil droplets (**Figure 5.3**).

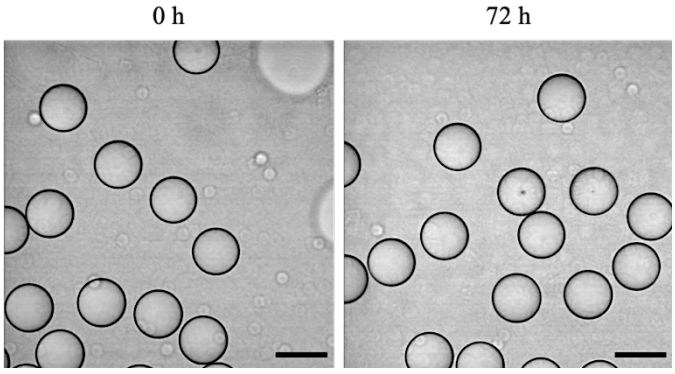

Figure 5.3 *Determination of the Stability of Droplets Stabilized with the Thiolated Surfactant*
The droplets were prepared with 2.5 mM thiolated surfactant and PBS as aqueous phase. Following, droplets were incubated for 72 h to assess the stabilizing ability of the synthesized thiol-surfactant. Droplets directly after production or after 72 h incubation are shown. The stability of the droplets during 72 h incubation was demonstrated. Scale bar: 50 µm.

Following the synthesis of the thiolated surfactant, I proceeded with coupling of gold nanorods to the thiolated surfactant. The obtained gold-linked surfactant could then be used for the linking of PNIPAM to the droplet periphery, thus allowing the formation of the cortical cytoskeleton structure.

5.1.1.2 Gold-Functionalized Surfactant

After the successful synthesis of the thiolated surfactant, gold nanorods were linked to form the gold-functionalized surfactant (AuS; **Figure 5.2** B). For the reaction, gold nanorods were washed with DCM to remove the excess of CTAB and afterwards re-dispersed in water. The thiolated surfactant was dissolved in 2,2,2-trifluoroethanol to ensure the miscibility with the nanorod solution. The washed nanorods were afterwards sonicated in the presence of the surfactant solution under N_2 atmosphere for 4 h. Following, the solution was kept undisturbed for 16 h to allow the formation of gold-linked surfactant. After incubation overnight, two phases occur: One colorless aqueous phase and one purple surfactant phase. The phases were separated, the oil phase was dried under reduced pressure, the residue was dissolved in HFE 7100 and filtered. The gold-linked surfactant was afterwards dried again under reduced pressure. The gold surfactant was characterized by FT-IR spectroscopy (see **Appendix Figure SI 2**). The successful linking of the nanorods to the thiolated surfactant was also evidenced by absorption spectra (see **Appendix Figure SI 3**).

After the synthesis of the gold-linked surfactant, the functionalization of the gold nanorods using a thiolated crosslinker was performed. As thiolated crosslinker, N,N'-bis(acryloyl)cystamine was used. In a next step, droplets with AuS, PNS and a polymerization solution containing the NIPAM monomer and BIS as further crosslinker were produced and the droplets afterwards polymerized to generate the synthetic PNIPAM cortex. However, the produced droplets were not stable, as the used gold nanorods led to bursting of the droplets, due to the relatively large dimensions of the rods (35 nm × 10 nm) and the resulting accumulation of inorganic components at the droplet interface. This accumulation led to the destabilization and bursting of the droplets. If gold nanoparticles should be attached to the droplet periphery, small sized particles (~ 5 nm) need to be used. However, a surfactant to immobilize gold particles was successfully synthesized and the effective coupling of gold nanorods to the thiol-functionalized surfactant was shown.

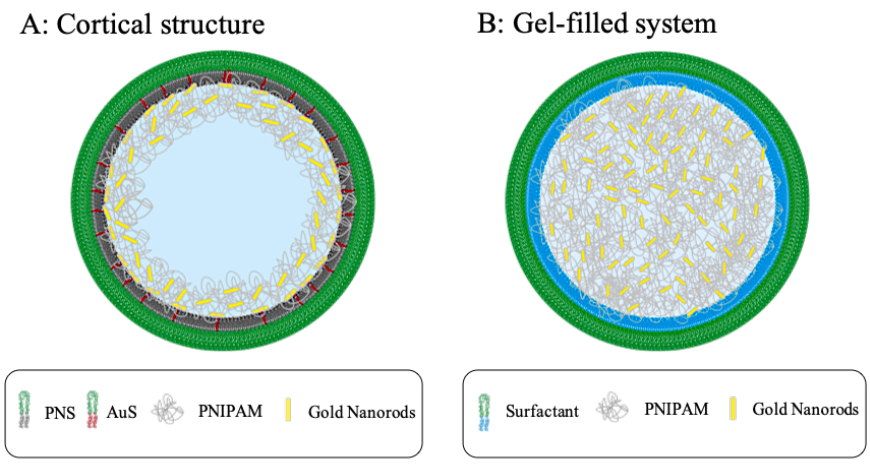

FIGURE 5.4 *COMPARISON OF DIFFERENT PNIPAM PRESENTATION MODES WITHIN THE DROPLET CONFINEMENT*
Representative sketches of the initially planned cortical structure (A) and the implemented gel-filled system (B). Surfactants are pictured in green (hydrophobic part) and either grey, red or blue (hydrophilic part). PNIPAM is shown in light grey and gold nanorods are presented in yellow. Both presented PNIPAM distributions mimicking naturally occurring actin distributions in mammalian cells.

Nevertheless, the cortical arrangement of the artificial cytoskeleton (**Figure 5.4** A) was not considered further and instead PNIPAM/gold nanorod composite filled droplets were generated (**Figure 5.4** B). This evenly distribution of the artificial cytoskeleton in the water-in-oil droplets is resembling the distribution of actin in the natural cell and is leading, due to a higher amount of thermo-responsive material within the droplets to a stronger response of the system during polymer volume transition. Independent of the change of polymer distribution within the synthetic cells, the PNIPAM-based surfactant (PNS) was further investigated due to its potentially interesting thermo-responsive properties and is therefore discussed in more detail in the next section.

5.1.2 PNIPAM-CONTAINING SURFACTANT – SYNTHESIS AND CHARACTERIZATION

A surfactant is characterized by its amphiphilic character, meaning that it consists of a hydrophilic and a hydrophobic part. In order to enhance the interactions between the encapsulated PNIPAM-based cytoskeleton and the droplet periphery, thermo-responsive PNIPAM was incorporated as hydrophilic part in a surfactant. As hydrophobic tail, a perfluorinated polyether was used.

5.1.2.1 Synthesis

The synthesis of the PNIPAM-based surfactant (PNS) was accomplished by a method reported elsewhere [155] with slight modifications in the purification protocol (**Figure 5.2** C; see **Section 4.1.1**). To obtain the surfactant, amine-terminated PNIPAM was coupled to oxalyl chloride activated Krytox in two steps. After 20 h coupling time, the solvent was removed, the residue dissolved in HFE7100 and the surfactant solution was purified by filtration to remove the colorless precipitate that was formed during the reaction. The purified surfactant could be obtained with a good yield of 87% as colorless highly viscous oil with an average mass of 9000 g/mol (see **Appendix SI 6**).

Afterwards, the surfactant was characterized by FTIR spectroscopy and partitioning experiments. The purity of the surfactant was further analyzed using NMR spectroscopy.

5.1.2.2 Chemical Characterization of PNS

In the following section, the characteristics of the surfactant synthesis, namely the determination of purity and conversion, are displayed in more detail. These characteristics were determined using different methods, such as FTIR and NMR spectroscopy for assessment of purity and partitioning experiments for the determination of conversion rates. The mass distribution of the synthesized surfactant was obtained by MALDI-TOF MS spectroscopy (see **Appendix SI 6**).

5.1.2.2.1 NMR Analysis

NMR spectra of PNS (**Figure 5.5**) were recorded in a mixture of 3:0.7 of $CDCl_3$ and 2,2,2-trifluoroethanol-d_3 due to low solubility of the surfactant in well-established solvents like chloroform or DCM. Chemical shifts are given in ppm referenced to standard solvent ($CDCl_3$, δ = 7.26 ppm for ^1H) [167] and coupling constants are given in Hz. In the presented data, singlets are referred to as s, duplets as d and multiplets as m.
^1H NMR: δ = 1.111 (6H, CH_3, d, J = 0.4); 1.252-1.317 (1H, CH, m); 1.501-1.586 (2H, CH_2, m); 3.804-3.878 (1H, CH, m); 3.935 (1H, CH, s).

NMR analysis was performed to confirm successful coupling of PNIPAM to Krytox. The peak at 4.350 ppm is caused by traces of unreacted Krytox. Nevertheless, the existence of specific PNIPAM peaks in the spectrum proves a successful reaction, since the NMR spectrum was recorded after purification by filtration and PNIPAM itself is not soluble in HFE7100.

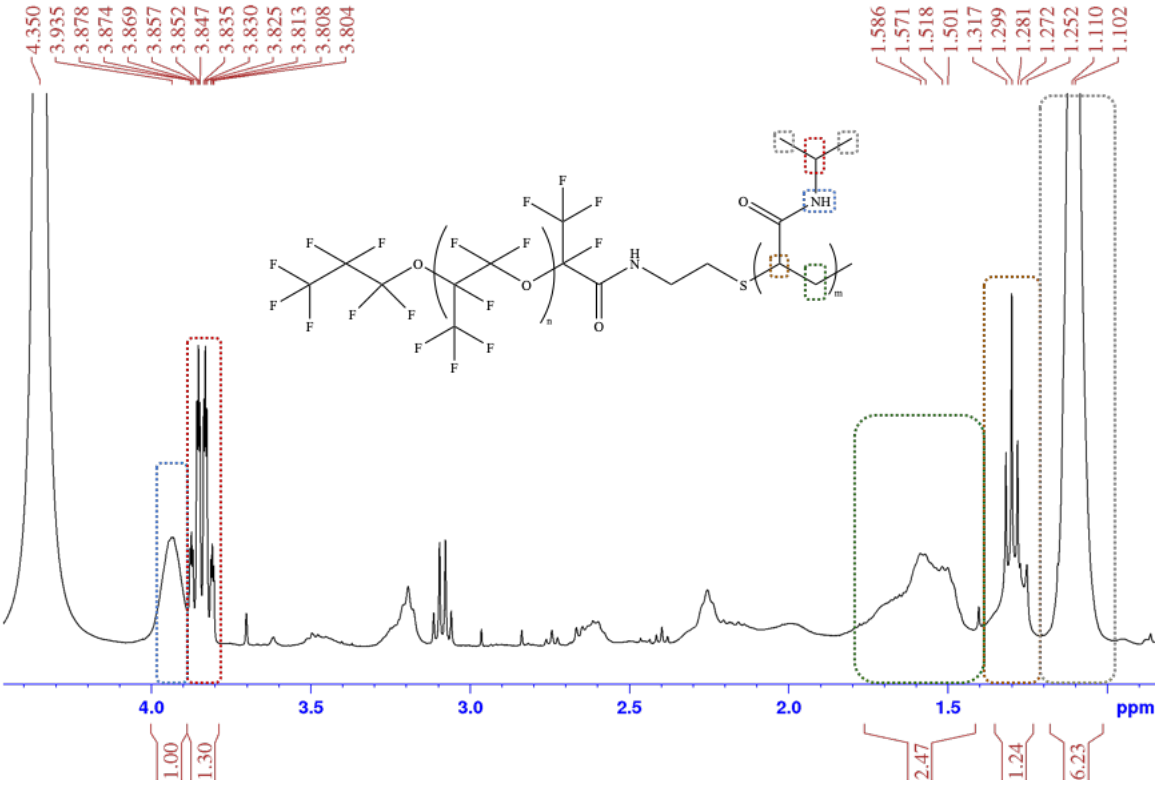

FIGURE 5.5 *^{1}H NMR SPECTRUM OF PNS*
NMR spectrum of PNS. The assignment of characteristic peaks is realized with the help of colored boxes directly in the spectrum and the corresponding structural formula. Chemical shifts are given in ppm. Due to specific PNIPAM peaks in the ^{1}H NMR spectrum, the successful coupling to Krytox was shown.

5.1.2.2.2 FTIR ANALYSIS

Representative FTIR spectra of PNIPAM-containing surfactant (PNS) and the PFPE7000-carboxylic acid (Krytox) synthesis starting material are presented in **Figure 5.6**. The wavenumber is given in cm^{-1} and the transmission is given in %.

The spectra show major peaks at 1650, 1740, 1775, 2880-2970 and 3090 cm^{-1}. The peak at 1775 cm^{-1} corresponds to the stretching mode of the (C=O) bond of PFPE-carboxylic acid [195] that is not only present in the starting material but also slightly shifted in the PNS product (60 cm^{-1} shift, black box). This indicates that traces of the starting material are still contained in PNS. In order to evaluate the amount of Krytox starting material contained in the synthesized surfactant, partitioning experiments were performed (see the following Section). The bands at 1650 and 1740 cm^{-1} are assigned to two different (C=O) groups incorporated in the PNIPAM structure (red box) [196]. The bands between 2880-2970 cm^{-1} represent the (C-H) valence vibrational mode of the (CH_2) groups in PNIPAM [196]. The peak at 3090 cm^{-1} represents the stretching mode of the (N-H) groups

[196]. Additionally to findings previously shown by NMR spectroscopy, specific PNIPAM bands were also found in the FTIR spectrum, proving the successful synthesis of PNS.

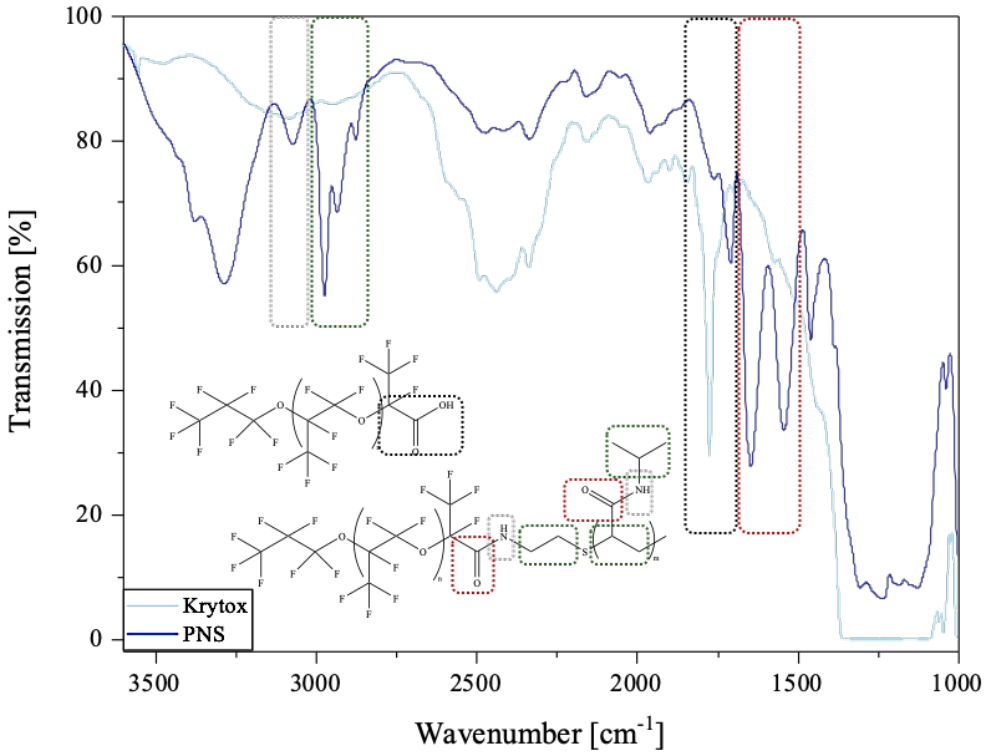

FIGURE 5.6 *REPRESENTATIVE FTIR SPECTRUM OF PNS*
Overlay of FT-IR transmission spectrum of PNS (dark blue) and Krytox (light blue). Both compounds were measured as pure substances. Wavenumber is given in cm^{-1} and transmission in %. Characteristic bands are marked in the spectra and the chemical structures by colored boxes, respectively. The characteristic PNIPAM bands confirm, in addition to NMR analysis, the successful synthesis of the PNIPAM-based surfactant.

5.1.2.2.3 PARTITIONING EXPERIMENT

Partitioning experiments were performed (for more details see **Section 4.1.2.3**) in order to determine the Krytox level in PNS. This was done by correlating the measured absorption of the aqueous Rhodamine 6G solution layered on top of the surfactants to a Krytox concentration given by the calibration curve (**Figure 5.7** B).

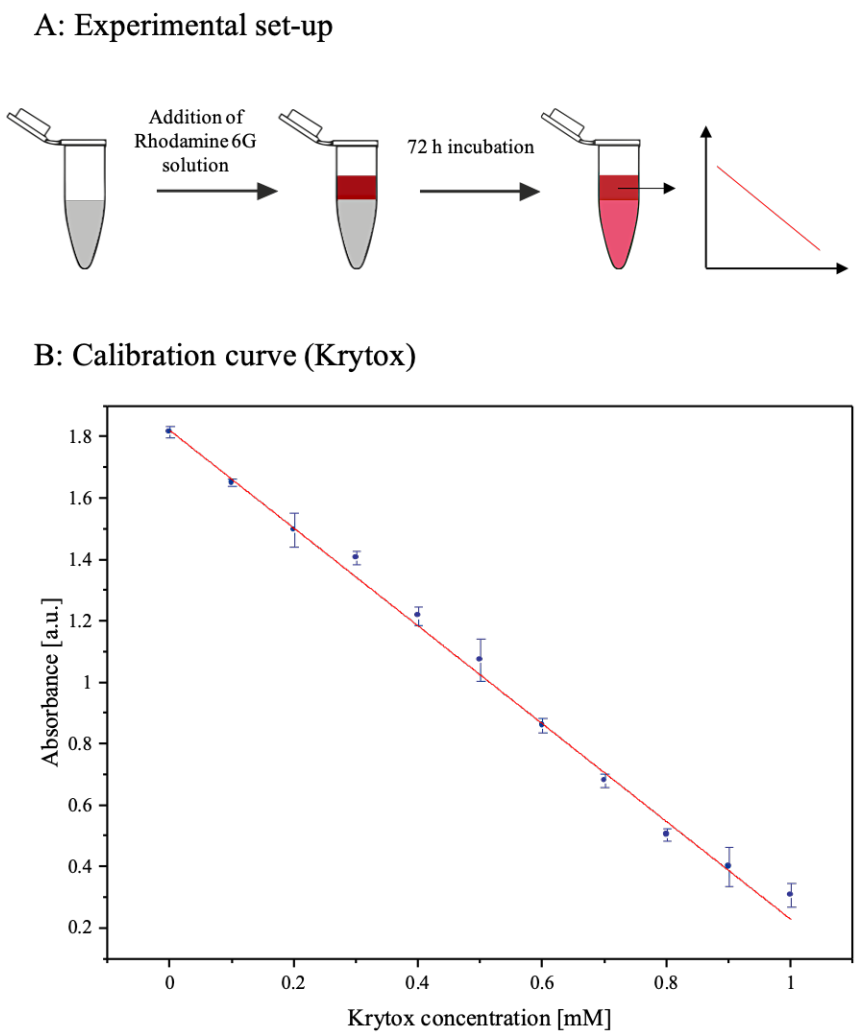

FIGURE 5.7 *PARTITIONING EXPERIMENT*
(A) Schematic representation of experimental set-up of Krytox partitioning experiment. The oil phase (shown in grey) either contains pure Krytox or pure surfactant. The Rhodamine 6G (Rho6G) solution is depicted in dark red and the oil phase after the reaction with Rho6G is shown in light red. (B) Representative calibration curve of partitioning experiment acquired for pure Krytox. The measured values are shown in blue, the linear fit of the data is shown in red. The concentration dependent reaction between Krytox and Rhodamine 6G is characterized through change of the absorption values. For analysis, the absorption values of Rhodamine 6G in the aqueous phase were used for either constructing the calibration curve or the determination of Krytox levels in the surfactants. Measurements were performed in triplicates in technical repeats (n = 4) and the standard deviation is shown. With this, the Krytox levels in the synthesized and the commercial surfactant were determined.

Afterwards, the amount of Krytox (n(Krytox)) contained in the samples was calculated and the ratio between calculated amount of Krytox and the amount of surfactant was formed. The determined Krytox levels and the used formula are listed below (**Table 5.1, eq. 5.1**). For the commercial fluorosurfactant (1.4 wt%), a concentration of 3.5 mM based on ref. [161] was assumed.

$$w_{Krytox}[mol\%] = \frac{n_{Krotox,sample}}{n_{Surfactant}+n_{Krytox,sample}} * 100\% \qquad \text{(eq. 5.1)}$$

TABLE 5.1 KRYTOX LEVELS IN SURFACTANTS

SAMPLE NAME	AMOUNT OF KRYTOX [MOL%]
Commercial fluorosurfactant (CS)	(3.3 ± 0.2)
PNIPAM surfactant (PNS)	(56.0 ± 2.3)

The high level of Krytox in the synthesized surfactant suggests an incomplete reaction. In order to enhance the conversion rate, the amount of amine-terminated PNIPAM (1.5 eq) was increased in order to shift the reaction further towards the product side. However, higher Krytox levels were detected (Krytox level: 59.8 ± 6.5 mol%). This indicates a side reaction of activated PFPE-carboxylic acid to the anhydride, which in the subsequent reaction with amine-terminated PNIPAM reacts in equal parts to product and Krytox as by-product. To support this hypothesis, oxalyl chloride was subsequently not removed from the reaction mixture after the reaction with Krytox and was thus available to activate the potentially formed free PFPE-carboxylic acid. However, the reduction of the product quantity in favor of the Krytox quantity (74.7 ± 2.9 mol% Krytox) was observed. Although this is not a conclusive evidence against the anhydride as a potential intermediate, it might be an indication of a potentially different reaction route.

Independent on the used synthesis route, a purification of the obtained surfactant is not trivial. Components that are not soluble in fluorinated oils are easily removable by filtration, but unreacted Krytox is quite impossible to remove since common purification methods like flash column chromatography are not applicable because of a strong interaction of the fluorinated part of the surfactants with the column material. Also finding the correct solvents and solvent mixtures for the purification by column chromatography is a time consuming process that is not necessarily leading to satisfying results. Therefore, the removal of Krytox from the synthesized surfactant was not performed. However, the high level of negative charge in PNS due to Krytox can be advantageous when recruitment of positively charged molecules to the droplet periphery is required.

After the surfactant was characterized with regard to its chemical properties, the physical properties were examined in more detail. As the surfactant was to be used as a synthetic plasma membrane analogue, the interfacial tension was determined.

5.1.2.2.4 Pendant Drop Tensiometry

To obtain a clear idea of the physiochemical properties of the synthesized surfactant with respect to its behavior in microfluidic processes, pendant drop tensiometry measurements were performed to evaluate the interfacial tension (IFT). Interfacial tension is a phenomenon that results from the difference in energy levels between molecules located at the fluid interface when compared to their bulk counterparts. Accordingly, molecules at the interface have fewer attractive interaction partners therefore forming the smallest possible intersection without the action of external forces [169]. Besides the synthesized PNS surfactant, a commercially available fluorosurfactant (CS) was also analyzed with respect to the potential application as plasma membrane analogue.

The obtained data show a relative high IFT value of the synthesized PNS surfactant compared to the commercial surfactant (CS), namely 27.006 mN/m compared to 10.428 mN/m at 25 °C (**Figure 5.8**). In contrast, compared to pure FC-40 oil ((49.964 ± 0.081) mN/m), a reduction in interfacial tension is observable meaning that both surfactants reducing the surface tension and, therefore are stabilizing the droplet system. Nevertheless, high surface tension values indicate that a stronger force must be applied to deform the droplets.

Comparing the temperature behavior of synthesized and purchased surfactant (**Figure 5.8**), a reduction of the IFT values for both surfactants is observed (difference between mean IFT values approximately ± 3 mN/m). However, contrary to expectations, no differences in the temperature-response behavior of PNS and CS were observed. The thermo-responsive PNIPAM moiety in PNS was expected to facilitate the further decrease of the IFT value due to the collapse of the PNIPAM chains and a corresponding higher surface coverage due to the smaller dimensions of the surfactant. Despite the expectations, the thermo-responsive PNIPAM moiety has no influence on the temperature response of the surfactant in the measured temperature range. This behavior can be explained due to the decrease of the transition temperature of PNIPAM caused by coupling to a hydrophobic tail, which is already described for other PNIPAM-containing surfactants [170]. The decrease of the transition temperature thereby means, that the surfactant is already in its collapsed state and the further increase of temperature cannot cause a further collapse. As a consequence, the IFT value changes during temperature increase following the trend described by Eötvös law [171], namely the IFT decrease upon temperature increase.

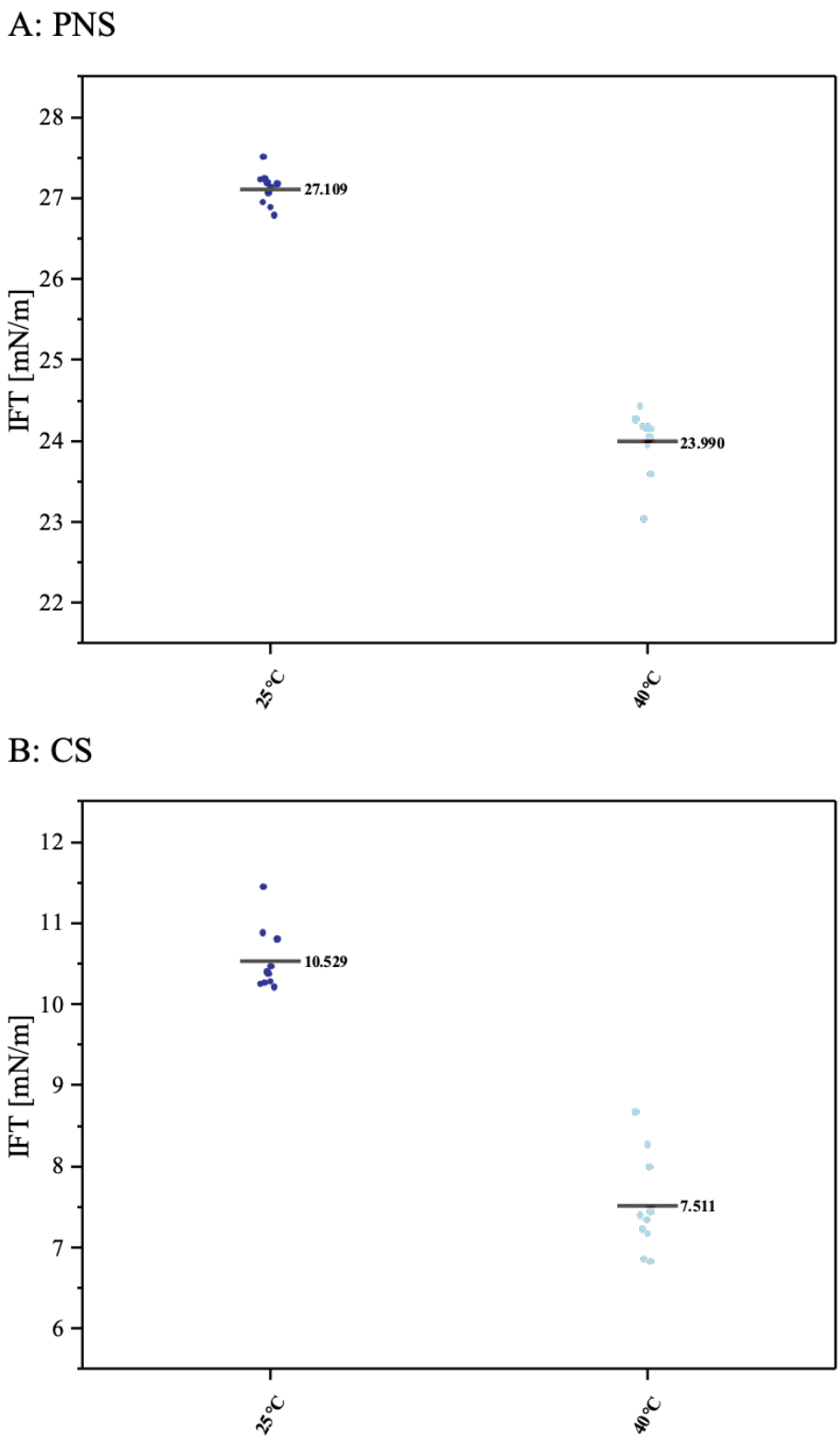

FIGURE 5.8 *INFLUENCE OF TEMPERATURE ON THE INTERFACIAL TENSION*
Interfacial tension (IFT) of surfactants was determined using pendant drop tensiometry. All surfactants were dissolved in FC-40 up to a final concentration of 2.5 mM in case of PNS and 1.4 wt% in case of CS. For all samples, 10 individual droplets were measured and the single data points and the mean displayed in the plots. (A) The influence of temperature on PNS behavior. As control without thermo-responsive moiety, CS was also measured (B). The behavior of both surfactants upon temperature changes, more precisely the decrease of the IFT values, was shown.

To proof the thermo-responsiveness of PNS, pendant drop tensiometry measurements at temperatures below 25 °C need to be performed in order to detect if the coupling of Krytox to PNIPAM caused a decrease of the transition temperature. Additionally, dynamic light-scattering (DLS) measurements above the CMC of the surfactant at different temperatures can be executed in order to observe changes in micelle size due to PNIPAM volume transition. However, since the synthesized surfactant was never used below 25 °C, no further considerations concerning the behavior at low temperatures were made.

Since the partitioning experiments revealed a certain amount of Krytox educt in PNS, the IFT values for Krytox at 25 and 40 °C were determined (**Figure 5.9**). Interestingly, no difference between the IFT values at 25 °C and 40 °C were observed. This result is contrary to findings described by Eötvös law, which states that a linear decrease of the interfacial tension can be expected with increasing temperature [171]. An explanation for this particular finding is the fact that Krytox is a highly polar molecule for which the Eötvös law is not implicitly applicable [172]. The fact that this behavior is not seen in PNS could be explained by the introduction of a less polar molecule (PNIPAM) into the surfactant structure. Nonetheless, to which extent the behavior of Krytox influences the temperature behavior of PNS cannot be determined on the basis of the collected data. Nevertheless, the IFT values of PNS, Krytox and CS at 25 and 40 °C were successfully determined.

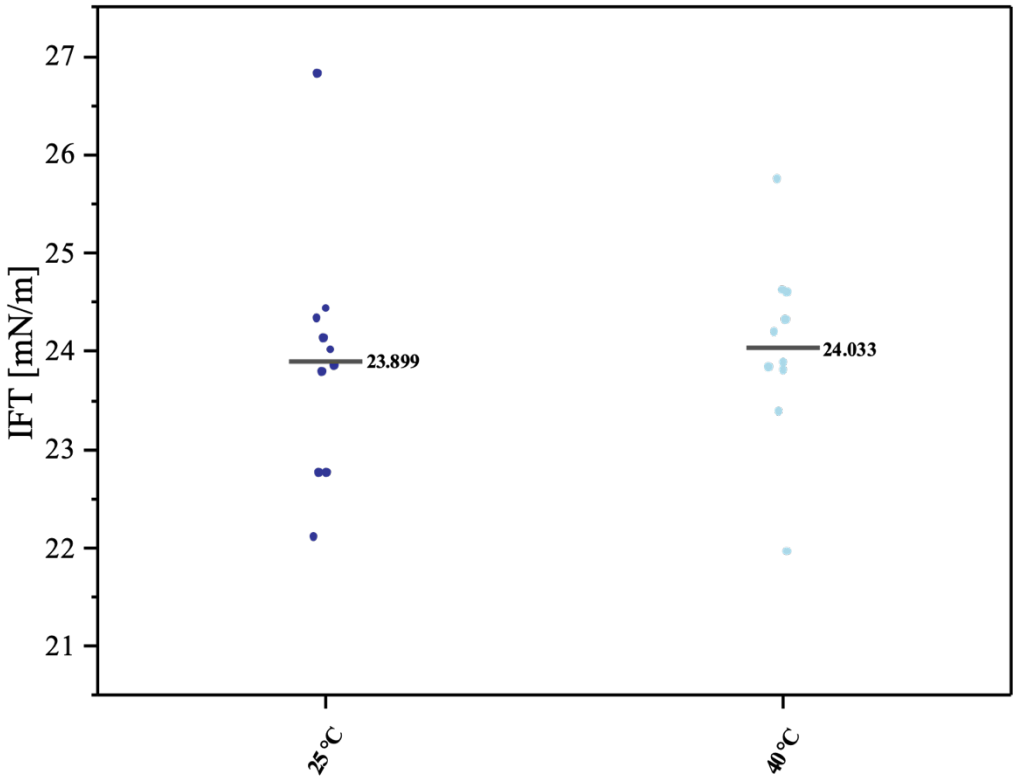

FIGURE 5.9 *TEMPERATURE RESPONSE OF KRYTOX*
Interfacial tension (IFT) of Krytox was determined using pendant drop tensiometry. For the measurements, Krytox was dissolved in FC-40 up to a final concentration of 2.25 mM. For all samples, 10 individual droplets were measured and the single date points and the mean displayed in the plot. IFT values acquired at 25 °C are shown in dark blue, values captured at 40 °C are shown in light blue.

In order to be able to make a better statement regarding the behavior of the surfactants in interaction with the encapsulated composite hydrogel, measurements with 100 µM carboxylic acid-terminated PNIPAM solution as aqueous phase were carried out in addition to the series of measurements in Type 1 water (**Figure 5.10**). Note, a relatively low concentration of PNIPAM was used (100 µM) due to the temperature-induced turbidity of the solution and the interference with the optical method used for IFT determination. However, significant IFT changes could already be achieved with this low amount of PNIPAM.

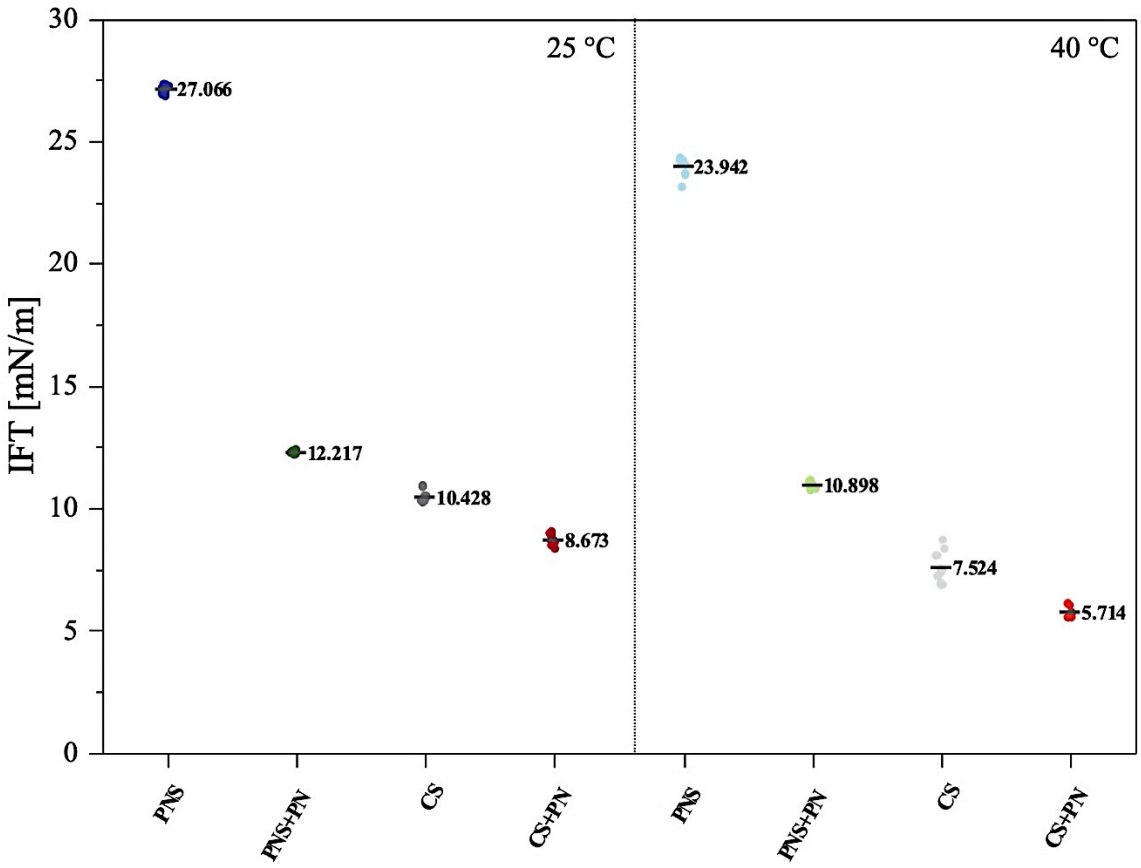

FIGURE 5.10 *INFLUENCE OF SYSTEM COMPONENTS ON PNS INTERFACIAL TENSION VALUES*
Interfacial tension (IFT) of surfactants was determined using pendant drop tensiometry. All surfactants were dissolved in FC-40 up to a final concentration of 2.5 mM in case of PNS and 1.4 wt% in case of CS. For all samples, 10 individual droplets were measured and the single measurements and the mean displayed in the plots. IFT measurements of PNIPAM surfactant (PNS) and commercial fluorosurfactant (CS) are shown. The surfactants were measured against two different aqueous phases, Type 1 water and 100 µM PNIPAM-COOH (PNIPAM) at two different temperatures (25 °C and 40 °C). Measurements at 25 °C are indicated by dark colors in the graph, those at 40 °C in light colors. The decrease of IFT values due to dissolved PNIPAM was shown for both surfactants, whereas the effect was stronger represented in case of PNS.

The measurements showed that the addition of PNIPAM led to a dramatic decrease in interfacial tension for the synthesized PNS, while for CS only a small decrease is observable. A summary of the obtained IFT values for the different tested conditions is given below (**Table 5.2**). The reduction of interfacial tension, which is stronger pronounced in PNS (mean difference of ± 14 mN/m compared to ± 2 mN/m), is independent from the system's temperature. This behavior arises due to a higher degree of interaction between dissolved and bound PNIPAM, which is intended to facilitate a better linkage of the PNIPAM gel to the droplet periphery. Although this result gives the impression that PNIPAM alone could be sufficient to stabilize water-in-oil droplets, no stable droplets could be generated without the addition of surfactant (see **Appendix Figures SI 12** and **SI 5**).

TABLE 5.2 SUMMARY IFT VALUES

TEMPERATURE	SURFACTANT	SURROUNDING PHASE	IFT [MN/M][A]
25 °C	PNS	Water	27.066 ± 0.195
	1.4 wt% CS		10.428 ± 0.373
	5 wt% CS		8.917 ± 0.190
	PFPE-carboxylic acid		23.899 ± 1.220
	FC-40		49.964 ± 0.081
	PNS	100 µM PNIPAM (carboxylic acid terminated)	12.217 ± 0.128
	1.4 wt% CS		8.673 ± 0.318
	PNIPAM-COOH[b]	FC-40	22.617 ± 0.045
40 °C	PNS	Water	23.942 ± 0.382
	1.4 wt% CS		7.524 ± 0.573
	5 wt% CS		6.898 ± 0.464
	PFPE-carboxylic acid		24.033 ± 0.925
	FC-40		50.644 ± 0.094
	PNS	100 µM PNIPAM (carboxylic acid terminated)	10.898 ± 0.120
	1.4 wt% CS		5.714 ± 0.240
	PNIPAM-COOH[b]	FC-40	18.773 ± 0.040

[a]IFT values of 10 individual droplets were averaged. Additionally, the standard deviation is given
[b]PNIPAM-COOH concentration of 100 µM was used

The IFT measurements showed that both surfactants, namely CS and PNS are capable of stabilizing water-in-oil emulsion droplets, both at 25 and 40 °C. Besides, the stronger interaction between dissolved PNIPAM and PNS was shown, which was used to create a link between the encapsulated artificial cytoskeleton material and the droplet periphery.

Following the physical and chemical characterization of the surfactants, the systems' components necessary for the assembling of the artificial cytoskeleton were prepared and characterized either as single components or in combination.

5.1.3 PNIPAM/Gold Composite Material

In order to induce PNIPAM volume transition triggered by light irradiation, gold nanorods that are capable of plasmon resonance were embedded into the thermally triggerable PNIPAM matrix.

5.1.3.1 Golds Nanorods – Implementation of Light-Triggerable Moieties

Gold nanorods were produced via a seed-mediated growth process (**Figure 5.11** A; see **Section 4.2.1**). At first, spherical particles with a size of approx. 5 nm were produced (seed solution) and then grown into rod-shaped particles in a growth solution containing silver nitrate and 5-bromosalicylic acid in addition to more gold salt. As stabilizing reagent for the seed solutions as well as for the rod-shaped particles, CTAB was used. Both, CTAB and 5-bromosalicylic acid are crucial for the stabilization of the rod-shape. The size of the rods is controlled by the concentration of silver nitrate but can be also influenced by hydrochloric acid, potassium bromide or salicylic acid [173, 156]. The purification of gold nanorods was performed by centrifugation to remove reaction components and unbound CTAB. After purification, the nanorods were analyzed by UV Vis and TEM measurements.

The measurements revealed that besides the desired nanorods, also spherical particles were generated that could not be separated by centrifugation. Those nanosphere impurities are visible as little shoulder of the peak stated around 500 nm in the UV Vis spectrum and in TEM micrographs. The obtained nanorods have a length of (35 ± 5) nm and a width of (10 ± 1) nm (**Figure 5.11** B) with an absorption maximum of (752 ± 9) nm (**Figure 5.11** C) and were synthesized in a reproducible manner over various batches (see **Appendix Figure SI 4**).

The gold nanorods (9.50×10^5 rods/ml; for calculations see **Section 4.2.3**) were added afterwards to a NIPAM polymerization solution containing BIS as a crosslinking reagent (see **Section 4.4.1**). Following polymerization, the LCST behavior and the sol content of the obtained PNIPAM/gold nanorod composite hydrogel was investigated.

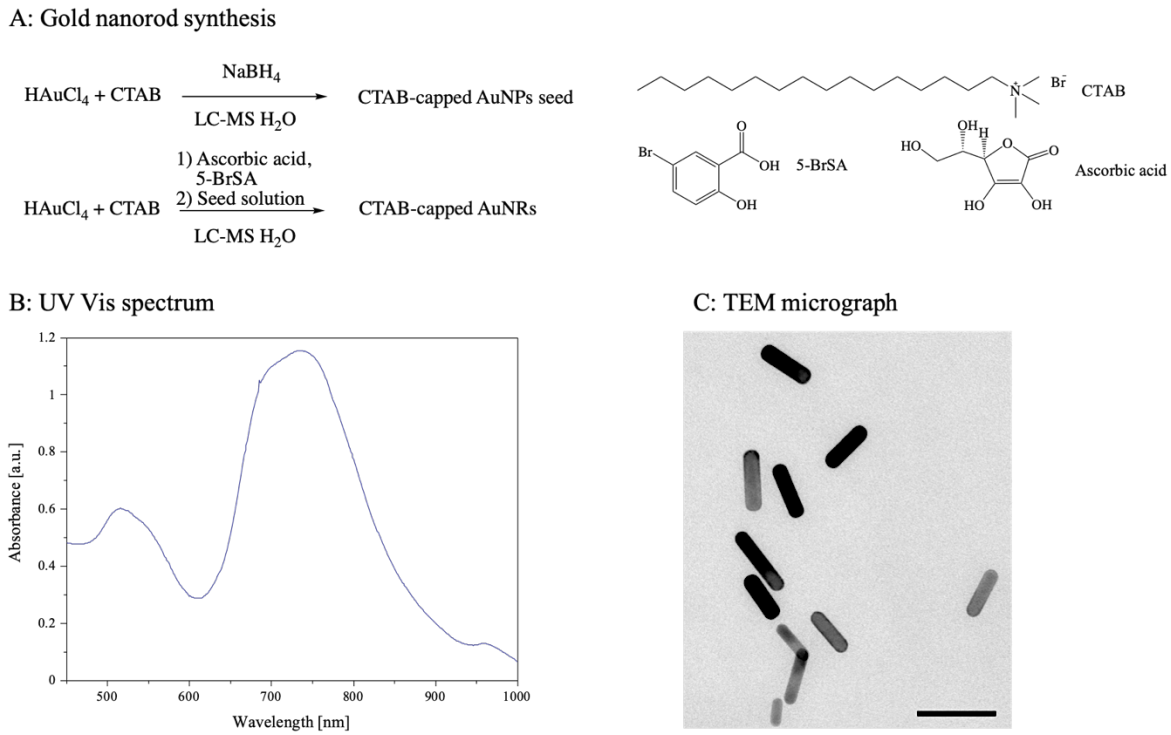

FIGURE 5.11 *SYNTHESIS AND CHARACTERIZATION OF GOLD NANORODS*

(A) Schematic representation of gold nanorods synthesis. Structural formulas of some compounds used during synthesis are depicted on the right side. (B) Representative UV Vis absorption spectrum of gold nanorod solution after purification. The absorption maximum located around 750 nm corresponds to the absorption of the long axis of the nanorod, while the secondary maximum around 520 nm is characteristic for its short axis absorption. (C) Representative TEM micrographs of gold nanorods. For determination of nanorod dimension, 20 individual rods were analyzed. Gold nanorods with a length of (35 ± 5) nm and a width of (10 ± 1) nm were obtained in a reproducible manner. Scale bar: 50 nm.

5.1.3.2 PNIPAM GEL MATRIX

The polymer matrix used was examined both in terms of its degree of polymerization and its temperature behavior.

5.1.3.2.1 DETERMINATION OF SOL CONTENT IN PNIPAM HYDROGELS

In order to first estimate the completeness of the polymerization, the sol content, meaning the non-crosslinked part of the hydrogel, was determined. The sol content was obtained by extraction of the unreacted molecules and calculated afterwards using **eq. 4.6**. The evaluation of the sol content is depicted hereinafter (**Figure 5.12**, **Table 5.3**).

$$w_{Sol}[\%] = \left(1 - \frac{m_{dry-washed}}{m_{dry-untreated}}\right) * 100\% \qquad \text{(eq. 4.6)}$$

To determine the sol content, the 2 ml reaction vessels were weighed first, then the gels were polymerized and, after polymerization, frozen and dried. After freeze-drying and weighing, the gels were incubated with 1.5 ml water over night, before removing the excess of water. Afterwards, the gels were again freeze-dried and weighed.

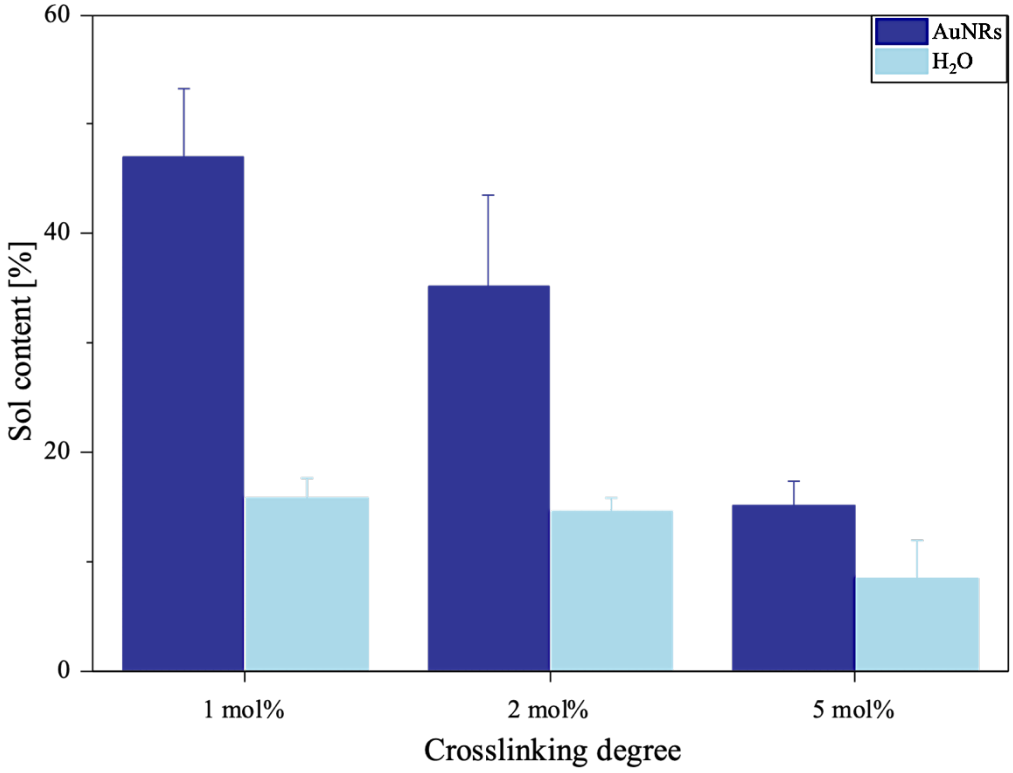

Figure 5.12 *Graphical Representation of Sol Content in PNIPAM Hydrogels*
Sol content of PNIPAM hydrogels is plotted against its crosslinking degree. As crosslinker, N,N'-methylenbisacrylamide (BIS) was used. The concentration is given in relation to the used NIPAM concentration. For all hydrogels, a NIPAM concentration of 1 M was used. Hydrogels prepared with gold nanorods (AuNRs) are depicted in dark blue, hydrogels without gold in light blue. All samples were prepared in triplicates and in technical repeats (n = 3). The mean and the standard deviation is shown.

Table 5.3 *Sol Content of PNIPAM Hydrogels*

Amount of Crosslinker	Sol Content [%]	
	AuNRs	H_2O
1 mol% BIS	47.00 ± 6.22	15.86 ± 1.73
2 mol% BIS	35.10 ± 8.42	14.60 ± 1.21
5 mol% BIS	15.06 ± 2.43	8.38 ± 3.48

Comparing the obtained results a clear, crosslinker concentration dependent trend can be seen in all tested samples, meaning that a higher crosslinker concentration is leading

to a lower sol content in the gels. When samples with and without gold nanorods are compared, it can be recognized that the hydrogels prepared without gold nanorods show a lower sol content. This is attributed to the fact that, besides the unreacted monomer and crosslinker molecules, also not-incorporated gold nanorods and excessive CTAB that could not be removed through centrifugation, is extracted by washing. This leads to an overestimation of the sol content of gold containing hydrogels, because the weight of the washed hydrogels is reduced to a greater extent. This hypothesis can be verified by detection of gold nanorods in the washing solution. Nevertheless, the correlation between the amount of crosslinker and the polymerization degree of the prepared hydrogels either with or without gold nanorods could be shown.

After evaluation of the hydrogel forming radical polymerization reaction, the transition temperature of the gold-containing composite hydrogels was determined.

5.1.3.2.2 Transition Temperature of PNIPAM/Gold Nanorod Composite Hydrogels

The transition temperature T_T of the composite material with different compositions was determined optically. To do so, the hydrogels were polymerized inside a 96-well plate, swollen overnight and the absorption (detection wavelength: $\lambda = 680$ nm) at fixed temperatures was determined afterwards (**Figure 5.13**). Before absorption measurements, the hydrogels were equilibrated for 5 min. Besides testing the influence of the embedded gold nanorods on the polymer transition behavior, also the effect of different NIPAM and BIS concentrations was investigated.

For determination of the influence of monomer concentration on the temperature-induced PNIPAM transition behavior, hydrogels comprised of 4 different monomer concentrations (0.125 M, 0.25 M, 0.5 M and 1.0 M) were produced. The BIS concentration was kept constant at 1 mol%. When addressing the effect of crosslinking degree, 3 different BIS concentrations (1 mol%, 2 mol% and 5 mol%) were tested while the NIPAM concentration (0.5 M) was kept constant. In all samples, the amount of photoinitiator was 0.6 wt% and the gold nanorod concentration was fixed. Since PNIPAM is a well-known material, hydrogels without gold nanorods were not prepared. Instead, unpolymerized samples were used as control to exclude any effect of temperature alone (see **Appendix Figure SI 7**). The phase transition temperature is given by the maximum of the first

derivative of the temperature-absorption curves and can be derived from the graphs (see **Section 4.9**).

The transition temperature of the composite hydrogel is neither influenced by the gold nanorods nor by the amount of used monomer (**Figure 5.13** A) and is stated around (31.2 ± 0.3) °C for all tested concentrations. This temperature is in agreement with the value for pure PNIPAM found in literature [174]. When comparing samples with high and low monomer amounts it can be seen that the higher the monomer concentration the weaker is the temperature response of the corresponding hydrogels (flatter temperature response curves caused by lower absorption values). This finding is caused by the fact that contraction of the polymer during phase separation is hindered by high amounts of material thus leading to smaller volume changes and accordingly to a reduced turbidity of the collapsed hydrogels. Therefore, subsequent experiments were performed with a monomer concentration of 0.5 M NIPAM. This concentration represents the optimal compromise between sufficient amount of polymer material and sufficient temperature response.

The transition temperature, however, is highly changeable by the amount of used crosslinker (**Figure 5.13** B) ranging from around 30.6 °C for the lowest amount of crosslinker to 34.4 °C for the highest concentration. This trend is caused by an increase of hydrophilicity through increased crosslinker concentrations [175] and therefore a stronger fixation of water molecules inside the hydrogels. This stronger incorporation of the water molecules in the hydrogel structure is leading to a slower phase separation. Additionally, the introduction of non-thermo-responsive moieties into the hydrogel structure is reducing the temperature-sensitivity of the PNIPAM hydrogel [177] which is further increasing the transition temperature. This is also leading to the decrease of the absorption values when 1 mol% BIS samples are compared with 2 and 5 mol% BIS samples due to the reduced turbidity.

The successful modulation of the transition temperature of PNIPAM composite gels was shown by means of the modulation of the crosslinker concentration. Importantly, the temperature can be tuned in a way that it fits physiological range.

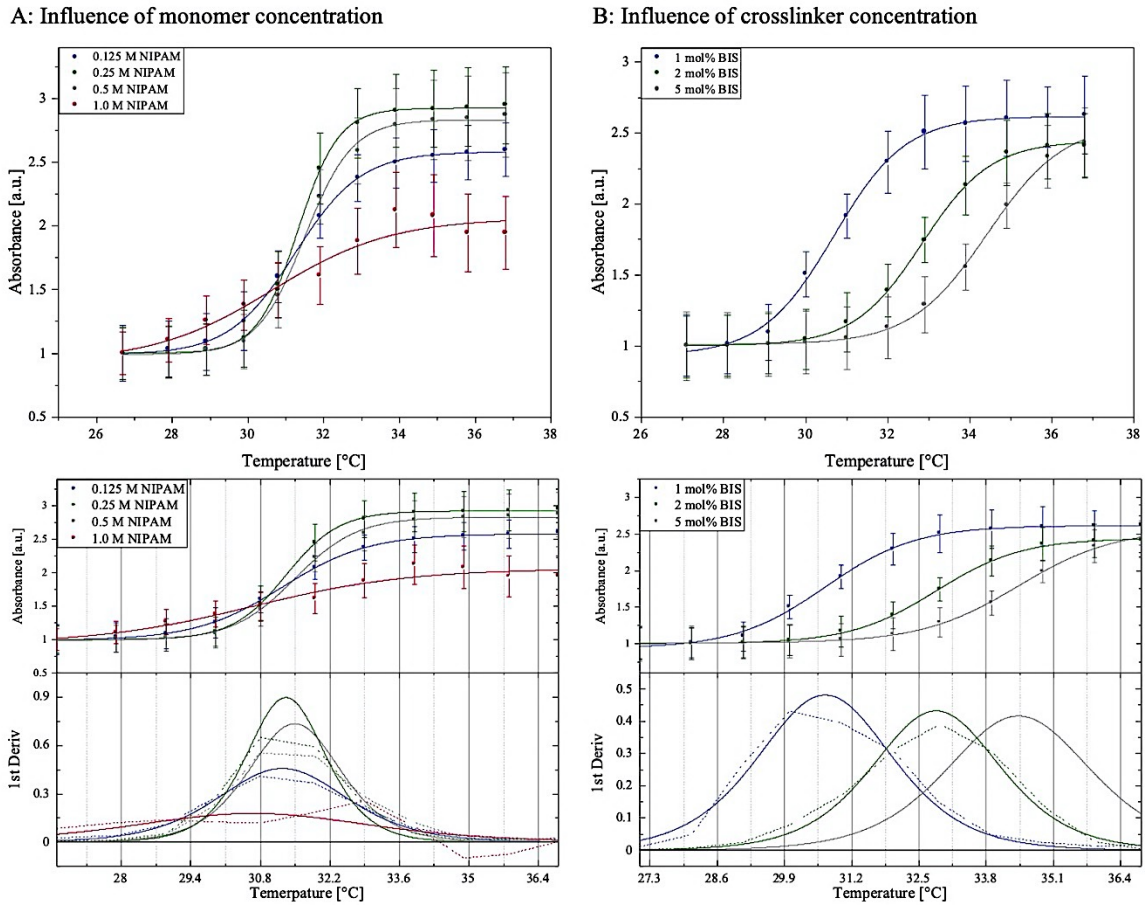

FIGURE 5.13 *TRANSITION TEMPERATURE OF PNIPAM COMPOSITE GELS*
Temperature characteristics of PNIPAM/gold nanorods composite hydrogels. For all samples the amount of gold nanorods and photoinitiator D1173 (0.6 wt%) was kept constant and the gels were swollen for 24 h. The swollen hydrogels were incubated in a plate reader and the absorption was determined at 680 nm. Every set of measurements was performed between 27 °C and 37 °C within 1 °C steps and every sample was prepared as pentaplicate. For data analysis, the absorption values were normalized to every individual well before temperature ramping. To determine the transition temperature of hydrogels in bulk, the first derivative was calculated by fitting the data with a sigmoidal "dose response fit" using Origin [159]. The displayed graphs show on the one hand the change in absorption with temperature change (top) and on the other hand the determination of the phase transition temperature using the first derivative (bottom). The dotted lines show the first derivative of the actual data at the respective temperature, while the bold lines represent the first derivative of the fit function. (A) Influence of NIPAM monomer concentration on composite hydrogel transition temperature in bulk. Hydrogels were prepared with 4 different monomer concentrations (0.125, 0.25, 0.5 and 1.0 M) with a fixed amount of 1 mol% BIS. (B) Influence of crosslinking degree on hydrogel characteristics. Hydrogels were prepared with 3 different crosslinker concentrations (1, 2 and 5 mol% BIS) with a fixed amount of monomer (0.5 M).

After examination of the factors influencing the transition temperature of the presented PNIPAM composite material, the reversibility of the transition was determined. The reversible switching of the PNIPAM volume transition would not only allow to trigger motility of the artificial cells on demand like in natural cells, but is also resembling the behavior of the natural cytoskeleton, which was aimed to mimic. Therefore, bulk hydrogels were subjected to temperature cycles (**Figure 5.14**).

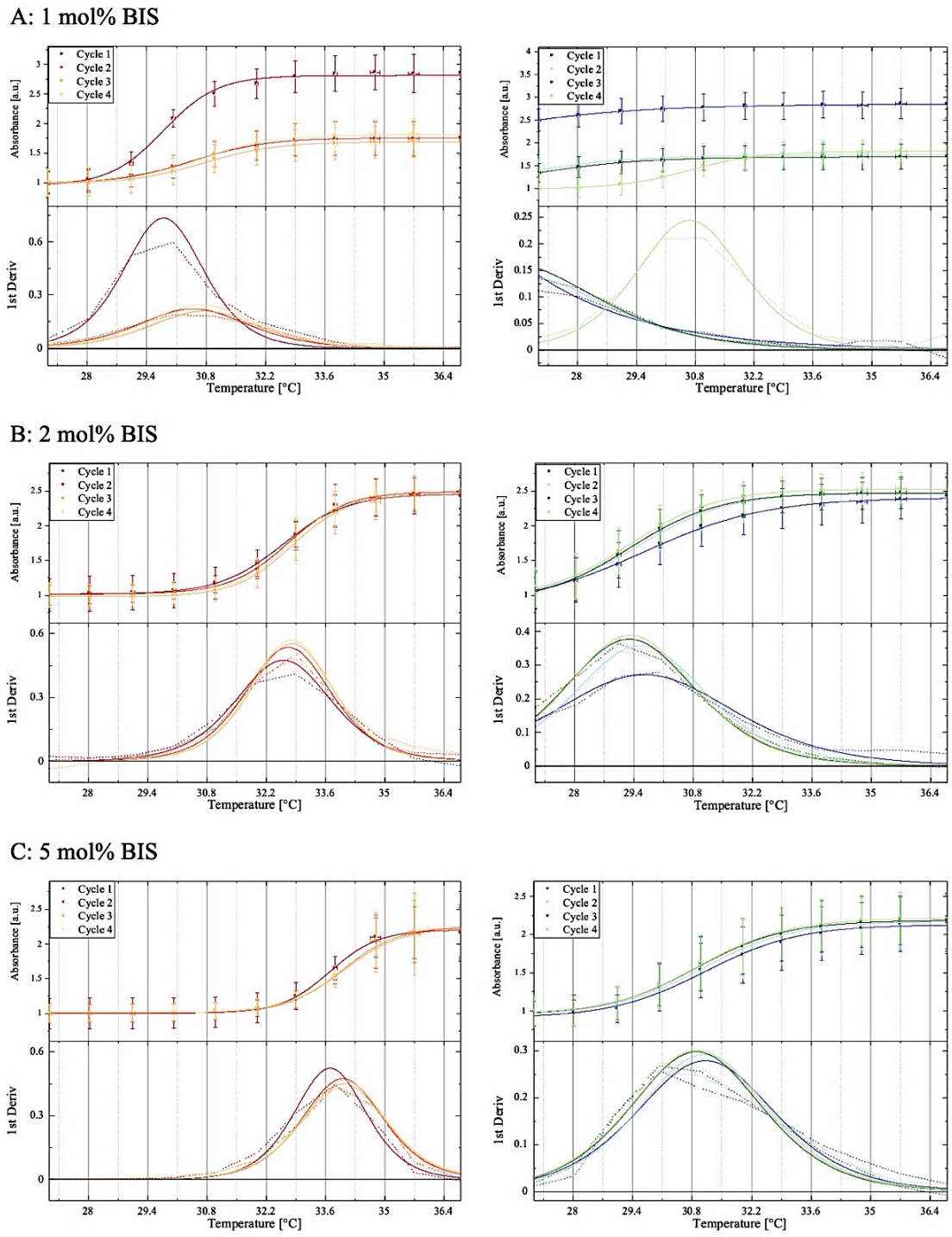

FIGURE 5.14 *REVERSIBILITY OF HYDROGEL TRANSITION*
The hydrogels containing 3 different BIS concentrations (1 mol%, 2 mol% and 5 mol%) were subjected to 4 heating and cooling cycles to test the reversibility of polymer transition. For all samples the amount of gold nanorods, NIPAM monomer (0.5 M) and photoinitiator D1173 (0.6 wt%) was kept constant and the gels were swollen for 24 h. Every set of measurements was performed between 27 °C and 37 °C within 1 °C steps and every sample was prepared as pentaplicate. Data and fits of heating cycles are shown in red/yellow shades (left), while cooling cycles are depicted in blue/green shades (right). The dotted lines show the first derivative of the actual data at the respective temperature, while the bold lines represent the first derivative of the fit function. (A) Temperature cycles of 1 mol% BIS gels. (B) Temperature response of 2 mol% BIS gels and (C) Temperature response of 5 mol% BIS gels.

Since a clear dependence of the gel response on crosslinker concentration could be shown before, hydrogels prepared with different BIS concentrations were exposed to temperature cycling. The obtained transition temperatures are listed below (**Table 5.4**).It was observed, that apart from the hydrogels containing 1 mol% BIS, several temperature cycles were achieved (**Figure 5.14**) and the obtained transition temperatures (T_T) contributed well to the temperatures obtained without temperature cycling (**Figure 5.13** B). The maxima of the first derivative for samples prepared with 2 and 5 mol% BIS are identical in the range of error, while for samples containing 1 mol% BIS higher variation was observed. Additionally, between heating and cooling cycles, a hysteresis in the received transition temperatures was observed for all tested conditions (**Table 5.4**). Since new hydrogen bonds between water and polymer molecules are formed during polymer transition and the re-organization of those bonds is not necessarily happening in a reversible manner, the conformational change back to the below LCST state is hindered leading to the hysteresis of T_T [181]. However, below a certain temperature, the good solubility of PNIPAM in water gets predominant and the polymer network is dissolved again. This effect, however, can be compensated by increasing the hydrophilicity of the polymer networks, which was experimentally done by increasing the amount of crosslinker. This enhanced hydrophilicity in samples containing higher crosslinker concentrations is also responsible for faster re-swelling kinetics which is evidenced by the fact, that for samples containing 2 and 5 mol% BIS, transition temperatures for all heating and cooling cycles were obtained in the given time of measurements, while this was not observed for 1 mol% BIS gels.

TABLE 5.4 *TRANSITION TEMPERATURE OF PNIPAM COMPOSITE GELS OVER FOUR CYCLES*

		TRANSITION TEMPERATURE T_T [°C]	
		HEATING	COOLING
1 mol% BIS	Cycle 1	29.8	-
	Cycle 2	30.5	-
	Cycle 3	30.8	-
	Cycle 4	30.7	30.7
	Mean[a]	30.5 ± 0.4	30.7
2 mol% BIS	Cycle 1	32.6	29.6
	Cycle 2	32.6	29.5
	Cycle 3	32.8	29.4
	Cycle 4	32.7	29.4
	Mean[a]	32.7 ± 0.1	29.5 ± 0.1
5 mol% BIS	Cycle 1	33.7	31.3
	Cycle 2	34.0	31.1
	Cycle 3	34.2	30.9
	Cycle 4	34.0	30.9
	Mean[a]	34.0 ± 0.2	31.1 ± 0.2

[a]Besides the mean transition temperature over the four different cycles, also the standard deviation is shown

Concluding, the reversibility of PNIPAM volume transition in bulk hydrogels with different crosslinker amounts was shown.

Following the characterization of the surfactant shell and the PNIPAM composite material in bulk, hydrogels were encapsulated in water-in-oil droplets to test the influence of confinement and potential hydrogel/surfactant interactions on PNIPAM transitioning behavior. Although the optimization of the NIPAM concentration and the influence of the amount of crosslinker on the reversibility of polymer transition was already assessed in bulk, the applied confinement may also have an influence on the responses of PNIPAM/gold nanorod composite hydrogels. Therefore, all tested crosslinker and NIPAM concentrations were applied for examining the influence of confinement on the PNIPAM volume transition.

5.1.4 PNIPAM/Gold Nanorods Composite Droplets – A Road Towards Artificial Cell Motility

5.1.4.1 Impact of Temperature -Induced Transition of PNIPAM Inside Droplets

To assess the influence of confinement on the temperature-dependent transition behavior of PNIPAM composite gels, NIPAM polymerization solutions (AuNRs + (0.125, 0.25, 0.5 or 1.0) M NIPAM + (1, 2 or 5) mol% BIS + 0.6 wt% D1173) were encapsulated within the droplets and polymerized. For droplet formation via the shaking method [180], either 2.5 mM PNIPAM surfactant or commercial fluorosurfactant (1.4 wt% and 5 wt%) was used. As can be seen in **Figures 5.15** and **5.16**, droplets with an inhomogeneous size were obtained. It is important to mention here, that NIPAM-containing monodisperse droplets can be achieved using droplet-based microfluidics (see **Appendix Figure SI 9**). However, in contrast to the shaking method, a higher surfactant concentration of 5 wt% might be required for stable droplet production by droplet-based microfluidics due to a higher surface-to-volume ratio caused by a smaller droplet size and the correspondingly higher surfactant consumption.

Following droplet assembly and polymerization of NIPAM within the droplets, an optical analysis of the response of the PNIPAM hydrogel-containing droplets was performed using confocal microscopy (**Figures 5.15** and **5.16**). Temperature changes were applied using a stage-top incubator. The highest temperature was chosen to be 60 °C. Note, this relatively high temperature was selected due to a poor temperature-insulation of the used incubation chamber (completely open bottom) in order to reach temperatures above T_T of PNIPAM.

Although different NIPAM concentrations did not show a significant influence on PNIPAM volume transition behavior in bulk, the influence of the NIPAM concentration between 0.125 – 1 M in the confinement of water-in-oil droplets was analyzed (**Figure 5.15**). In the concentration range between 0.125 – 0.5 M, besides an increased droplet diameter (mean), no remarkable changes in the droplet dimensions prior and after polymerization were observed at 25 °C. Note, slightly bigger droplets were observed in the case of droplets containing higher NIPAM concentrations. This can be attributed to a higher viscosity of the aqueous phase. However, in the case of 1 M NIPAM, the polymerization

led to the deformation of the droplets due to the expansion of the encapsulated volume. To select the optimal concentration of NIPAM, the encapsulated gels were exposed to a temperature gradient. As can be observed in **Figure 5.15**, at NIPAM concentrations below 0.5 M, the increase of temperature resulted in the formation of non-connected polymer grains. This observation is attributed to the insufficient polymer loading within the droplets. Therefore, no morphological changes of droplets were observed. In contrast to lower concentrations, in the case of 0.5 M NIPAM, a contraction of the interconnected polymer network was observed. This contraction led to the morphological deformation of the observed droplets. However, an additional increase of the NIPAM concentration (1 M) resulted in the production of overloaded PNIPAM droplets that even at 25 °C showed non-spherical shapes. Therefore, a NIPAM concentration of 0.5 M was chosen for the next experiments.

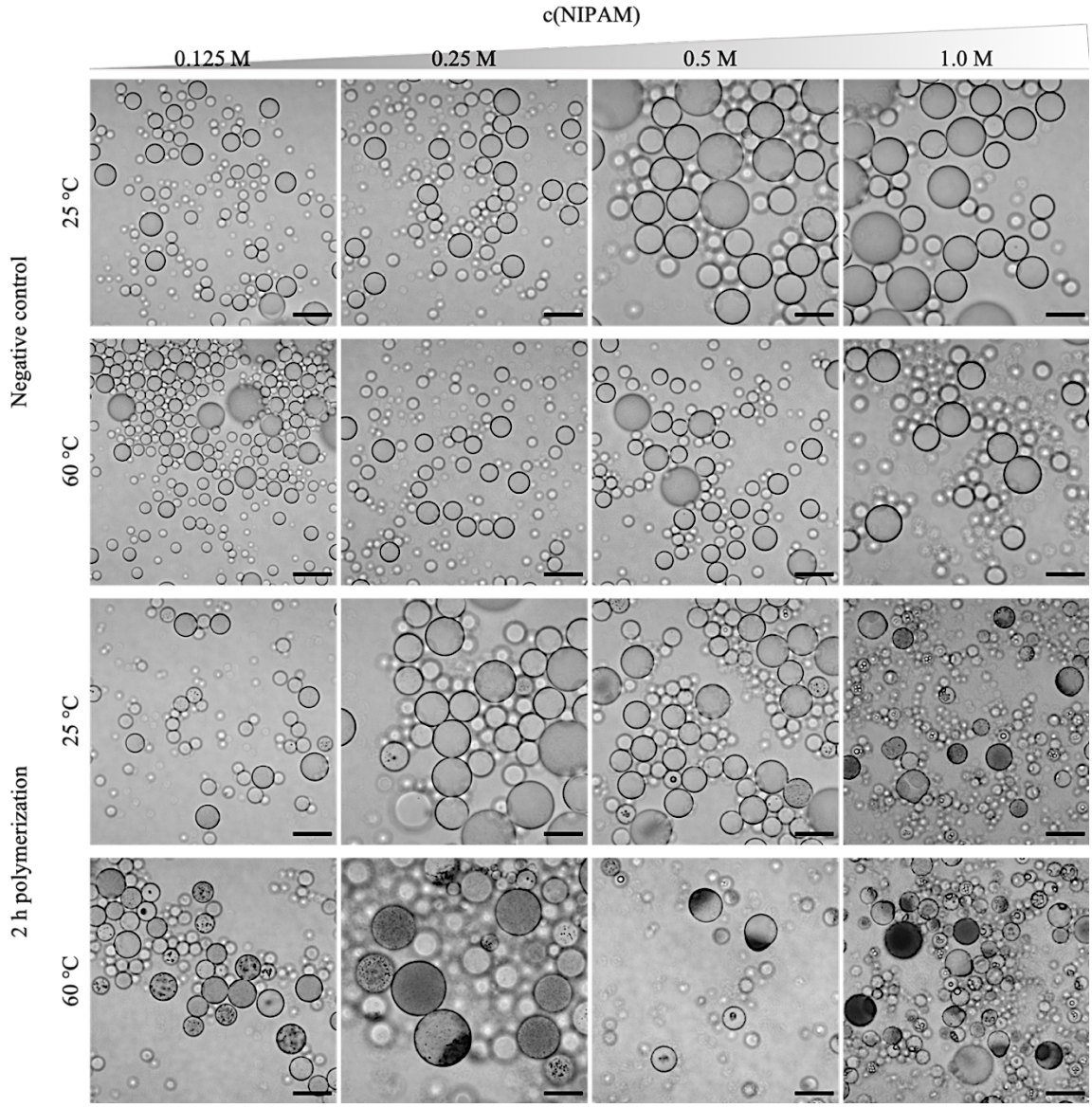

Figure 5.15 *Influence of NIPAM Concentration on PNIPAM Transitioning Behavior in Droplet Confinement*

Droplets were prepared in duplicates with gold nanorods, 5 mol% BIS, (0.125 – 1.0) M NIPAM and 0.6 wt% D1173 as aqueous phase and 1.4 wt% commercial fluorosurfactant as oil phase. After assembly, half of the droplet samples were polymerized for 2 h (365 nm, 15 cm working distance) while the other half of the samples were kept untreated. It was shown, that a monomer concentration of 0.5 M NIPAM is the optimal concentration for the PNIPAM assembly inside the droplets. Scale bar: 50 µm.

Following the optimization of the NIPAM concentration (0.5 M) required for the efficient thermo-responsive contraction of the PNIPAM-based artificial cytoskeleton, the impact of PNIPAM crosslinking on its contractility was tested. The droplets depicted in **Figure 5.16** were prepared with 1.4 wt% commercial fluorosurfactant and are shown at 25 °C (left pictures) and 60 °C (right pictures), respectively. As can be seen in **Figure 5.16** A and B, part of the droplets appeared to be less transparent or containing grain-like polymer structures. In general, successful polymerization within the droplets is not easily

detectable since PNIPAM-formation is causing only in estimated 20% of the droplets a change of morphology (**Figure 5.15** and **Figure 5.16** A). An exception are droplets prepared with NIPAM concentrations higher than 0.5 M (**Figure 5.15**). In those droplets, many deformed and completely filled droplets are visible. Comparing the droplets obtained with PNIPAM/gold nanorods composite gels prepared with different BIS concentration, no difference is detectable between the different samples at 25 °C (**Figure 5.16** A). However, comparing the time-lapse pictures obtained during temperature cycling (**Figure 5.16** B and C) it can be observed that the composite hydrogels containing 1 mol% BIS show the smallest volume transition leading to a final polymer volume in the range of 30 - 40% of the droplet volume, which was determined optically. Despite the smallest volume transition, the deformation of the droplets was observed. This deformation is attributed to the water release process. PNIPAM releases water during volume transition leading to areas with a denser polymer gel network structure and some with more fiber-like structures. The formed network structure is then, upon heating, collapsing to a denser polymer globule leading to the deformation of a part of the droplet while the areas with the fiber structures are also collapsing but not contributing to the deformation due to single fiber collapse instead of a network collapse. However, due to a low crosslinker concentration, a more fibrous gel structure in contrast to a mesh structure is formed, which can explain the low contractility of the encapsulated gel. Interestingly, at some point, no further collapse of the polymer gel is observable and the deformed stated of the droplets is preserved, independent of the fact that the temperature was kept constant above T_T (**Figure 5.16** C). This observation is contributing to the hypothesis of different polymer architectures within the droplets and the fact that due to low crosslinking degrees and correspondingly bigger distances between the interconnected PNIPAM chains, the contraction is stagnating, since no strong hydrophobic interactions can be formed. In contrast, the droplets containing 2 and 5 mol% BIS are showing two phases of volume transition (**Figure 5.16**, C). The first phase of volume transition is characterized by the fast ($\Delta t \approx 30$ s) collapse of the polymer network leading to a polymer volume of roughly 40 – 45% of the overall droplet volume. During this fast volume transition, similar to the behavior seen for 1 mol% BIS samples, deformation of the droplets is observed. However, during the second slow phase of volume transition ($\Delta t \approx 150$ s), an additional collapse of the composite polymer network leading to 10 – 15% of final polymer fraction of the droplet volume is observed. During this process, the droplet recovers its spherical shape with a small polymer-containing globule at the

periphery of the droplet. Again, this is in accordance with the theory of different polymer structures, where the first phase of volume transition that is also observable for the 1 mol% BIS condition is assigned to the release of water in combination with a first collapsing of the polymer structure. The second slow phase is dominated by the further shrinking of the densely crosslinked polymer areas due to hydrophobic interactions and the rearrangement of hydrogen bonds. Since the amount of crosslinker was increased in comparison to the 1 mol% BIS sample, this second phase of transition is enabled due to the formation of larger areas of crosslinked mesh structures instead of fiber-like structures.

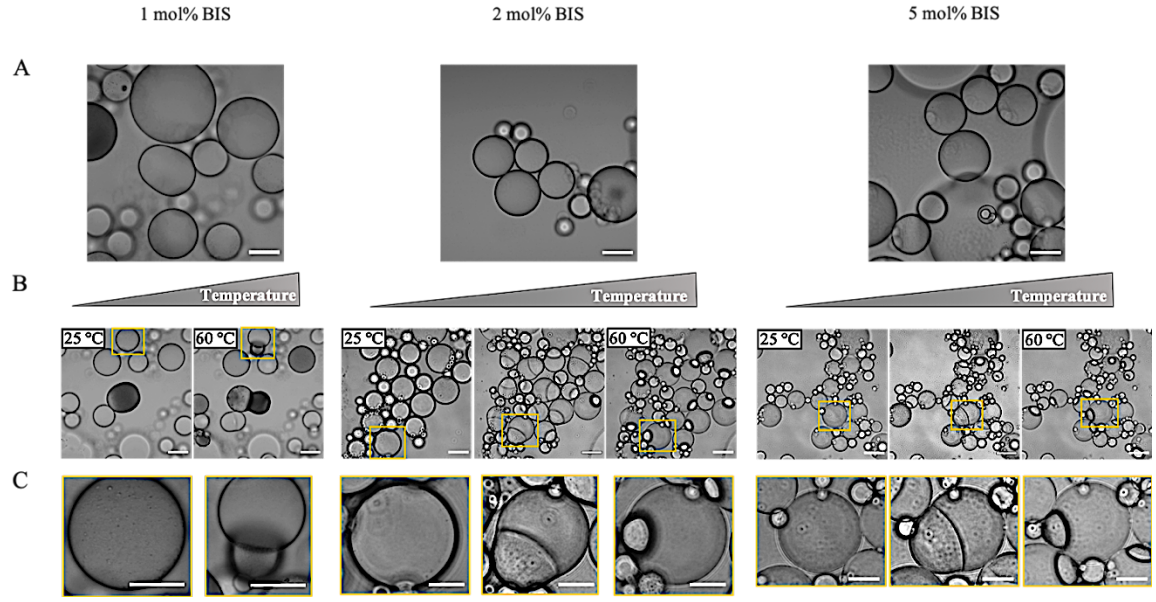

Figure 5.16 *Representative Brightfield Images of temperature-Induced Change of Droplet Area* Droplets were prepared as described in Section 4.5.1.1. After assembly, droplets were polymerized for 2 hours (365 nm, 15 cm working distance). (A) Representative confocal images of droplet appearance at 25 °C. Scale bar: 50 µm (B) Change of droplet area upon temperature-induced polymer transition. Droplets were heated between 25 °C (left) and 60 °C (right). For 2 and 5 mol% BIS also an intermediate state (middle) is shown The collapsed polymer hydrogel forms a dense globular structure at the periphery of the droplet. Yellow boxes track one droplet during PNIPAM volume transition. Scale bar 50 µm. (C) Magnification of insets highlighted in (B) during volume transition of PNIPAM/gold nanorod composite gels. Scale bar: 25 µm

The occurring phase separation, which is arising during polymer collapse, is also observable in SEM micrographs (**Figure 5.17**). For the acquisition of micrographs, droplets were first heated to 60 °C using a water bath and afterwards flash frozen in liquid nitrogen and freeze-fractured. The heating of samples prior to freezing induces the transition to the collapsed state of the droplet-entrapped polymer gel, which is visible as dense structure in the micrographs (**Figure 5.17**). Note that this observation is independent of the used surfactant. Unfortunately, due to the dense polymer network, no gold nanorods were

observed. However, in samples without the polymer, the nanorods are clearly visible as bright structures within the droplets (see **Appendix Figure SI 11**). Besides spherical droplets, also some asymmetric droplets are present in some samples, mostly in the sample prepared with commercial fluorosurfactant (**Figure 5.17** A). Apart from the dense polymer network (area in the micrographs marked by I), also more fibrous and less dense structures (area in the micrographs marked by II) are visible within the droplets. This observation supports the hypothesis of different polymeric structures in the droplets that is, in combination with the water release during polymer volume transition, responsible for the differences in droplets temperature response for samples prepared with different crosslinker amounts (**Figure 5.16**). However, also in samples prepared with the same polymer composition, the morphology of the polymer network within different droplets is not homogenous over the observed population. Since microfluidic encapsulation was used for the production of PNIPAM/gold nanorods composite gel filled droplets that were analyzed via SEM measurements, inhomogeneity of the encapsulated content in terms of overall concentrations is not a reasonable explanation for the differences in hydrogel appearance in the droplets. One possible explanation is the small volume in the droplets, which leads to the formation of gels with small molecular masses. With such small masses, even minor local differences in the distribution of the starting materials lead to a significant change in polymer behavior, since the presence or absence of another monomer unit has a strong influence on the molecular weight. Also locally arising concentration differences of the encapsulated content or differences in UV light amount during polymerization caused by a dense packing of the droplets can explain the different droplet morphology. In order to avoid both, differences in local content distribution in the droplets and different irradiation intensities with UV light, mixing of the droplets during the polymerization might be beneficial. However, mixing must be carried out in such a way that the rupture of the droplets is avoided.

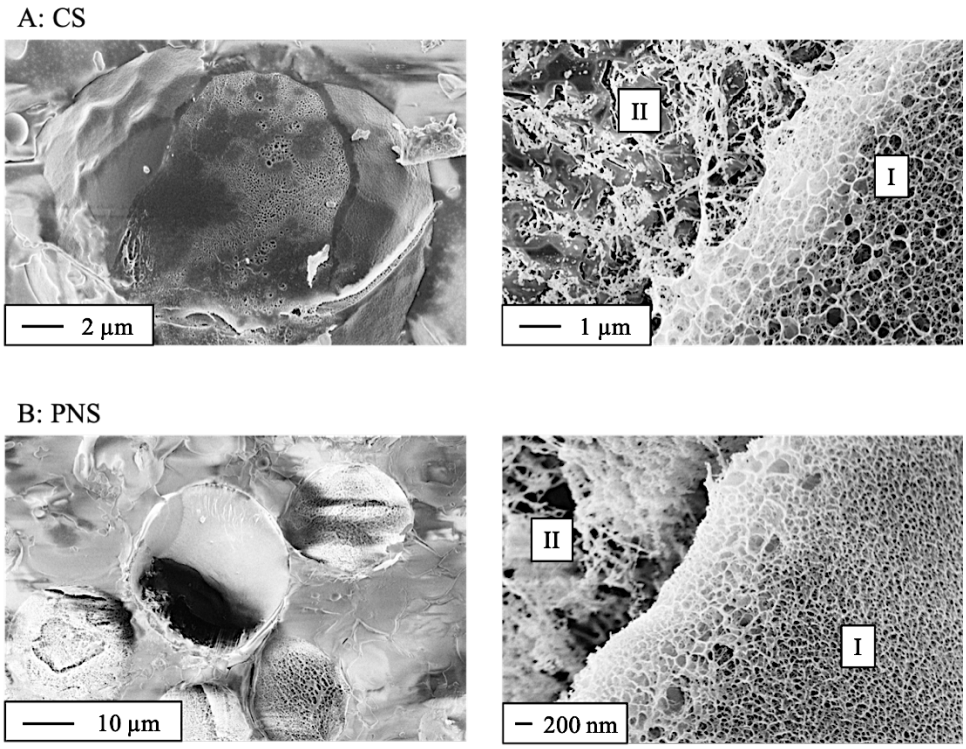

FIGURE 5.17 *REPRESENTATIVE CRYO SEM MICROGRAPHS OF COMPOSITE GEL FILLED DROPLETS*
Droplets were prepared as described in Section 4.5.1.2. As crosslinker concentration, 5 mol% was used. Before freeze-fracturing, droplets were heated to 60 °C using a water bath. SEM micrographs on the left side are showing the overview of one droplet, while in the micrographs on the right side a close-up of the hydrogel structure in the droplets is depicted. Independent of the used surfactant, two different polymer regimes are visible, one dense crosslinked mesh structure (I) and an area with more fibrous structures (II). The respective scale bars are shown in the micrographs. (A) Droplets prepared with commercial fluorosurfactant. (B) Droplets obtained with the PNIPAM-based surfactant.

In order to investigate the temperature-induced change of the droplets more precisely and to classify the influence of not only the hydrogel material but also the used surfactants, a statistical analysis of the change in droplet area was carried out. For this purpose droplets were produced with three different crosslinker concentrations (1, 2 and 5 mol% BIS) and 0.5 M NIPAM as described before. Besides the commercial fluorosurfactant the self-synthesized PNS was used as surfactant (**Figure 5.18**).

In order to ensure a better comparability between the individual samples, droplets were produced using microfluidic devices, thus providing droplets with an approximately equal size. Although microfluidic encapsulation of content is ensuring an equal size and content distribution within the droplets, no difference in droplet temperature response was detectable for droplets prepared via the shaking method compared to droplets prepared via microfluidic chips (see **Appendix Figure SI 10**, **Table 5.5**). Accordingly, trends and observations made under these highly controlled conditions can also be applied to the droplets prepared by shaking.

The combination of the hydrogel system with water-in-oil droplets leads to a crosslinker- and surfactant-dependent change of the projected droplet area during heating cycles (**Figure 5.18**). It was observed that higher crosslinking degrees and higher IFT values of the used surfactant cause a decrease in droplet area, while lower crosslinking degrees and IFT values are favoring droplet deformation (**Table 5.5**). Higher IFT values are hereby represented by the PNIPAM-containing surfactant (~ 27 mN/m), while the commercial fluorosurfactant with a low IFT value is forming more easily deformable droplets (**Table 5.5**). This trend is visualized by higher differences between the "below LCST"- and the "above LCST"-state. The only exception are the droplets produced with 2 mol% BIS and PNS, which represent a clear deviation from the observed trend, since the increase of projected droplet area during heating cycles is explicitly higher than the values determined for 1 mol% BIS samples (**Table 5.5**), which is not seen in CS samples. This is caused by the increased fusion of the droplets during the temperature cycling. Although droplets with a collapsing polymer network could be generated with all tested crosslinker concentrations, droplets with 5 mol% BIS concentration showed a higher amount of polymer network filled droplets. For droplets with lower crosslinking degrees, more droplets that contain grain-like polymer structures upon heating instead of a collapsed polymer globule were observed. Therefore, 0.5 M NIPAM and 5 mol% BIS seem to be the optimal conditions for reproducible production of PNIPAM/gold nanorod composite gel filled droplets. However, the highest change in droplet area was observed using CS in combination with hydrogels containing 1 mol% BIS. This trends are in accordance with the results already obtained by the optical analysis of the droplet behavior upon temperature cycling (**Figure 5.16**).

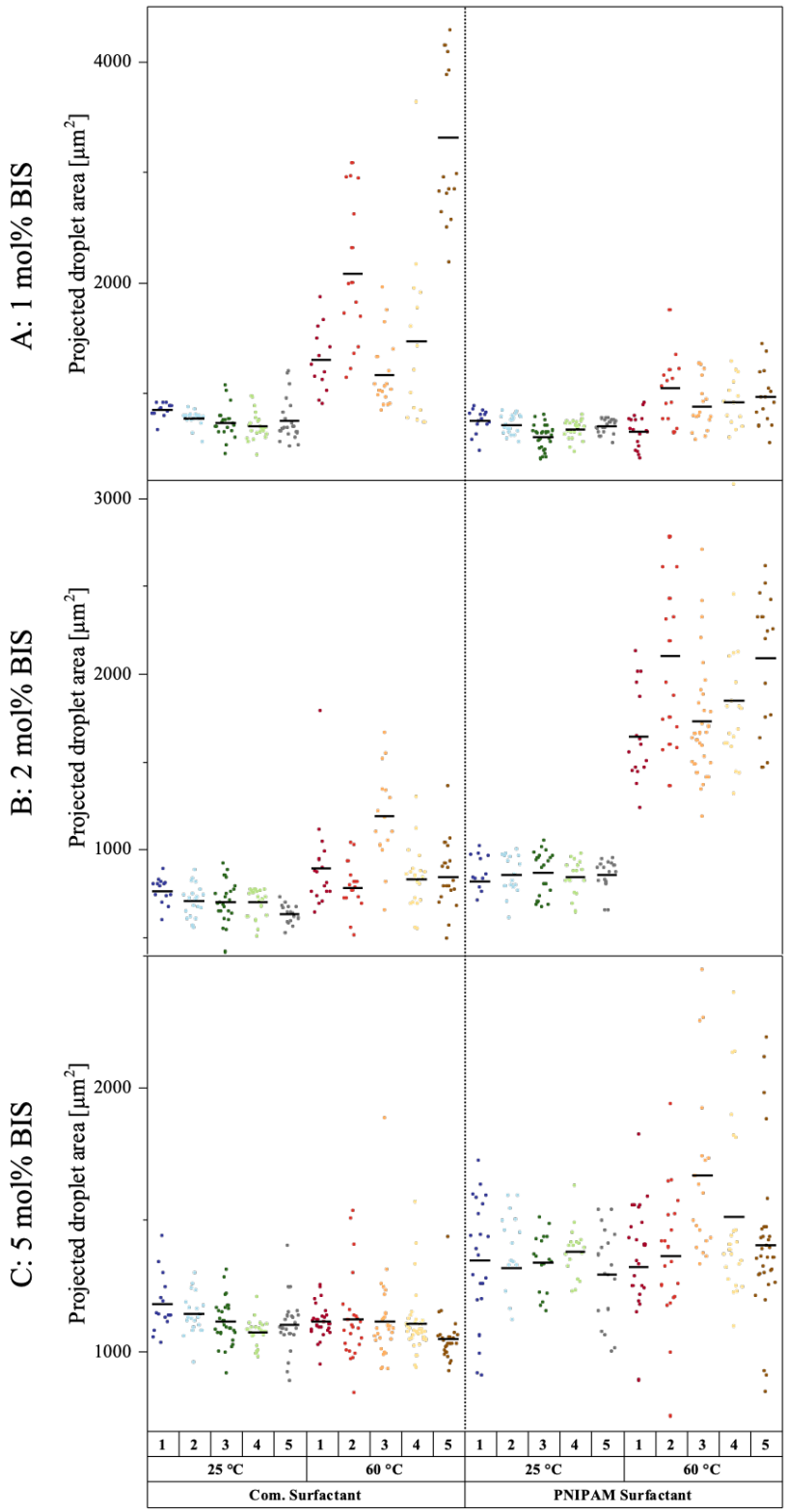

FIGURE 5.18 *INFLUENCE OF DROPLET CONFINEMENT ON PNIPAM TRANSITIONING BEHAVIOR*
Droplets were prepared as described in Section 4.5.1.2 and the droplet areas during five heating and cooling cycles were determined. Data collected for the commercial fluorosurfactant is represented on the left side of the respective graph, data for PNS on the right side, respectively. The area of the droplets at 25 °C is shown in blue/green shades, while the values at 60 °C are depicted in red/yellow shades. The data acquired for (A) 1 mol% BIS, (B) 2 mol% BIS and (C) 5 mol% BIS is shown. The statistical analysis of the projected droplet area during temperature cycling reveals the reversibility of PNIPAM volume transition within the droplet confinement and the dependency of this process on the polymer and surfactant composition.

TABLE 5.5 *STATISTICAL EVALUATION OF TEMPERATURE-INDUCED DROPLET AREA CHANGE*

		PROJECTED DROPLET AREA [µM²]				
		25 °C		60 °C		
	BIS CONC.	MEAN	STDEV	MEAN	STDEV	DIF. [%][a]
CS	1 mol%	751.3	83.5	1861.7	685.2	247.8
	2 mol%	697.3	62.1	904.7	174.6	129.8
	5 mol%	1120.0	60.1	1099.4	74.5	98.2
Shaking[b]	5 mol%	4895.1	601.6	4845.8	600.4	98.9
PNS	1 mol%	677.2	69.3	885.8	177.3	130.8
	2 mol%	847.3	72.0	1878.6	281.3	221.7
	5 mol%	1333.2	107.9	1452.0	212.3	108.9

[a]Calculation of difference in droplet area: $Diff.[\%] = \frac{A_{above\ LCST,60\ °C}}{A_{below\ LCST,25\ °C}} * 100\%$

[b]Droplets produced via the shaking method are prepared with 5 mol% BIS as crosslinking reagent and 1.4 wt% commercial fluorosurfactant.

Since not only several different hydrogel and surfactant combinations were analyzed, but also various temperature cycles were applied, a closer look on the behavior of the droplets during those cycles is outlined in the following. First of all, it is noticeable that the variance of the data at 60 °C is much higher than the variance at 25 °C. Due to the production of the droplets using microfluidic chips, the small variance of the data at 25 °C at least for the first cycle is following expectations, since microfluidic chips are used for the production of monodisperse droplets. Interestingly, the variance of the data at 25 °C does not fluctuate greatly over the several cycles (e.g. Commercial surfactant, 5 mol% BIS, mean droplet area: 1177.092 µm^2 (cycle 1), 1140.564 µm^2 (cycle 2), 1111.474 µm^2 (cycle 3), 1071.328 µm^2 (cycle 4) and 1099.533 µm^2 (cycle 5)), which indicates that although the polymer volume transition is leading to the deformation of the droplets upon heating, the original shape and droplet area is restored during the cooling cycles. This shows that over several cycles, the phase transition of the polymer and the resulting deformation of the droplets is reversible, which qualifies the presented system as a dynamic cytoskeletal model. The high variance of the data at 60 °C allows the assumption that although monodisperse droplets were produced, the polymer network formed in the droplets differs within the investigated samples, which leads to an individual degree of deformation for every analyzed droplet. This inhomogeneity within one droplet population was already observed during cryo SEM measurements (see **Figure 5.17**).

Although IFT measurements (see **Figure 5.8** and **Table 5.2**) suggesting that PNS might enhance the connection between the droplet-filling polymer network and the surfactant layer of the droplets, no clear evidence for a higher degree of interaction between surfactant-coupled PNIPAM and PNIPAM is revealed in the statistical analysis of the droplet area. The high IFT values of the synthesized PNS compared to CS are resulting in a minor change of the projected droplet area. To evaluate the contact area between the PNIPAM/gold nanorods composite gel and the surfactant membrane in a better way, droplets prepared with either PNS or CS were optically analyzed using confocal microscopy (**Figure 5.19**). Following droplets formation, the droplets were heated above T_T and the contact area between the surfactant interface and the collapsed composite material was determined. The results revealed a higher contact area between the collapsed PNIPAM-based hydrogel and PNS which is leading to the deformation of the droplets to an ellipsoid-like shape. In contrast, in the case of CS-stabilized droplets, the droplets preserve a spherical shape following the PNIPAM collapse.

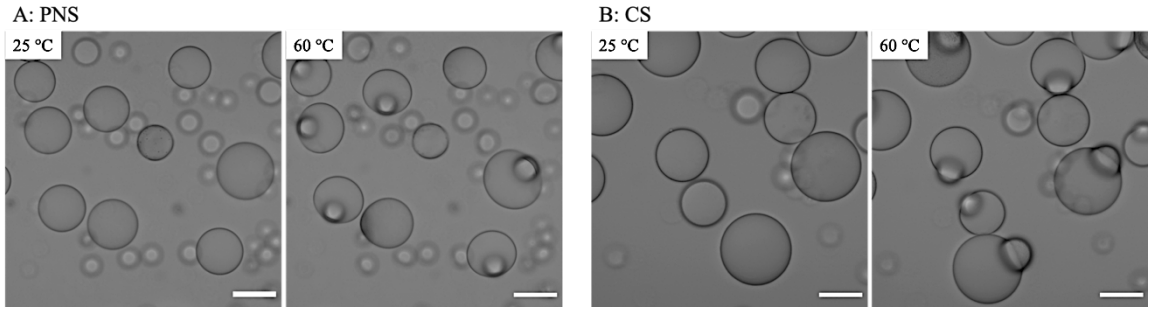

Figure 5.19 *Analysis of Contact Area between collapsed PNIPAM Gel and the Surfactant Interface*

Droplets were prepared with an aqueous phase containing Gold nanorods (9.5×10^5 particles/ml), 0.5 M NIPAM, 1 mol% BIS and 0.6 wt% D1173 and an oil phase containing either 2.5 mM PNS or 1.4 wt% CS via shaking. After production, the droplets were polymerized for 2 h. (A) Representative images of droplets prepared with PNS at 25 and 60 °C. Scale bar: 50 µm. (B) Representative images of droplets prepared with CS at 25 and 60 °C. Scale bar: 50 µm.

In summary, I could demonstrated, that the artificial PNIPAM-based cytoskeleton is leading to the deformation of water-in-oil droplets. Additionally, the reversibility of this deformation process over several cycles was shown, mimicking the dynamic rearrangement of the cytoskeleton which is also observed for the natural analogue actin.

After optimizing the PNIPAM-based composite gel conditions in bulk and droplet confinement and analysis of the obtained droplets upon temperature cycling, the motility of droplets induced by changes in the artificial cytoskeleton was reconstituted. To

accomplish cellular-like motility, PNIPAM-containing droplets shall experience significant morphological deformation. Nevertheless, despite the deformation, initially spherical PNIPAM-containing droplets did not show any motility. Therefore, inspired by the symmetry breaking of migrating mammalian cells, the concept of polarization was successfully transferred to droplets to implement cell-like motility.

5.1.4.2 Influence of Symmetry Breaking on Droplet Behavior

To modulate droplet symmetry, two different ways were tested: First, the pre-orientation of droplets using microfluidic chips with small channels and second, an intrinsic route by generating already symmetry-broken droplets.

5.1.4.2.1 Pre-Orientation in Microfluidic Channels

For the generation of asymmetric droplets, controlled deformation using microfluidic devices was chosen. Towards this end, a device for production and observation of PNIPAM-filled gel droplets was designed. In order to induce symmetry breaking and to be able to simultaneously observe the pre-oriented droplets during temperature changes, a device with an observation chamber consisting of 500 small interconnected chambers was designed (**Figure 5.20** A). In addition, a big polymerization chamber was introduced in the device.

For droplet production, a gel composition consisting of gold nanorods, 0.5 M NIPAM, 5 mol% BIS and 0.6 wt% D1173 was chosen. As surfactant, 5 wt% commercial fluorosurfactant was used. Although this particular combination showed the lowest percentage in projected droplet area change during temperature cycling (**Table 5.5**), the chosen crosslinker concentration ensures the highest amount of a completely crosslinked gel inside the droplets and with that a collapsing polymer network as a whole. The chosen NIPAM concentration is optimal for applications in droplet confinement without having overloaded droplets. CS as surfactant was selected because of its low IFT value to allow deformability of the produced droplets.

First, the droplets were produced using the production module (I) which is connected with a polymerization chamber (II). Ones the desired amount of droplets was transferred into the polymerization chamber, the droplet production was stopped and the device sealed for NIPAM polymerization. After polymerization, the droplets were transferred into the interconnected observation chambers (III). However, the

polymerization was not possible due to the high UV absorption of both the used fluorinated oil and the PDMS device and therefore no polymerization of the gel inside the droplets could be achieved. Thereupon, only the observation chamber (III) was used and the droplets were introduced after production and polymerization (**Figure 5.20** B).

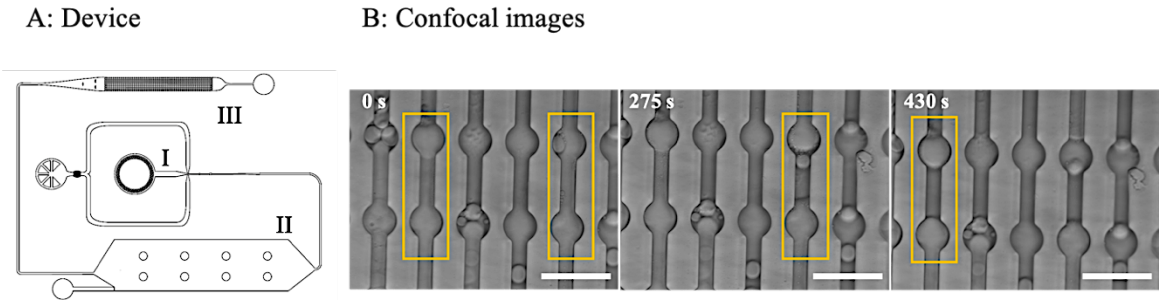

FIGURE 5.20 *GENERATION OF SYMMETRY BROKEN DROPLETS USING A COMBINED PRODUCTION AND OBSERVATION DEVICE*
(A) This microfluidic PDMS chip was fixed onto a cleaned glass coverslip. The device is composed of a unit for the production of droplets (I), a polymerization chamber (II) and an observation chamber (III). The big observation chamber consists of 500 small chambers. The small round observation chambers (30 µm diameter) are connected by narrow channels with a width of 20 µm and a length of 50 µm. (B) Representative confocal images of droplets inside the observation chamber upon heating. Droplets were prepared with gold nanorods and 5 wt% commercial surfactant as described in Section 4.5.1.2 and afterwards introduced inside the observation chambers. Yellow boxes are showing division of the droplets within the device upon heating. The time of heating is indicated in the left corner of the respective image. Scale bar: 100 µm.

After the transfer of the droplets inside the chamber, the whole device was sealed and heated using an incubation chamber. During temperature increase, some of the droplets divided upon polymer transition induced collapse (**Figure 5.20** B (yellow boxes)). The division of artificial cells is highly desirable and the implementation of division in synthetic cells is a very active field of research [176]. The droplets showing this particular behavior are those overarching several channel-connected chambers. Those droplets were formed during transfer into the observation chambers due to enhanced fusion. Although just low pressures were used for the droplet transfer (10-20 mbar), fusion events could not be prevented. This fusion is caused by the elevated pressure that is applied on the droplets due to channel constriction. However, due to the size of the observation chamber and the entire device, it cannot be excluded that the division of droplets was caused by pressure differences in the chamber. In order to eliminate possible pressure differences from the system and further to minimize the pressure on the droplets when they are introduced into the chambers, a device only consisting of an observation chamber was used and the influence of the pre-orientation was tested (**Figure 5.21** A).

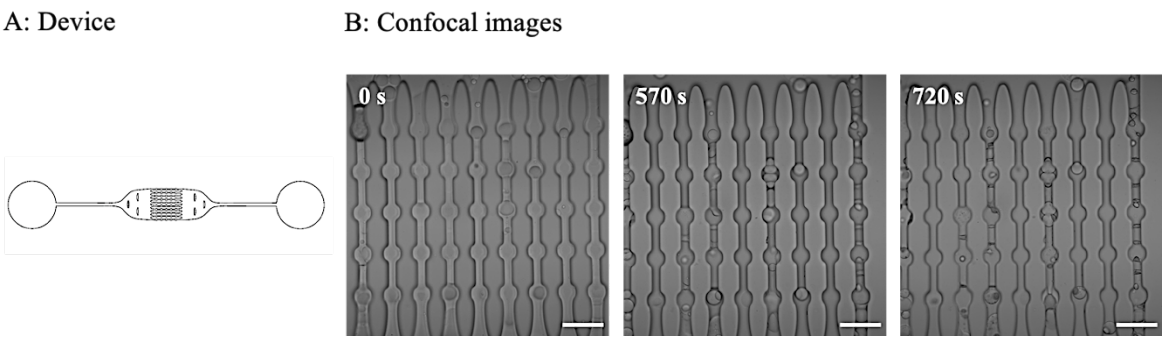

FIGURE 5.21 *EXCLUSION OF THE INFLUENCE OF PRESSURE DIFFERENCES ON DROPLET DIVISION INSIDE MICROFLUIDIC CHIPS*
(A) This microfluidic PDMS chip was fixed onto a cleaned glass coverslip. The big observation chamber consists of 50 small chambers. The small round observation chambers (30 µm diameter) are connected by narrow channels with a width of 20 µm and a length of 50 µm. (B) Representative confocal images of droplets inside the observation chamber upon heating. Droplets were prepared with gold nanorods and 5 wt% commercial surfactant as described in Section 4.5.1.2 and afterwards introduced inside the observation chambers. Upon heating, no division of droplets inside the device was observable. The time of heating is indicated in the left corner of the respective image. Scale bar: 100 µm

By using the refined device, the fusion of the droplets during transfer could be significantly reduced. This led to a higher amount of also small droplets (diameter ~ 30 µm) inside the channels and chambers. When the behavior of the droplets inside the new device was analyzed, no division of droplets could be observed although some droplets are still bridging several chambers (**Figure 5.21** B). This means that the force generated by the polymer during the phase transition is not sufficient for the division of the droplets in the device alone. Only the combination of a pressure gradient within the device and the polymer volume transition is leading to droplet division.

Although a controlled manipulation of droplets in terms of symmetry breaking was possible using microfluidic devices, the constriction-based pre-orientation alone is not sufficient for a controlled droplet division. Additionally, also no migratory motility could be achieved within the channels. Therefore, the influence of intrinsic symmetry breaking by enhanced droplet fusion was investigated.

5.1.4.2.2 PNIPAM-MEDIATED MOTILITY IN ASYMMETRIC DROPLETS

Since the controlled migration of device-trapped PNIPAM composite gel droplets could not be achieved, non-spherical droplets with the intrinsic feature of symmetry breakage through polymer distribution were generated using targeted fusion. For this purpose, stable (1.4 wt% CS) and unstable droplets (0.7 wt% CS) were generated and mixed prior to the polymerization procedure. Due to the low surfactant amounts needed for

preparation of the asymmetric droplets, the production via microfluidic chips was not possible, since the generated droplets were unstable. Therefore, the droplets were produced via shaking as described in **Section 4.5.1.1**.

Compared to droplets prepared normally with 1.4 wt% CS (**Figure 5.22** B), the samples containing mixed droplets (**Figure 5.22** C) showed a higher amount of asymmetric droplets (**Figure 5.22** A), namely (13.2 ± 2.1)% in comparison to (0.8 ± 0.6)%, respectively. This means that an increased number of asymmetric droplets were obtained due to different surfactant concentrations in the mixed populations and an associated instability of the droplets. Importantly, the asymmetric droplets remained stable over several month. The combination of droplets with even lower surfactant concentration (0.5 wt% CS) with stable droplets (1.4 wt% CS) did not lead to a larger amount of asymmetric droplets, but mainly to the bursting of the droplets during polymerization. This means that a certain threshold of surfactant is needed also for the generation of unstable droplets. Nevertheless, the method is suitable for the increased production of asymmetrical droplets to induce cell motility and was therefore used for subsequent experiments.

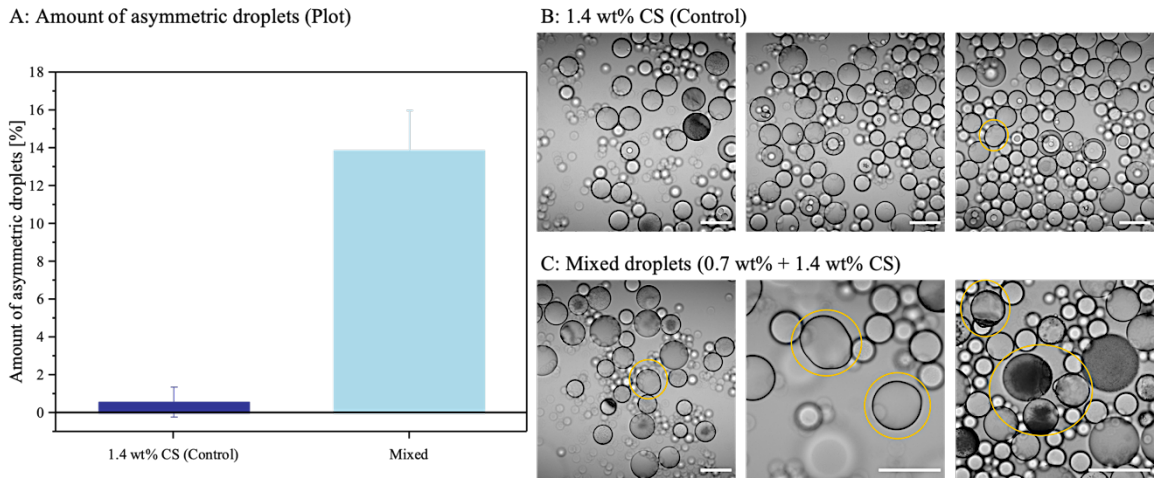

FIGURE 5.22 *INVESTIGATION OF TARGETED FUSION ON DROPLET APPEARANCE*
Droplets were produced with 1 mol% BIS and either 1.4 wt% CS or 0.7 wt% CS as surfactant as described in Section 4.5.1.1. For the preparation of mixed droplets, 1.4 wt% CS droplets were added on top of 0.7 wt% CS droplets and the emulsion afterwards gently mixed using a pipette prior to polymerization. Each sample was prepared in triplicates. (A) Graphical representation of difference in asymmetric droplet amount. The percentage of asymmetric droplets was calculated by optically analyzing 60 droplets per replicate concerning the circularity. The amount of asymmetric droplets in the control sample is shown in dark blue, the percentage in the mixed droplet sample in light blue. (B) Representative confocal image of droplets in the control sample. Yellow circles mark asymmetric droplets. Scale bar: 100 µm. (C) Representative confocal images of enhanced amount of fused droplets in mixed droplets sample. Yellow circles mark asymmetric droplets. Scale bar: 100 µm.

Following the assembly of non-spherical droplets, the temperature-induced PNIPAM-mediated motility was investigated. To achieve significant deformation during temperature cycling that might be required for PNIPAM-induced droplet motility, CS and 1 mol% BIS were used for droplets preparation. Depending on the heating speed, the droplets show either division-like behavior (**Figure 5.23**) or tend to be motile (**Figure 5.24**).

Upon fast heating (0.3 °C/s), the collapse of the polymer structure and the efflux of water from the hydrogel was triggered in a rapid way leading to a strong deformation of the droplet and a semi-division. For this deformation some kind of interaction between the polymer gel inside and the surfactant layer is needed. Although the exact structure of the commercial surfactant is not clear, MALDI-TOF MS measurements revealed that the hydrophilic part of the surfactant is comprised of PEG molecules [161]. Those PEG molecules can undergo reactions when oxidative stress is applied [178] because of radical cleavage after a so-called random chain scission process [179], which lead to enhanced interactions between the encapsulated PNIPAM and the surfactant layer.

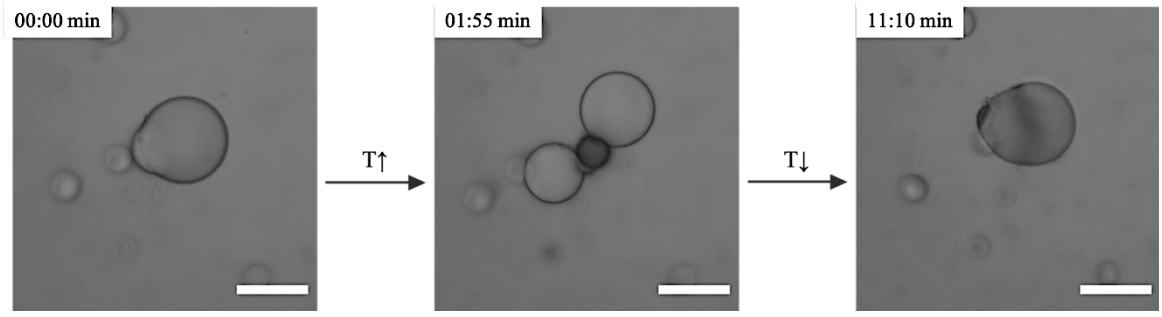

FIGURE 5.23 *TEMPERATURE-INDUCED DEMIXING OF ASYMMETRIC DROPLETS*
Symmetry broken droplets were produced via shaking method by mixing droplets produced with 1.4 wt% commercial fluorosurfactant (stable) with droplets produced with 0.7 wt% (unstable) before polymerization. As aqueous phase, gold nanorods in combination with 0.5 M NIPAM, 1 mol% BIS and 0.6 wt% D1173 was used. The droplets were afterwards subjected to temperature changes (25 °C → 60 °C and vice versa) leading to the collapse of the polymer hydrogel and the incomplete division of the droplets. Scale bar 100 µm.

Although a strong deformation of the droplet was observed during the volume transition of the polymer, no complete division was detected. Nevertheless, the division-like behavior of the droplets is observable over several temperature cycles before the connection between polymer hydrogel and surfactant might rupture and no division behavior can be detected anymore. This observation is due to high shear stresses that are exerted on the polymer/surfactant connection during the polymer transition.

When the asymmetric droplets were heated and cooled at slow rates, namely around 0.06 °C/s, a different behavior was observable. **Figure 5.24** shows the dynamic PNIPAM-mediated motility of droplets due to heating and cooling cycles. It was observed that upon heating, the PNIPAM volume transition led to a decrease of droplet deformation. This can be attributed to the collapse of two independent polymer networks, leading to small PNIPAM volume fractions within the droplet (see **Figure 5.24**, **I**). A sequential cooling step led to the rehydration of the polymer networks and rescue of the droplet form due to the shape memory of the encapsulated PNIPAM networks. During these heating and cooling cycles, a slight motility of the droplets was observed. However, the total dislocation of the droplets from the beginning until the end of the temperature cycling is not remarkable (**Figure 5.24**).

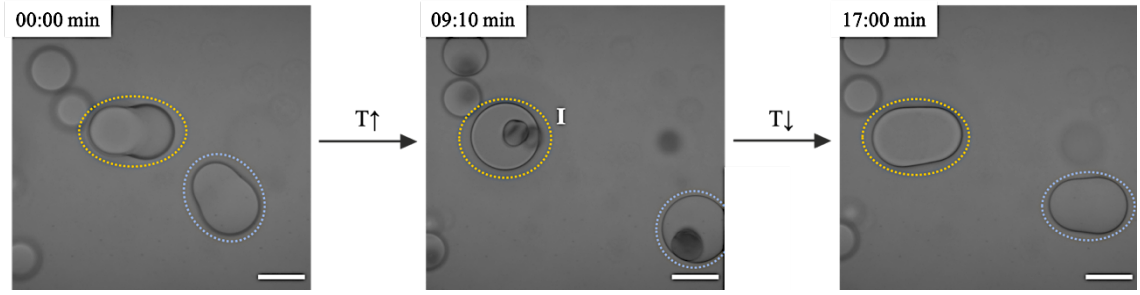

Figure 5.24 *Induction of Motion by Smart artificial cytoskeleton*
Asymmetric droplets were prepared as described in Section 4.5.1.1 with gold nanorods, 0.5 M NIPAM, 1 mol% BIS and 0.6 wt% D1173 as aqueous phase. The droplets were afterwards subjected to temperature cycles with a slow heating speed (0.6 °C/s), contrary to the previously performed experiments with a heating speed of 0.3 °C/s. The induced collapse of the polymer hydrogel led to the migration of the droplets. The region of the collapsed polymer within one droplet is marked with (I). In sake of clarity, the respective migrating droplets are marked by colored ellipsoids. Scale bar 100 µm.

It is important to mention here, that significant migration of the asymmetric droplets was observed in rare cases (see **Appendix Figure SI 13**). This type of heterogeneity in droplets motility behavior can be attributed to chemical or physical defects that are presented on the surface of the coverslips functioning as anchor points for interactions between the glass surface and the droplets. Note, due to the Buoyancy force the droplets are pushed towards the upper glass slide [182]. Therefore, the chemical nature of the glass and its homogeneity might affect the friction that is created between the droplets and the surface which is leading to droplet motility.

To optimized the homogeneity of the glass surface and to enhance the friction, PNIPAM-mediated droplet motility experiments on fluorophilic coated glass surfaces were established. Towards this end, asymmetric droplets were combined with the coated glass

surfaces and temperature cycling was applied. It was observed that the fluorophilic coating is indeed remarkably promoting PNIPAM-mediated droplet dislocation in the case of asymmetric droplets (**Figure 5.25**). Additionally, also spherical droplets show motility, although not in the same extent as observed for non-spherical ones (see **Appendix Figure SI 14**).

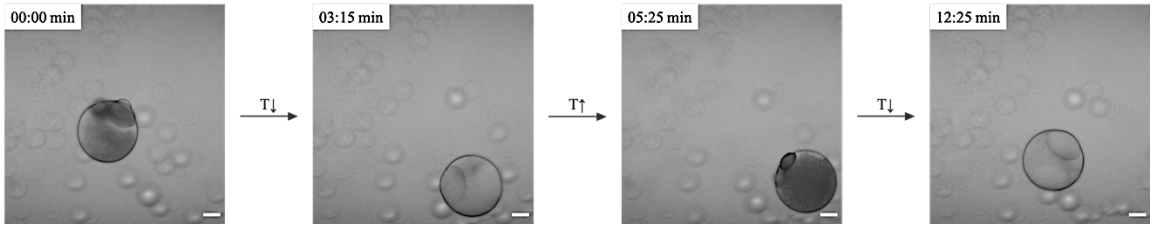

FIGURE 5.25 *FRICTION-INDUCED PNIPAM-MEDIATED DROPLET DISLOCATION*
Asymmetric droplets were prepared as described in Section 4.5.1.1 with gold nanorods, 0.5 M NIPAM, 1 mol% BIS and 0.6 wt% D1173 as aqueous phase. Afterwards, the droplets were transferred into an observation chamber which was constructed using fluorophilic coverslips and temperature cycling was applied (heating rate 0.6 °C/s). Note, the higher contrast in picture 1 and 3 is due to the demixing of PNIPAM during heating-induced polymer transition. The enhanced friction of the coated surfaces is leading to the enhanced dislocation of the observed asymmetric droplets. Scale bar: 50 µm.

Interestingly, when the morphology of the polymer in the migrating droplet and the droplets showing division-like deformation is compared, it can be recognized that the asymmetric droplets showing semi-division behavior containing only one single polymer gel close to the center of the droplet (**Figure 5.26** A; yellow box). Semi-division hereby means no complete division, since no daughter-droplets were formed. The migrating droplets however containing two individual polymer gels that are connected via a joint similar to a welding joint (**Figure 5.26** B; yellow box).

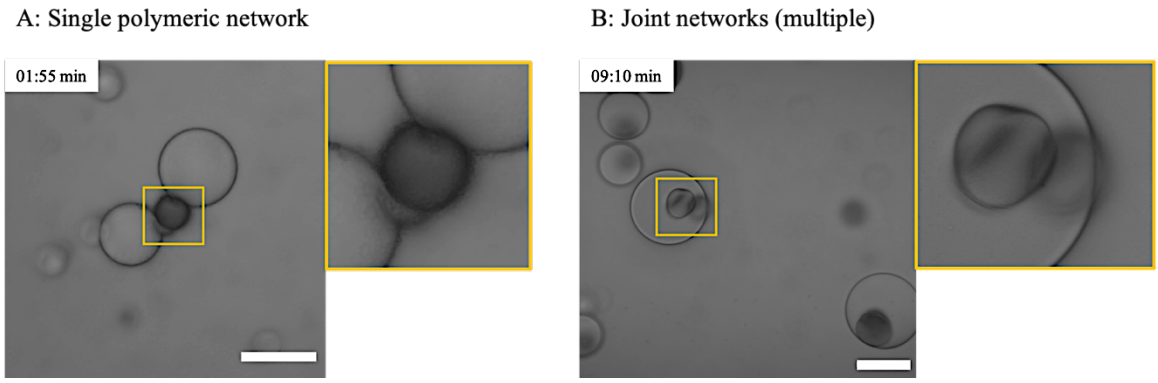

FIGURE 5.26 *COMPARISON OF THE POLYMER ARCHITECTURE DURING DIFFERENT PNIPAM-MEDIATED DROPLET RESPONSE MODES*

Representative widefield images of droplets showing different temperature-induced behaviors, namely division-like deformation (A) and droplet migration (B), respectively. Asymmetric droplets were prepared as described in Section 4.5.1.1 with gold nanorods, 0.5 M NIPAM, 1 mol% BIS and 0.6 wt% D1173 as aqueous phase. Besides the complete confocal image also a close-up showing the respective architecture of the polymeric network is shown. The region of interest is marked with a yellow box. Scale bar: 100 µm.

These preferred polymer constellations are presented in all droplets that show the respective behavior. A closer look at the migrating droplets reveals that, first, one of the two polymer networks undergoes a phase transition and only afterwards, the phase transition in the second polymer network is observed. Thereby, the delay in the phase transition of the two networks does not necessarily have to be sequential. This second phase separation, which is passed on to the droplet, is responsible for the observed migration behavior.

The results for both systems is summarized in **Figure 5.27**. (I) is thereby describing the route of PNIPAM phase transition leading to droplet deformation and sequentially to migration of the droplet, which can be observed for slow heating speeds and enhanced friction caused by fluorophilic surface coatings, while (II) is illustrating the droplet behavior upon fast heating, namely the division-like deformation of the droplets. The responses for both systems, show that by linking synthetic cells with smart materials, fundamental vitally important processes can be implemented in a completely synthetic cell system. This might allow to form a bridge between living and non-living matter and gaining thereby closer insights into the origin of life.

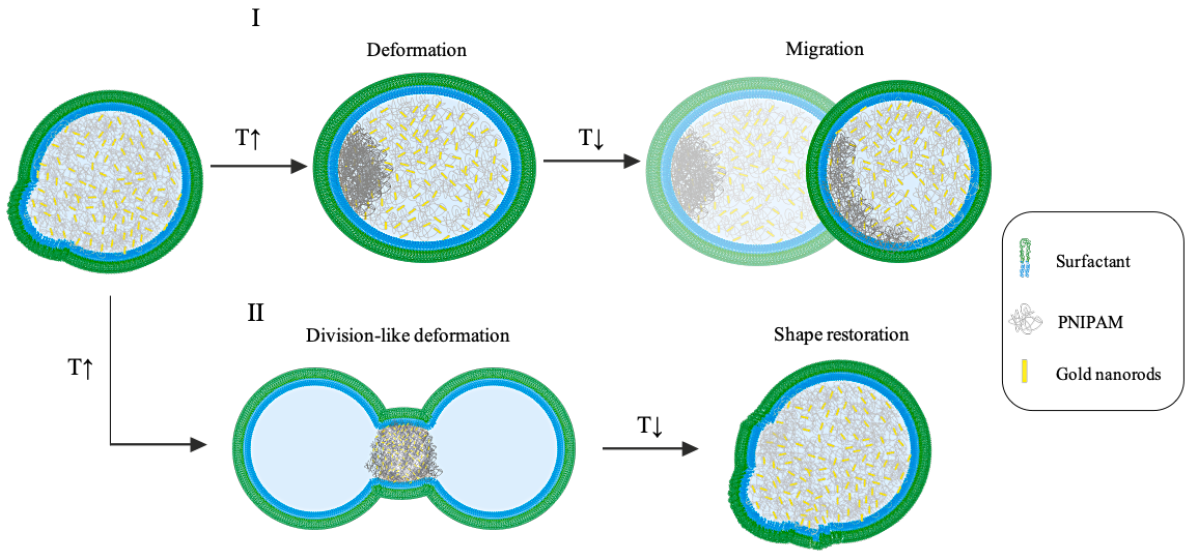

Figure 5.27 *Summary Temperature-Induced Response of the PNIPAM/Gold Nanorods Filled Water-in-Oil Emulsion Droplets*

Schematic illustration of PNIPAM/gold nanorods filled water-in-oil emulsion droplets. PNIPAM is shown in grey, PNS is pictured in green and blue. gold nanorods are represented in yellow. Temperature changes are indicated by "T" in combination with arrows. The different deformation modes of the presented system (deformation → migration, I; deformation → semi-division → shape restoration, II) are depicted with roman numerals.

5.2 PNIPAM Hybrid Systems – A Combination of Synthetic and Natural Components

Although bottom-up synthetic biology allows for the implementation of organic and inorganic materials for the reconstitution of cellular functions, the combination of synthetic and natural components within a synthetic cell is still in its early stages. Therefore, for the first time, I combined the implemented artificial PNIPAM-based cytoskeleton with the natural cytoskeleton component actin in a water-in-oil emulsion-based synthetic cell.

5.2.1 Cytoskeleton Assembly – The PNIPAM/Actin System

5.2.1.1 Evaluation of Cytoskeleton Assembly in Bulk

In order to evaluate the stability of the used F-actin fibers in combination with the artificial PNIPAM-based cytoskeleton material, the appearance of the fibers during different fabrication steps was analyzed. First, rhodamine-phalloidin stabilized F-actin filaments were mixed with a NIPAM polymerization solution and transferred into an observation chamber. Besides the sample containing the natural and the artificial cytoskeleton components, a solution containing F-actin filaments in combination with methylcellulose as state of the art system [191, 192] was also analyzed. Note, methylcellulose is used to generate depletion forces, which results in the formation of thick and long actin bundles (up to 1 µm thick and several µm long). Indeed, the formation of those actin bundles was observed in the control sample (**Figure 5.28** A). However, the combination of the F-actin fibers with the NIPAM polymerization solution led to the aggregation of F-actin instead of bundle formation (**Figure 5.28** B).

Nevertheless, both samples were illuminated with UV light in order to test stability of the F-actin fibers during the illumination and polymerization process (**Figure 5.28** C and D). It was observed that F-actin fibers in the control sample were still stable even after illumination with 365 nm light. In the hybrid sample containing F-actin and NIPAM polymerization solution, the successful formation of PNIPAM was observed. However, since F-actin already had formed aggregates before, no difference between the polymerized and the untreated sample was detectable. This can be explained by the aggregation of the actin filaments caused by the depolymerization and denaturation of actin due to

inappropriate pH values of the NIPAM polymerization solution, which can be solved by the use of appropriate buffers.

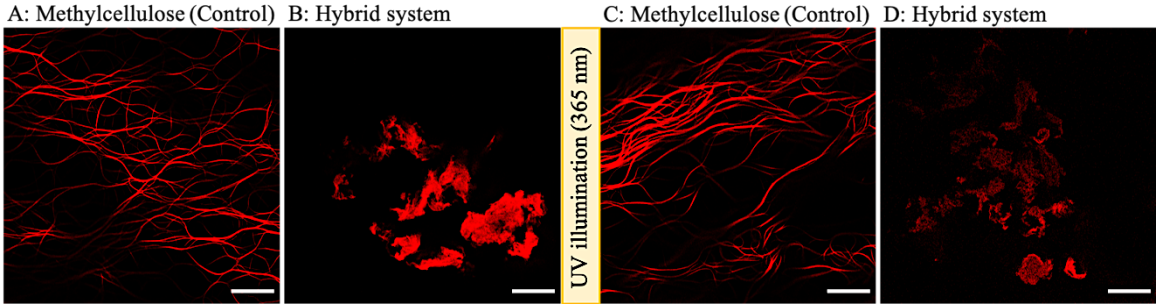

Figure 5.28 *Appearance of Rhodamine-Phalloidin stabilized F-Actin Filaments in Bulk*
Representative fluorescence confocal images of F-actin fibers before and after UV illumination (365 nm, 15 cm, 1 min). (A) Rhodamine-phalloidin stabilized F-actin (50 µM) was mixed with AB buffer containing methylcellulose to obtain a solution containing 10 µM F-actin and 0.4 wt% methylcellulose. (B) Rhodamine-phalloidin stabilized F-actin (50 µM) was mixed with a NIPAM polymerization solution containing gold nanorods, NIPAM, BIS and D1173 to obtain a final concertation of 10 µM F-actin, 0.5 M NIPAM, 5 mol% BIS and 0.6 wt% D1173. After gentle mixing of the components using a pipette, the solutions were transferred into an observation chamber. Afterwards, the samples were treated with UV light (C), (D). Scale bar: 50 µm.

However, in order to be able to analyze the combination of the two cytoskeleton components within a synthetic cell setting, both compositions already used in the bulk experiments were encapsulated in water-in-oil emulsion droplets.

5.2.1.2 Co-Encapsulation of Cytoskeleton Components within the Droplet Confinement

Water in-oil emulsion droplets containing a mixture of NIPAM polymerization solution and rhodamine-phalloidin-labeled F-actin were assembled via the shaking method. As control, an F-actin solution containing methylcellulose was also encapsulated. Following the formation, the droplets were polymerized using UV light (**Figure 5.29**). It was observed that F-actin bundles can be encapsulated in water-in-oil emulsion droplets and do not disassemble during UV treatment (**Figure 5.29** A). However, in the case of PNIPAM/F-actin hybrid droplets, no actin bundles could be detected (**Figure 5.29** B). Nevertheless, the NIPAM polymerization in the presence of actin was successful, which is shown by structures with a higher contrast within the droplets. The lack of actin bundles within the PNIPAM-containing droplets is caused by the radical-induced decomposition of F-actin during polymerization.

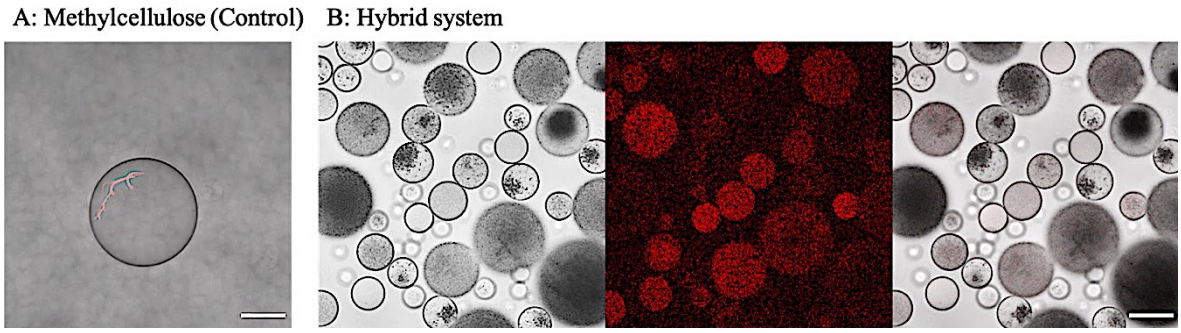

FIGURE 5.29 *UV TREATMENT OF F-ACTIN FILAMENTS IN DROPLET CONFINEMENT*
Respective confocal and fluorescence images of encapsulated F-actin filaments. Droplets were produced using 1.4 wt% CS as oil phase and either a solution containing 0.4 wt% methylcellulose and 10 µM F-actin in AB buffer (A) or a solution containing gold nanorods, 0.5 M NIPAM, 5 mol% BIS, 0.6 wt% D1173 and 10 µM F-actin (B) as aqueous phase. After assembly, the droplets were polymerized using UV light (365 nm, 15 cm, 2 h). Although the successful polymerization of PNIPAM was observed, no F-actin filaments were formed in the hybrid sample. Scale bar: 50 µm.

To overcome this limitation, F-actin filaments were sequentially added into the already polymerized droplets. Therefore, I implemented a microfluidic pico-injection approach for precise injection of actin filaments into preformed PNIPAM-containing droplets. Besides the demonstration of biocompatibility, the successful combination with a highly specialized natural system can serve as an advanced platform towards synthetic cell systems for basic research and potential biomedical applications.

5.2.1.3 SEQUENTIAL ASSEMBLY OF PNIPAM/F-ACTIN CONTAINING SYNTHETIC CELLS

The microfluidic pico-injection method was used to sequentially incorporate F-actin filaments into the preformed PNIPAM-containing droplet confinement without risking filament disassembly during polymerization. Therefore, first NIPAM-containing droplets were produced using a microfluidic chip and polymerized using UV light. Then, rhodamine-phalloidin stabilized F-actin filaments were pico-injected into the PNIPAM-containing droplets.

As can be observed in **Figure 5.30 A** and **Figure 5.31**, sequential pico-injection resulted in successful formation of PNIPAM/F-actin-containing droplets at 25 °C. Moreover, nicely formed F-actin bundles were observed within the droplet confinement. A detailed analysis of F-actin bundles distribution within the droplets revealed that the actin cytoskeleton occupies the PNIPAM-free volume of the droplets (see droplets marked by yellow boxes). In case of droplets without the PNIPAM-based artificial cytoskeleton, equal distribution of the F-actin fibers is observable (blue boxes).

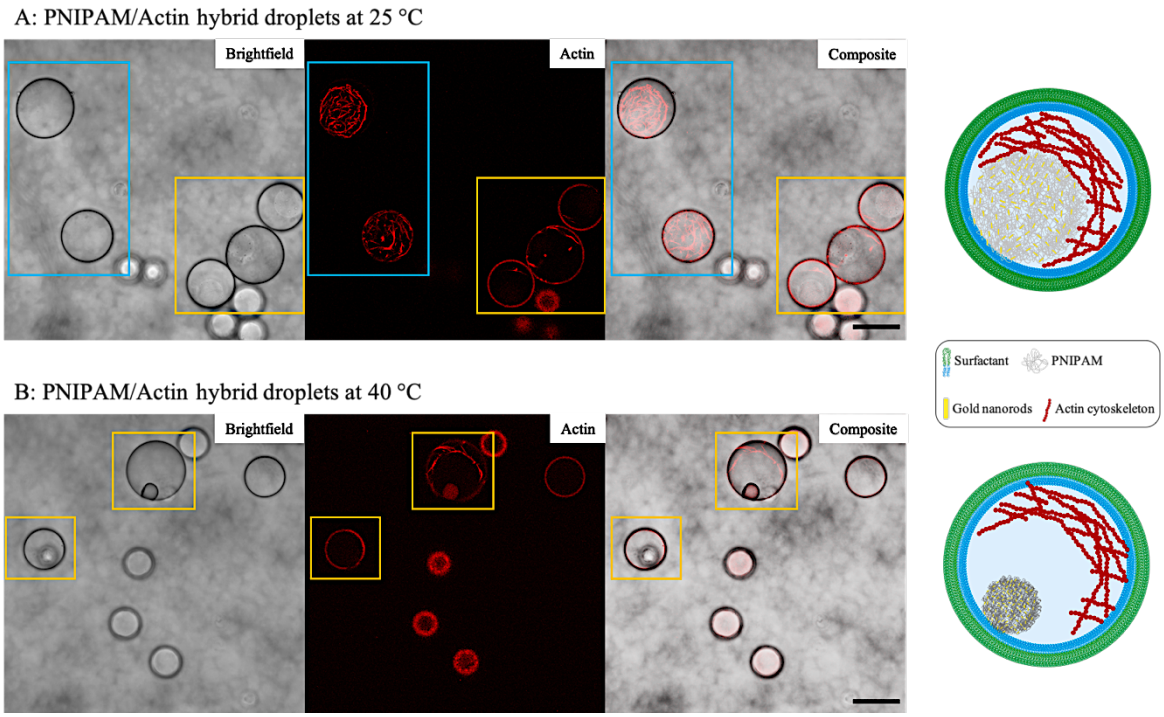

FIGURE 5.30 *CYTOSKELETON ASSEMBLY OF NATURAL AND ARTIFICIAL COMPONENTS*
Water-in-oil emulsion droplets containing artificial and natural cytoskeleton elements were assembled using a sequential pico-injection approach as described in Section 4.6.2. Respective brightfield (left), fluorescence (middle) and composite images (right) of PNIPAM and F-actin containing droplets at 25 °C (A) and 40 °C (B) are shown. Droplets containing the PNIPAM-based artificial cytoskeleton and F-actin filaments are highlighted with yellow boxes, while those droplets containing only F-actin filaments are highlighted by a blue box. Besides, sketches illustrating the F-actin and PNIPAM distribution at 25 and 40 °C are shown rightmost. Scale bar: 50 µm.

Following the assembly of PNIPAM/F-actin containing droplets, the influence of thermo-responsive PNIPAM volume transition on F-actin spatial organization was assessed (**Figure 5.30** B and **Figure 5.31**). Note, in order to prevent temperature-induced denaturation of the F-actin filaments, a maximum temperature of 40 °C was chosen. PNIPAM volume transition could be triggered although longer incubation times of around 20 min before imaging were necessary. Similarly, to the case of PNIPAM-containing droplets only, the increase in temperature induced PNIPAM volume transition to 25% of the initial PNIPAM volume. It is important to mention here that no PNIPAM-mediated deformation of the droplets during the heating cycle was observed. This is due to the fact that the overall droplet volume was increased during the pico-injection process while the polymer volume was constant. Therefore, no droplet deformation during polymer phase transition was observed due to an overall too low polymer volume fraction. Note, the polymer volume transition was not influenced by the introduced actin filaments although a buffer containing different salts was used. This is contrary to measurements in bulk, were a clear dependence of the polymer transition behavior in the presence of different salts was

observed (see **Appendix Figure SI 8**). This suggests that the presence of salts during polymerization disturbs the network structure of PNIPAM, whereas the subsequent introduction of salts seems to have no effect on PNIPAM, but are inevitable for the actin polymerization.

During the shrinkage of PNIPAM and the release of hydrogel-bound water, the actin filaments were pressed against the droplet's periphery, leading to dense actin cortex formation and the rotation of the observed droplets (**Figure 5.31** and **Figure 5.30**, sketches). Importantly, the spatial organization of the F-actin cortex is not influenced by the phase transition of the polymer, meaning that both systems can co-exist within the same droplet without losing their functionality.

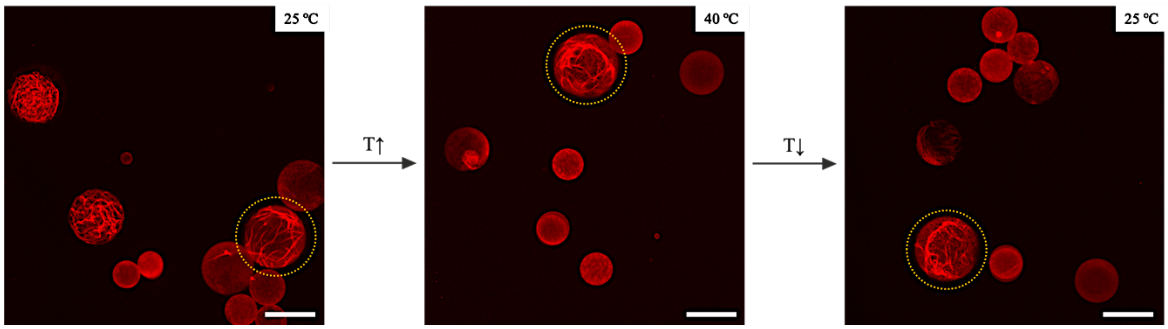

Figure 5.31 *Spatial Organization of the Co-Encapsulated Actin Cytoskeleton during PNIPAM Volume Transition*
Confocal fluorescence images of the spatial organization of the co-encapsulated actin cytoskeleton during temperature cycles. The z-projections of the respective three-dimensional stacks at different temperatures are shown. One droplet containing both, the artificial and the natural cytoskeleton components is marked by yellow dashed circles throughout the whole series. The spatial organization of the F-actin cortex is not altered during the volume transition of the co-encapsulated PNIPAM. Scale bar: 50 µm.

The here presented combinatorial encapsulation of F-actin and the artificial PNIPAM cytoskeleton enabled a controlled spatial organization of an asymmetric actin-based cortex within the droplet confinement. It could be demonstrated, for the first time, that the artificial PNIPAM-based cytoskeleton and natural F-actin could not only be co-encapsulated inside the droplets, but are also still functional showing the biocompatibility of the implemented PNIPAM-based cytoskeleton. Since, in the future, also other components such as myosin [193], tubulin [194], DNA [180] or further materials can be introduced into the droplet confinement after NIPAM polymerization, the system presents a highly versatile and flexible tool for the production of hybrid systems. This allows the here presented system to be combined with other either natural or synthetic components, thus presenting a robust platform for a variety of different biomedical applications.

Summary and Outlook

6 Summary and Outlook

6.1 Summary

Mimicking cellular processes in cell-like compartments is a current research focus in synthetic biology. To achieve this, two different approaches, namely the top-down and the bottom-up approach can be chosen. In addition to naturally-derived proteins, bottom-up synthetic biology allows for implementation of organic and inorganic materials for the reconstitution of cellular functions. Here, for the first time, a straight forward way of assembling an artificial actin analogue in a synthetic cell model system based on a poly(N-isopropylacrylamide) PNIPAM composite material was accomplished. As synthetic cell model, water-in-oil emulsion droplets were chosen and inducible cell migration was reconstituted by the reversible triggering of PNIPAM volume transition.

At first, I characterized and optimized the physicochemical properties of the PNIPAM-based hydrogels in bulk. In addition, gold nanorods with an absorption maximum stated around 750 nm were synthesized and incorporated in the gel matrix. Overall, composite hydrogels with different monomer and crosslinker concentrations in combination with the gold particles were analyzed and the sol content of the composite hydrogels in regards to the crosslinking degree and the influence of gold nanorods was investigated. As expected, a decrease of the sol content in the analyzed hydrogels occurred with increasing crosslinker concentration. However, comparing hydrogels prepared with and without gold nanorods, a higher sol content was detected for gels containing the nanoparticles. This might be due to the removal of not incorporated nanoparticles during the washing step. Afterwards, the phase transition of the composite gels was induced and analyzed. The gold nanorods, as well as different tested NIPAM concentrations did not show any influence on the PNIPAM transition temperature in bulk experiments. In contrast, a crosslinker-dependent change in the transition temperature of the composite gels was observed. With this fine-tuning of the gel composition, the shifting of the transition temperature to a range that fits physiological conditions was achieved.

After the optimization of PNIPAM composite gel performance in bulk, NIPAM polymerization solutions were encapsulated in water-in-oil droplets and directly polymerized within the droplet confinement. As surfactant, a commercially available fluorosurfactant (CS) was used. Although some optimizations were already performed in bulk, the influence of confinement, namely the restricted diffusion of components on the polymer transitioning behavior needed to be evaluated. Therefore, all conditions that were tested in bulk before were also applied in the confined set-up of water-in-oil droplets. Besides the successful encapsulation, also polymerization of NIPAM in the droplets could be achieved. The combination of the PNIPAM/gold nanorods composite hydrogel with water-in-oil droplets led to a temperature-induced deformation of the droplets. The optimal NIPAM concentration to obtain the described morphological changes of the droplets upon polymer volume transition was determined to be 0.5 M. Additionally, by comparing droplets with different gel compositions respective to crosslinker concentration, insights could be gained into the process of temperature-induced phase transition of the polymer network and the influence of this process on droplet deformation. It was shown that a lower crosslinking degree caused a strong deformation of the analyzed droplets upon heating, whereas high concentrations initially led to an equal degree of deformation, which was almost eliminated after several minutes due to hydrophobic interactions and the rearrangement of hydrogen bonds.

After successful encapsulation of functional PNIPAM composite gels within the droplet confinement and the effective triggering of polymer contraction upon heating, a contact between the encapsulated PNIPAM and the inner droplet interface was established. Inspired by nature, attractive lipophilic forces between the encapsulated polymer material and the inner periphery of the droplets were utilized to create a link by functionalizing the inner droplet interface using a thermo-responsive PNIPAM-based surfactant (PNS). The physiochemical properties of the surfactant were characterized and the ability to establish a contact between the artificial cytoskeleton material and the surfactant layer was analyzed. It could be shown, that the synthesized surfactant is in fact enhancing the interactions between the encapsulated composite material and the droplet periphery, which can be seen in a larger contact area between collapsed composite material and the periphery at high temperatures. However, the analysis of the dynamic change of droplet area during PNIPAM volume transition revealed, that the overall degree of deformation of droplets prepared with PNS was lower compared to droplets prepared with CS since PNS exhibited high interfacial

tension (IFT) values leading to a lower deformability of the produced droplets. Nevertheless, regardless of the used surfactant, a reversible transition of the polymer network within the droplet confinement was observed over various temperature cycles.

After optimizing the PNIPAM-based composite gel conditions in bulk and droplet confinement and after analyzing the behavior of the obtained droplets upon temperature cycling, droplet motility induced by changes in the artificial cytoskeleton was triggered. To accomplish cellular-like motility, PNIPAM-containing droplets should experience significant morphological deformation that in combination with sufficient friction with the outer droplet environment would lead to dislocation. Since droplets prepared with PNS showed lower deformability than those prepared with CS, only CS as surfactant was used for the subsequent experiments. Nevertheless, despite the deformation, initially spherical PNIPAM-containing droplets did not show any motility in experiments before. Therefore, inspired by the symmetry-breaking of migrating epithelial cells, asymmetric droplets were created. In a first approach, synthetic cell polarity was achieved by introducing the composite gel-containing droplets into narrow channels of a microfluidic device. This successful implementation of polarization is required for the directional active movement of the synthetic cells in contrast to passive diffusion of the droplets. Additionally to droplet polarization, the pressure gradient across the device led to the division of some of the droplets during temperature-induced PNIPAM phase transition. This reconstitution of cell division is highly desirable and subjected of extensive research. Following, PNIPAM-containing asymmetric droplets (i.e., non-spherical) were created by polymerization and spontaneous fusion of NIPAM-containing stable (1.4 wt% CS) and unstable (0.7 wt% CS) droplets. Upon mixing and polymerization of these droplets, an increased tendency towards fusion was observed. Hence, I observed that the asymmetric droplets indeed showed slight migratory tendencies. Interestingly, in some rare cases a remarkable dislocation of symmetry-broken droplets was observed due to enhanced friction caused by the inhomogeneity of the used glass surfaces. With this in mind, the friction between the used coverslip surfaces and the PNIPAM-containing asymmetric droplets was increased by using fluorophilic surfaces. Indeed, the enhanced friction caused by the fluorophilic surfaces in combination with the forces generated during PNIPAM phase transition of the artificial cytoskeleton material led to the dislocation of the observed droplets. Additionally, this behavior was not only observable for the asymmetric droplets but also for the spherical ones, although not the same magnitude of covered distance was observed. It has thus been

shown that the implemented artificial cytoskeleton material, like its natural counterpart actin, can be used for the manipulation of synthetic cells, in terms of deformation and migration and is therefore highly suitable for the reconstitution of cellular functions within artificial cells.

Following the assessment of PNIPAM-containing droplet motility, I combined, for the first time, PNIPAM- and actin-based cytoskeleton networks within the droplet confinement in order to expand the bandwidth of the bottom-up synthetic biology tool-kit. For the production of this hybrid-network droplets, a microfluidic pico-injection approach for precise injection of actin filaments into preformed PNIPAM-containing droplets was implemented. The combinatorial encapsulation of F-actin and the PNIPAM-based artificial cytoskeleton enabled a controlled spatial organization of an asymmetric actin-based cortex within the droplet confinement that was also stable upon temperature cycling. Additionally, the PNIPAM phase transition was not influenced by the co-encapsulated content. Moreover, the compatibility of the implemented artificial system and nature-derived proteins was shown. The presented work thus offers an important entry point for further research in the field of hybrid systems consisting of natural and synthetic components and an access point for biomedical applications.

6.2 Outlook

6.2.1 Water-in-Oil Emulsion Droplets

Temperature-induced PNIPAM-mediated droplet deformation and motility were achieved in the presented work. Two different types of movement in asymmetric droplets were realized, on the one hand deformation which leads to almost division of the droplets and on the other hand deformation which leads, in combination with friction transmitted by fluorophilic-coated surfaces to the migration of the droplets. These morphological changes of the droplets were achieved by using temperature as trigger. However, the incorporated gold nanorods enable the system to be controlled spatiotemporally due to IR light illumination. Although preliminary tests to induced polymer volume transition using an IR laser were already made, the polymer phase transition was not achieved. This might be due to the shift of the absorption maximum of the nanorods caused by a change of the chemical and physical environment in the composite gels. Nevertheless, this light-trigger, which allows for the spatiotemporal control of the droplets response, would further enhance the attractivity of the system. With this, guided migration or a complete division of droplets containing the artificial cytoskeleton material might be achieved. This would take research one step further towards the production of an artificial cell from scratch using only synthetic components.

The application possibilities of the developed artificial cytoskeleton can be further increased by transferring it from water-in-oil droplets to a water-in-water system such as polymersomes and/or giant unilamelar vesicles. The surfactant layer can thereby for example be replaced by an amphiphilic polymer shell with the same viscoelastic properties or by lipids (see **Section 4.7**) thus allowing to implement motility of synthetic cells in more physiological conditions. Moreover, additional synthetic mimetics of natural cell components such as integrin analogues which will function as anchoring point between the synthetic cells and the substrate during migration or a linker between the PNIPAM-based cytoskeleton and the synthetic cell membrane to enhance the PNIPAM-mediated deformation could be introduced.

6.2.2 PNIPAM Hybrid Systems

6.2.2.1 Cytoskeleton Assembly

For the first time, the combination of the artificial PNIPAM-based cytoskeleton and the natural cytoskeleton protein actin in water-in-oil emulsion droplets was achieved. The production of these droplets was accomplished by sequential pico-injection. This proof of compatibility with nature-derived substances could be further extended. Other components of the natural cytoskeleton complex, such as actin motor proteins like myosin II could be co-encapsulated in order to trigger contractility via chemical cues (Mg^{2+}/ATP). With this, two functional cytoskeleton complexes, a natural and an artificial one could be presented within one cell-like compartment. This might lead to a complementary relationship between both cytoskeleton complexes and could add an additional chemical stimulus to trigger actin contractility, since motor proteins are triggered by ATP hydrolysis. Additionally, the incorporation of two individual cytoskeleton complexes is leading to a symmetry breaking within the synthetic cells. This symmetry breaking, which is crucial for fundamental natural processes like cell migration [197], is so far hard to achieve in a synthetic system and of current research interest [198].

Besides cytoskeleton components, also different other components could be co-encapsulated with the PNIPAM-based cytoskeleton which can be spatially triggered. Caged ATP that can be released using light as trigger could be encapsulated for instance, thus allowing for the spatiotemporal control of natural and artificial cytoskeleton contractility [183]. Besides, membrane-enclosed sub-compartments which can provide an H^+-gradient needed for the synthesis of ATP could be encapsulated. This would enable the independent synthesis of ATP and thus the provision of energy for the contraction of the natural cytoskeleton components.

6.2.2.2 Lipid-Encapsulated Microgels

Besides the use of synthetic materials like surfactants for the compartmentalization, also natural materials like lipids can be used for the production of artificial cells containing the PNIPAM-based cytoskeleton. The assembly of those lipid-enclosed cells could be realized in two ways, either by encapsulating the NIPAM polymerization solution within

the lipid-bilayer support confinement (unilamelar vesicles) and subsequent polymerization or by encapsulating PNIPAM microgels within a lipid-bilayer.

Throughout this project, both approaches were tested. Nevertheless, the encapsulation of NIPAM polymerization solution in vesicles and the following polymerization did not lead to the formation of a responsive PNIPAM network. A potential explanation might be the interference of the lipids with the radicals that are formed during the polymerization process and the rapid change of the environment, for example pH, in the confined vesicle state. However, responsive PNIPAM microgels could be generated. This was accomplished in the same way as the production of water-in-oil emulsion droplets, though instead of fluorinated surfactants and oil, silicon oil and a respective surfactant was used (see **Section 4.7**). The advantage of the system is the easy removal of the oil and surfactant layer which results in PNIPAM microgels with a size between 5 – 100 µm. The size can be tuned by the used emulsification method (vortex vs. emulsificator). The coating of the microgels was successful, however no lipid-bilayer could be obtained but a random adsorption of the lipids. This might be caused by the fact that lipids were applied onto freeze-dried microgels which were rehydrated afterwards. This led to the equal distribution of the lipids within the whole microgel. Nevertheless, the microgels responded to temperature changes by a reduction of microgel volume upon heating. Importantly, the behavior of the polymer is not influenced by the lipids as was observed for the vesicle system.

However, if the successful encapsulation of the microgels in the lipid bilayer-supported confinement can be achieved, different applications are imaginable. The small lipid-coated microgels might be used as synthetic vesicles that can be uptaken into cells. Since the polymer microgels can collapse above the transition temperature and water is expelled from the gel particles, the microgels can be used as drug carriers. The bigger sized particles might be used as cell analogues with switchable mechanical properties. Since the microgels can be further functionalized with cell-cell contact proteins like cadherins and cell-substrate contact proteins like integrins due to the lipid layer, the mechanical influence on processes like cell migration can be investigated.

The presented ideas for further projects show that the PNIPAM-based cytoskeleton can be used in versatile ways and can be spatiotemporally controlled due to the

implemented gold nanorods. This paves the way for the production of synthetic cells from scratch.

Appendix

Appendix

A – Supplementary Information

A.1 FTIR Spectra

The FTIR spectrum of the thiolated surfactant (**Figure SI 1**) shows major bands at 1500, 1550, 1680, 2660 and 2900 – 3200 cm^{-1}. The peaks at 1500 and 1550 cm^{-1} are correlated to the deformation modes of the (CH_2) groups of the PEG molecule, indicating a successful reaction between Krytox and thiolated PEG. The peak at 1680 cm^{-1} is attributed to the (C=O) stretching bond . Note, no peak at 1775 cm^{-1} corresponding to the Krytox starting material is visible in the spectrum of the thiolated surfactant indicating a complete reaction of the starting material. The weak peak at 2660 cm^{-1} is correlated to (S-H) end group of the thiolated surfactant. The bands between 2900 – 3200 cm^{-1} are attributed to the valence vibration modes of the (CH_2) groups.

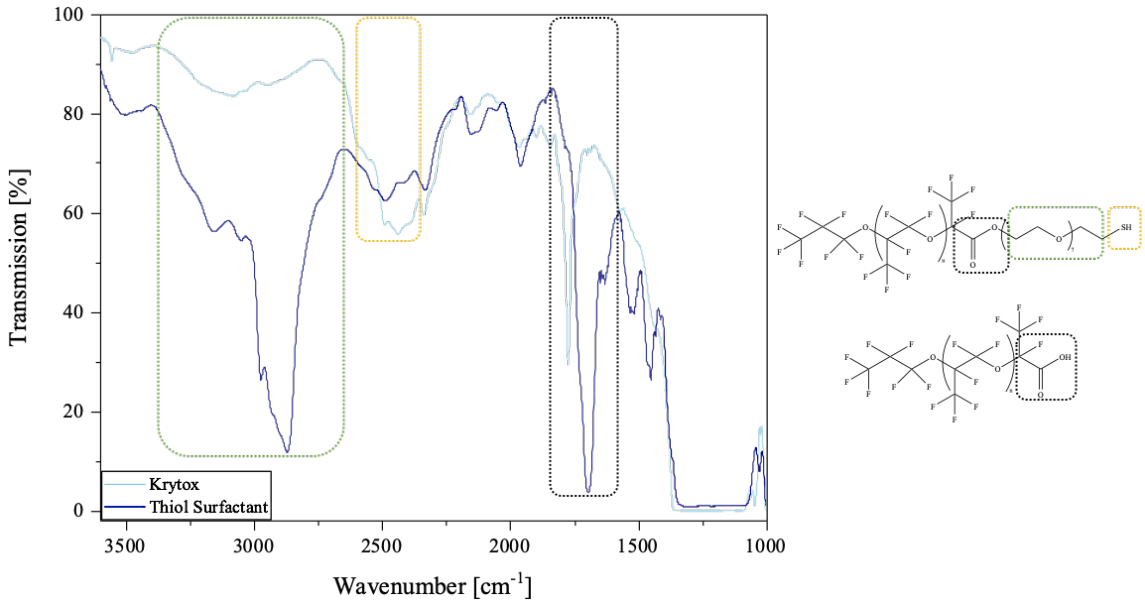

Figure SI 1 *Representative FTIR Spectra of Thiolated Surfactant*
Overlay of FTIR transmission spectra of precursor molecule (light blue) and surfactant (dark blue). All substances were measured as pure molecules without addition of solvent. Wavenumber is given in cm^{-1} and transmission in %. Characteristics bands are marked in the spectra and the chemical structures by colored boxes, respectively.

The FTIR spectrum of the gold-linked surfactant (**Figure SI 2**) shows identical bands between 1000 – 2500 cm^{-1}. Note, a small shift of the thiol peak in the gold-linked surfactant is visible (2660 cm^{-1} in the thiol precursor molecule to 2670 cm^{-1} in the gold-coupled product, shift of 10 cm^{-1}). The peak at 2900 cm^{-1} represented in the thiolated surfactant is splitted in two peaks (2900 and 2950 cm^{-1}) in the gold-linked surfactant.

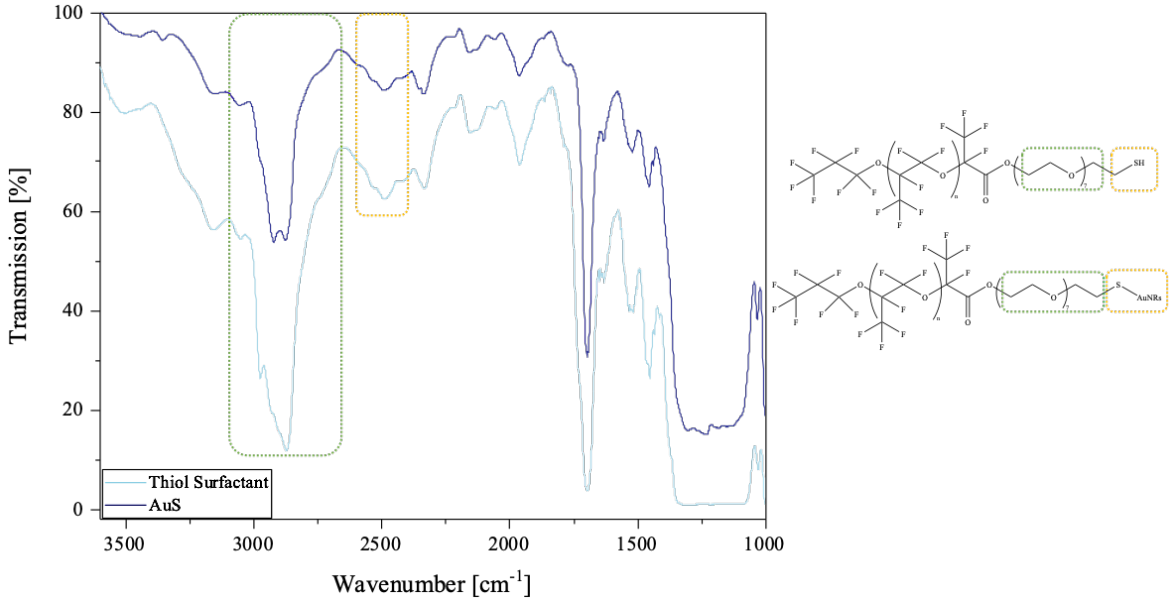

FIGURE SI 2 *REPRESENTATIVE FTIR SPECTRA OF GOLD-LINKED SURFACTANTS*
Overlay of FTIR transmission spectra of precursor molecule (light blue) and surfactant (dark blue). All substances were measured as pure molecules without addition of solvent. Wavenumber is given in cm^{-1} and transmission in %. Characteristics bands are marked in the spectra and the chemical structures by colored boxes, respectively

A.2 UV VIS SPECTRA

The UV Vis spectra of the aqueous and the oil phase of the coupling reaction between the thiolated surfactant and the synthesized gold nanorods before and after the reaction is shown in **Figure SI 3**. The UV Vis spectra of the aqueous as well as the oil phase are showing a successful reaction since typical bands of the used gold nanorods are visible in the spectra of the gold-linked surfactant, while the bands disappear in the spectrum of the aqueous phase after the reaction.

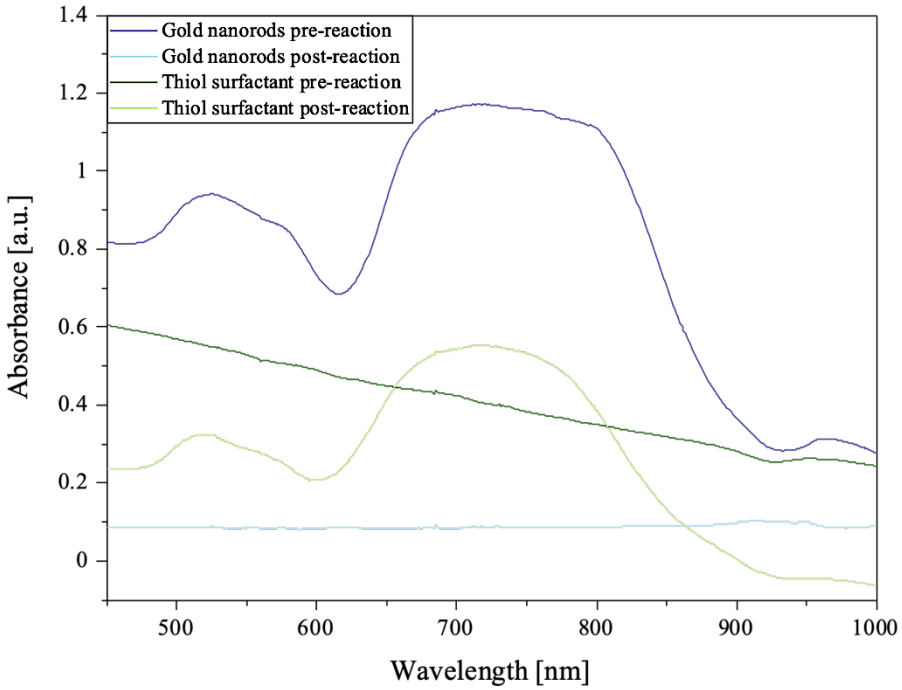

FIGURE SI 3 *CONFIRMATION OF THE COUPLING REACTION BETWEEN GOLD NANORODS AND THE THIOLATED SURFACTANT*

Representative UV Vis spectra of solutions either containing gold nanorods or thiolated surfactant before and after the coupling reaction. For the reaction and the measurements, gold nanorods with a concentration of 9.5×10^5 particles/ml dissolved in LC-MS grade water were used. The surfactant was dissolved in 2,2,2-Trifluoroethanol for the reaction since the miscibility with water could be ensured in this way. UV Vis measurements of the surfactants were performed in FC-40 (used concentration: 2.5 mM). The UV Vis spectrum of the aqueous solution before the coupling reaction is depicted in dark blue and after the reaction in light blue. As blank, LC-MS grade water was used. The spectrum of the thiolated surfactant prior to the reaction is depicted in dark green, and the spectrum of the gold-linked surfactant in light green. For measurements of the surfactant solutions, FC-40 was used as blank. Since the characteristic nanorod bands are visible in the UV Vis spectrum of the oil phase after the reaction, the successful coupling of the thiolated surfactant and the gold nanorods could be shown.

To test the reproducibility of the gold nanorods synthesis, several batches of nanoparticles were obtained and analyzed using UV Vis spectrometry (**Figure SI 4**). The comparison of the spectra of the different batches revealed, that the absorption band of the long axis is centered around (752 ± 9) nm for all measured samples, indicating a reproducible synthesis of the Gold nanorods. Also the absorption band of the short axis is located around the same wavelength.

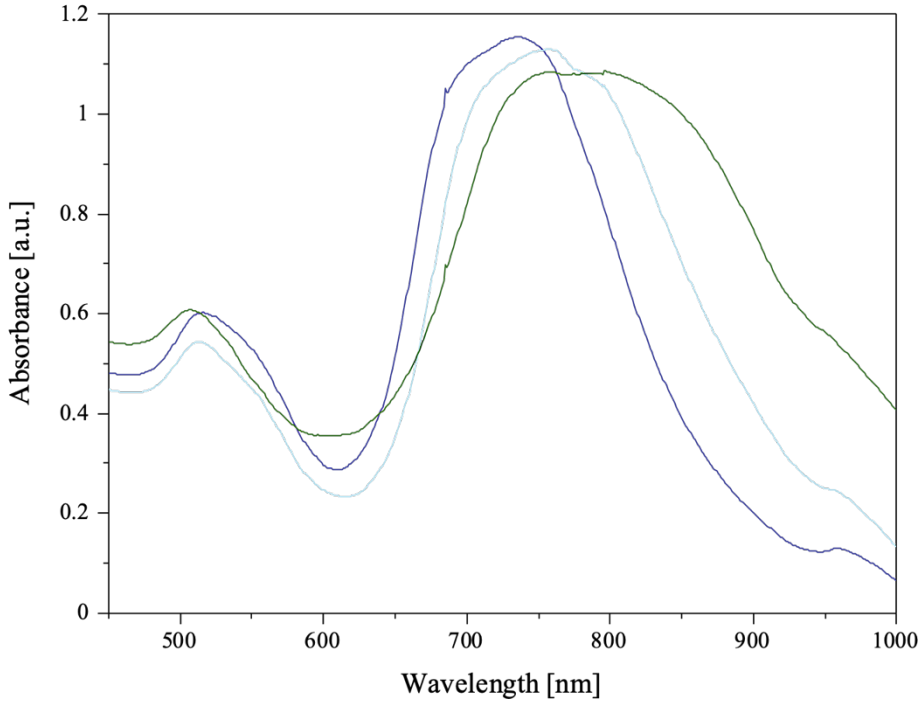

FIGURE SI 4 *COMPARISON OF THE REPRODUCIBILITY OF THE GOLD NANORODS SYNTHESIS USING UV VIS SPECTROMETRY*

The reproducibility of the synthesis of gold nanorods in several batches was tested using UV Vis spectrometry. For the measurements, gold nanorods with a concentration around 9.5×10^5 particles/ml were used. The different reaction batches are depicted in different colors in the graph. Gold nanorods with in the error interval identical absorption maxima over several batches were obtained.

A.3 PENDANT DROP TENSIOMETRY MEASUREMENTS

Pendant drop tensiometry measurements of pure PNIPAM (**Figure SI 5**) were performed to test its use as potential surfactant. Compared to pure FC-40 (49.964 mN/m), PNIPAM is reducing the IFT by about half at 25 °C and almost three times as much at 40 °C. These results show the amphiphilic character of PNIPAM and suggesting that PNIPAM alone might be sufficient for the stabilization of water-in-oil droplets. However, stable droplets could not be produced without the use of surfactants.

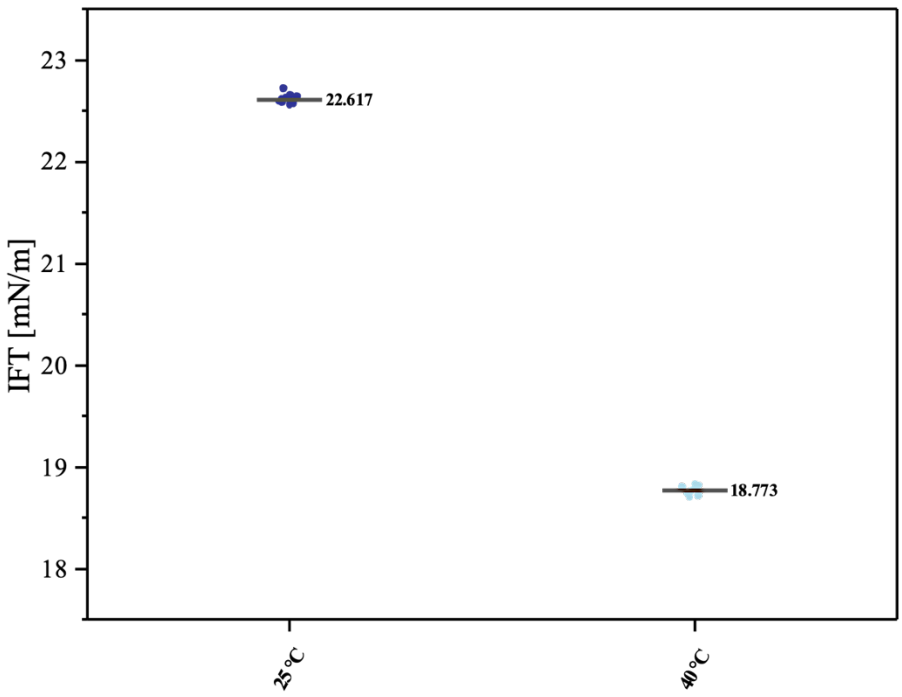

Figure SI 5 *Determination of Surfactant Properties of Pure PNIPAM*
Interfacial tension of pure PNIPAM was determined using a pendant drop set-up. For the measurements, PNIPAM was dissolve in Type 1 water (100 µM) and measured against pure FC-40. For every temperature value, 10 individual droplets were measured and the mean displayed in the plot. IFT values acquired at 25 °C are shown in dark blue, values captured at 40 °C are shown in light blue. A decrease of the IFT value upon temperature increase in the same range as observed for PNS and CS was found.

A.4 MALDI-TOF MS Spectra

MALDI-TOF MS measurements of the PNIPAM-based surfactant were performed. In addition, also the amine-terminated PNIPAM starting compound was measured. The mass spectra revealed the successful coupling of PNIPAM to PFPE, which can be seen by distinct mass patterns of both compounds in the spectrum of PNS (**Figure SI 6**). Additionally, the average mass of the surfactant is centered around 9000 g/mol which is in accordance with the expectations.

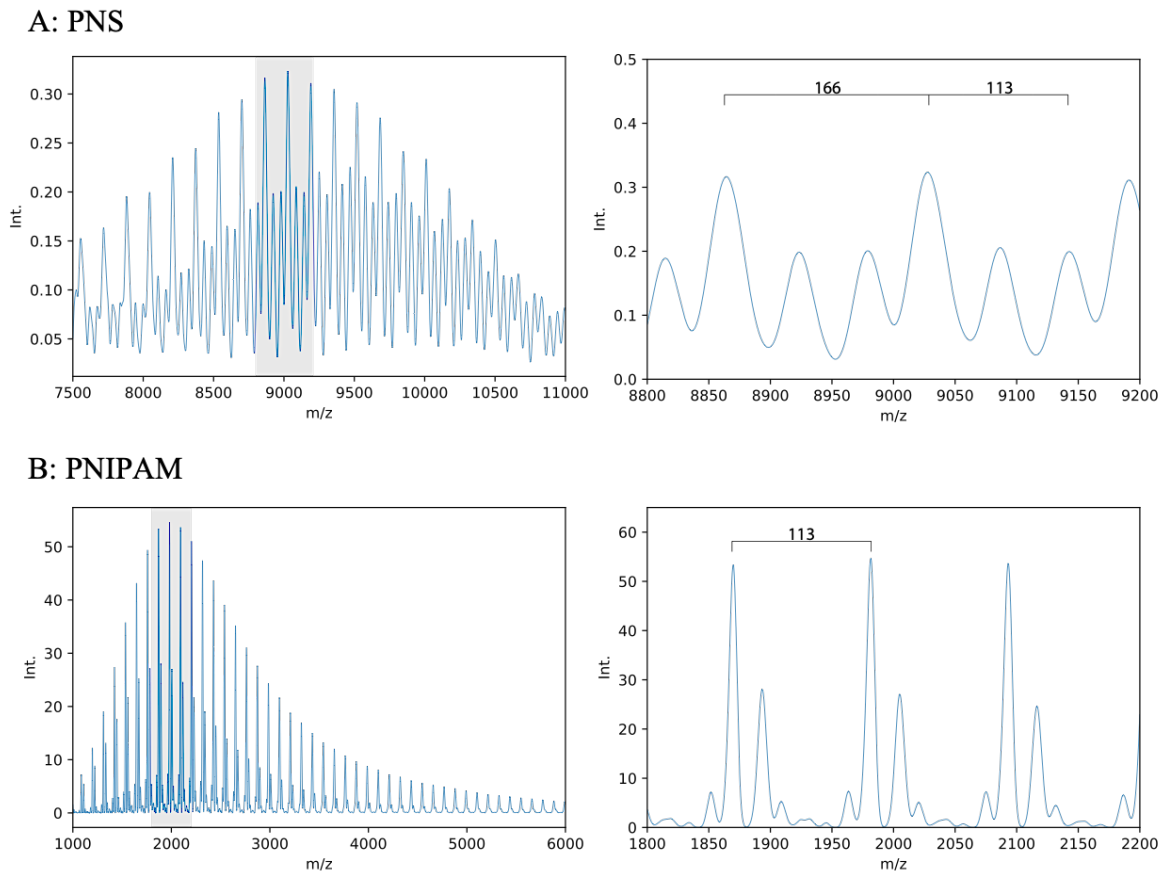

FIGURE SI 6 *MS ANALYSIS OF PNS*

MALDI-TOF MS measurements of PNS (A) and amine-terminated PNIPAM (B). For both compounds, the whole spectrum is shown on the left side, while a close-up of the region with grey background is depicted on the right side. In both close-ups, distinct mass patterns of PNIPAM (Δm/z = 113) are visible. In addition, the PNIPAM-based surfactant is also showing the mass pattern of the PFPE polymer (Δm/z = 166).

A.5 Transition Temperature Measurements

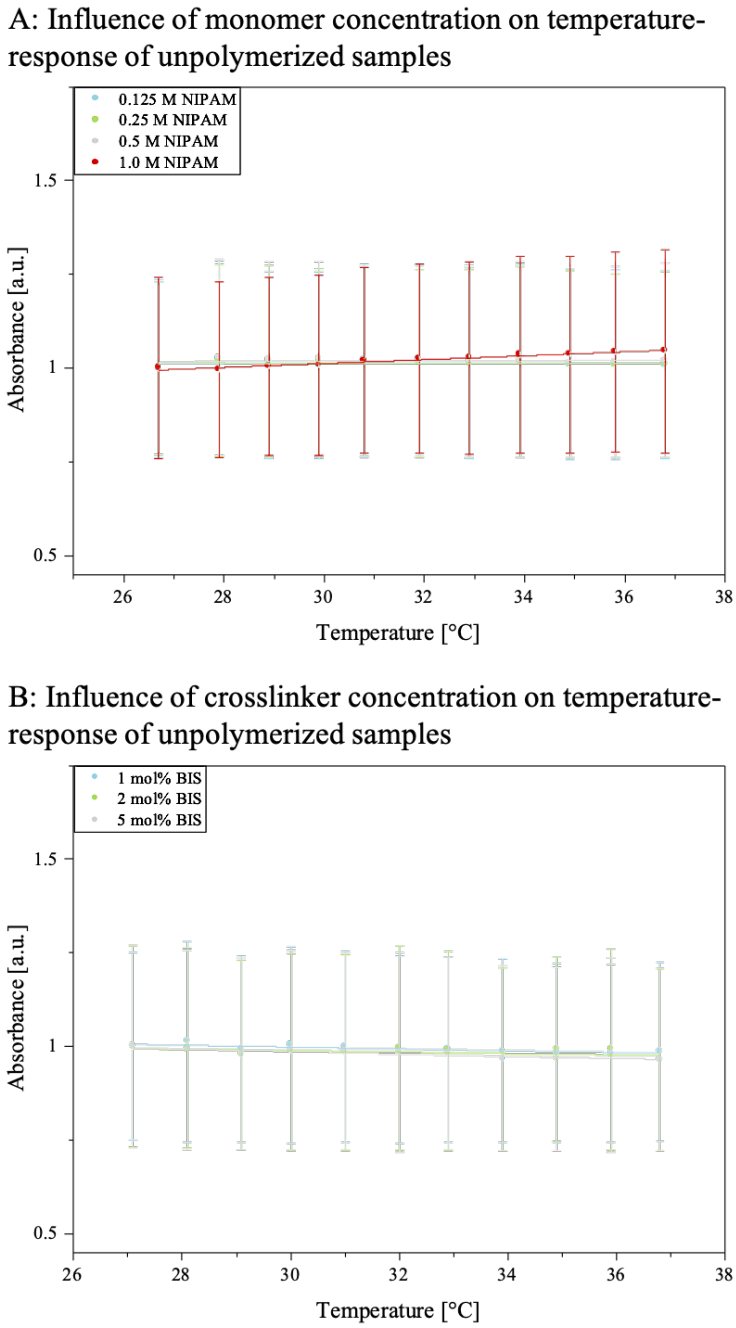

Figure SI 7 *Transition Temperature Controls*
Unpolymerized control samples containing either different amounts of NIPAM (A) or different amounts of the crosslinker (B). For all samples, the amount of gold nanorods (9.5×10^5 particles/ml) and photoinitiator D1173 (0.6 wt%) was kept constant. For samples prepared with different NIPAM concentration, the amount of crosslinker was kept constant at 1 mol%, while for samples prepared with different BIS concentrations, a fixed NIPAM amount of 0.5 M was used. Absorption values were determined at 680 nm using a plate reader. Every set of measurements was performed between 27 °C and 37 °C within 1 °C steps and every sample was prepared as pentaplicate. For data analysis, the absorption values were normalized to the starting value at 27 °C. The control samples showed no significant change in absorption during the heating cycle.

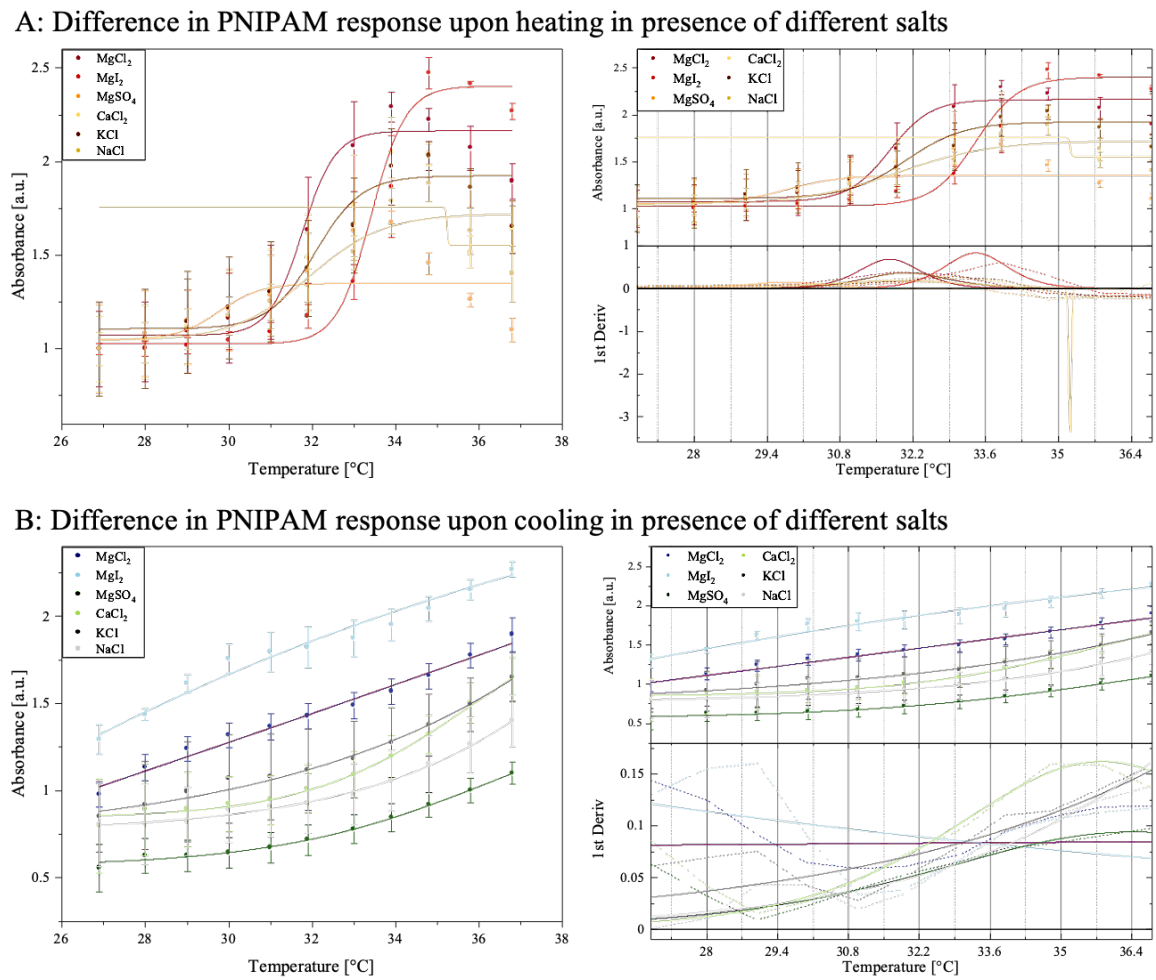

FIGURE SI 8 *INFLUENCE OF DIFFERENT SALTS ON THE TRANSITION TEMPERATURES*

The volume transition behavior of the PNIPAM-based composite material was determined in the presence of different salts. For the preparation of composite gels containing different salts, solutions containing gold nanorods (9.5×10^5 particles/ml), 0.5 M NIPAM, 1 mol% BIS, 0.6 wt% D1173 and 30 mM of the respective salt were prepared. 100 µl of those polymerization solutions were transferred into a 96-well plate and afterwards polymerized (Hamamatsu Lightningcure LC8, 365 nm, 15 cm working distance, 10 min). The polymerized gels were swollen in 100 µl LC-MS grade water for 24 h prior to absorption measurements. Absorption values were determined at 680 nm using a plate reader. Every set of measurements was performed between 27 °C and 37 °C within 1 °C steps and every sample was prepared as pentaplicate. To determine the transition temperature of hydrogels in bulk, the first derivative was calculated by fitting the data with a sigmoidal "dose response fit". The displayed graphs show on the one hand the change in absorption with temperature change (left) and on the other hand the determination of the phase transition temperature using the first derivative (right). The dotted lines show the first derivative of the actual data at the respective temperature, while the bold lines represent the first derivative of the fit function. The transition behavior of the salt-containing composite gels upon heating (A) and cooling (B) is shown. It was observed that the different salts are influencing the transition temperature of the PNIPAM composite gel in such a way that the before observed reversible volume transition is hindered.

A.6 Droplet Analysis

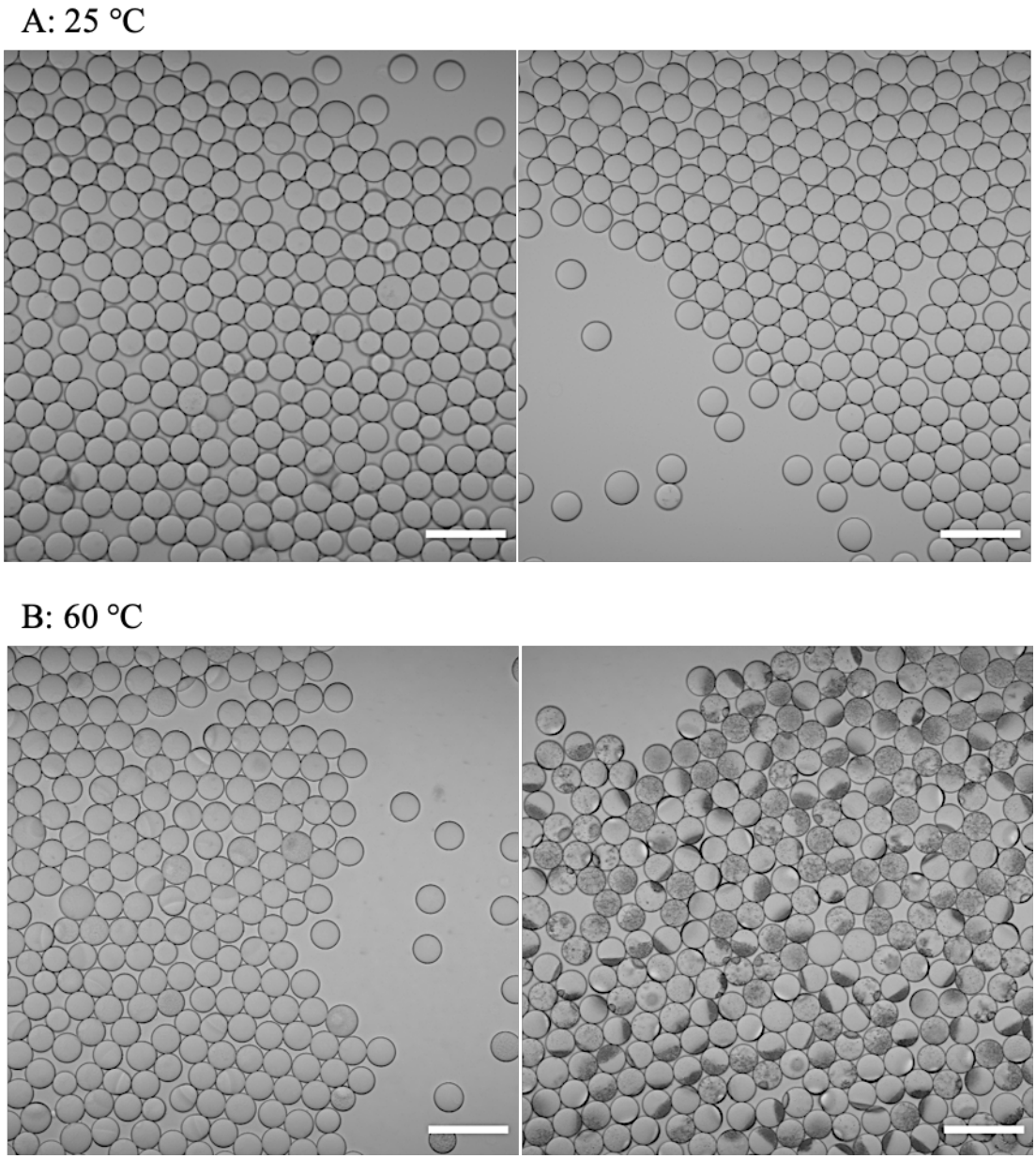

Figure SI 9 *Monodispersity of PNIPAM-Containing Water-in-Oil Emulsion Droplets*
Droplets were prepared according to the protocol described in Section 4.5.1.2 with 5 mol% BIS, 0.5 M NIPAM and 5 wt% CS as oil phase. After assembly, the droplet samples were polymerized for 2 h (365 nm, 15 cm working distance). (A) Monodisperse droplets at 25°C are shown. (B) PNIPAM volume transition in monodisperse water-in-oil droplets at 60 °C. Scale bar: 50 µm

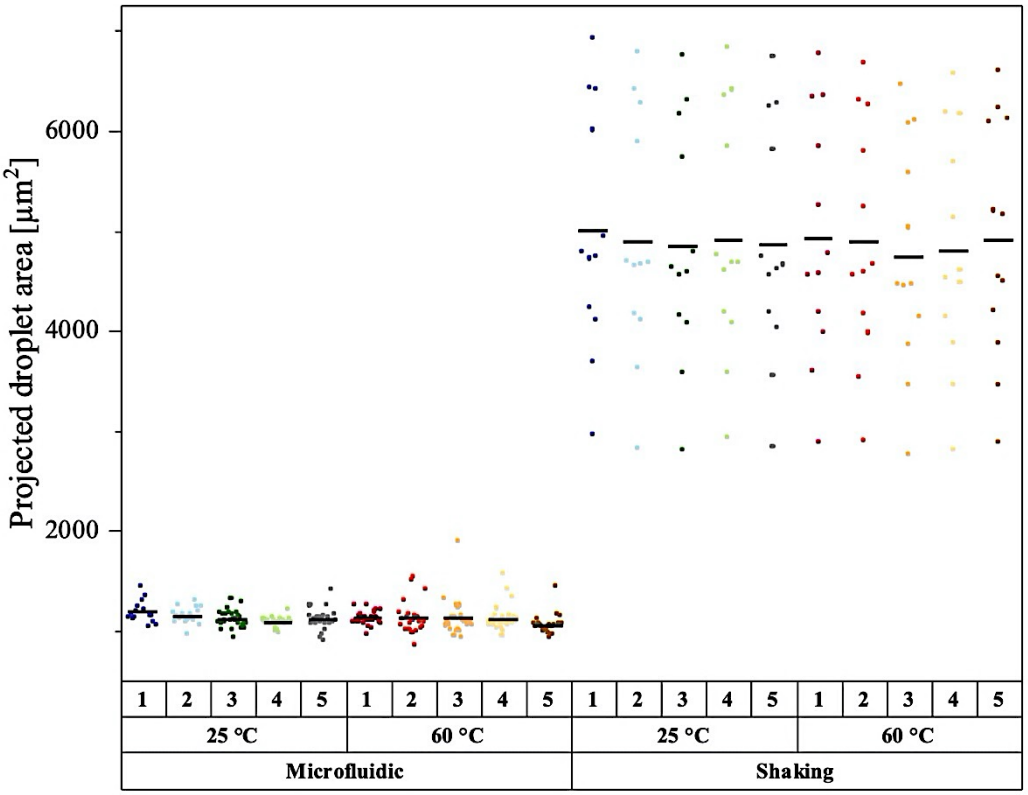

FIGURE SI 10 *INFLUENCE OF PRODUCTION METHOD ON PNIPAM-MEDIATED CHANCE OF THE DROPLET AREA*
Droplets were prepared as described in Section 4.5.1.2 and 4.5.1.1 using either 5 wt% CS (microfluidic chip production) or 1.4 wt% CS (shaking method). The area of droplets during five heating and cooling cycles were determined. Data collected for droplets produced via microfluidic chips is displayed on the left side, while the values determined for droplets produced via the shaking method are shown on the right side, respectively. The area of the droplets at 25 °C is shown in blue/green shades, while the values at 60 °C are depicted in red/yellow shades. Independent of the used droplet production method, the same trends upon temperature cycling were observed for samples prepared with the same polymer composition and the same surfactant. This proves that the reversible temperature behavior of the droplets is only influenced by the polymer and surfactant composition, but not by the production method.

A.7 Cryo-SEM Micrographs

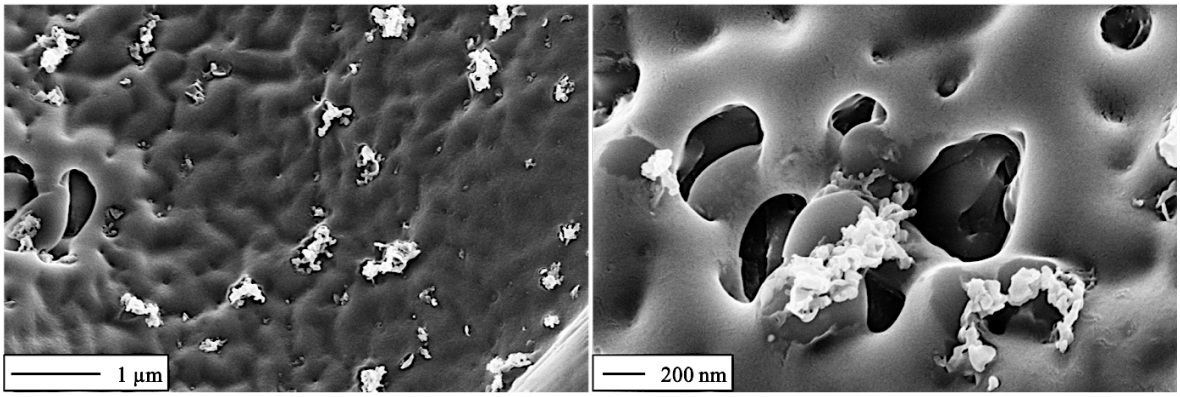

Figure SI 11 *Detection of Gold Nanorods inside Water-in-Oil Droplets*
Droplets were prepared as described in Section 4.5.1.2, but instead of a NIPAM polymerization solution, a solution of pure gold nanorods (9.5×10^5 particles/ml) was used. Before freeze-fracturing, droplets were heated to 60 °C using a water bath. SEM micrographs on the left side are showing the overview of the inner droplet space of one droplet, while in the micrographs on the right side a close-up of the gold nanorods distribution in the droplet is depicted. The respective scale bars are shown in the micrographs.

A.8 Time-Lapse Images

In order to test the stabilizing behavior of PNIPAM alone, water-in-oil droplets containing 100 µM PNIPAM-COOH in Type 1 water as aqueous phase and either 2.5 mM PNS or FC-40 as oil phase were prepared in a microfluidic production chip and the appearance of the droplets at the T-junction and the outlet was analyzed (**Figure SI 12**). It was observed that stable droplets could be obtained in the case of 2.5 mM PNS, while the droplets prepared without surfactant in the oil phase fused (**Figure SI 12**, left side). This indicates that PNIPAM alone is not sufficient to stabilize water-in-oil emulsion droplets although its amphiphilic character and an additional surfactant is required to form a stable emulsion.

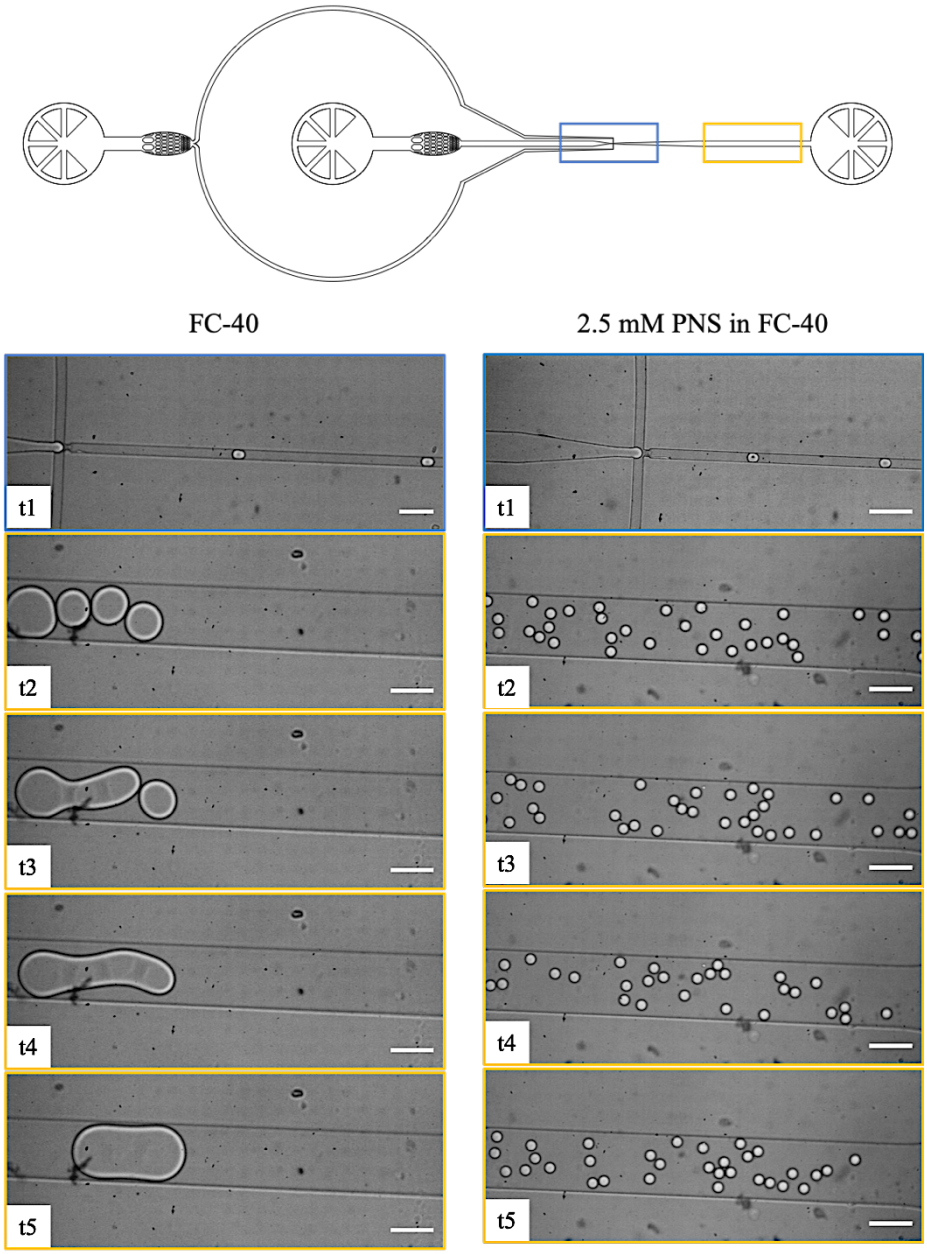

FIGURE SI 12 *DETERMINATION OF STABILIZING PROPERTIES OF PNIPAM*
The stabilizing properties of PNIPAM were evaluated using a microfluidic production device. The droplets were prepared in the deice and the appearance was checked at the droplet-producing T-junction (blue boxes) and the outlet of the device (yellow boxes). Besides the schematic drawing of the design of the microfluidic device, representative time lapse images of the droplets produced with and without surfactant at the T-junction and the outlet are shown. The appearance of the droplets at different time points (t 1- t5) is depicted. It was observed that droplets produced without the addition of surfactant are fusing within the production device, meaning that stable droplets could only be achieved in the presence of the surfactant. PNIPAM alone was not sufficient to stabilize the produced droplets. Scale bar: 100 µm.

Asymmetric droplets show a PNIPAM-mediated motility during temperature cycling. In most of the cases the overall dislocation during the migration process is rather small. However, in some rare cases, a significantly higher dislocation is observable (**Figure**

SI 13), which is most likely caused by enhanced friction between the droplets and the glass surface due to surface defects.

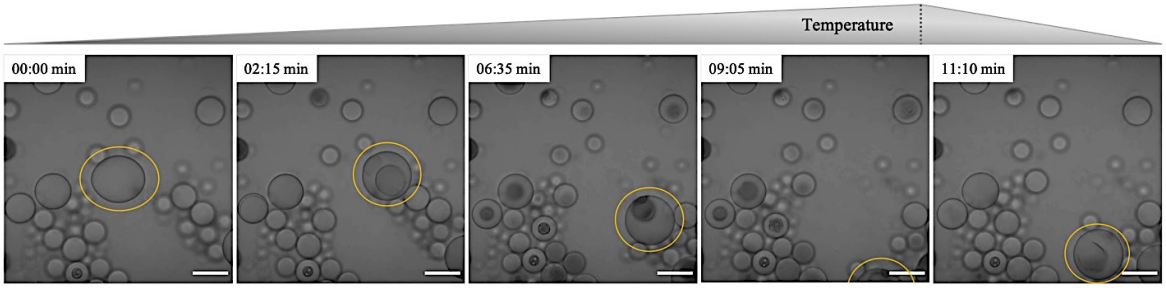

FIGURE SI 13 *ASYMMETRIC DROPLET SHOWING HIGH PNIPAM-INDUCED MOTILITY*
Asymmetric droplets were generated by mixing stable (1.4 wt%) and unstable (0.7 wt%) droplets containing a NIPAM polymerization solution with 1 mol% BIS prior to polymerization (2 h, 365 nm, 15 cm working distance). Afterwards, the droplets were subjected to one heating and cooling cycle (25 °C → 60 °C → 25 °C). The position of one droplet (yellow ellipsoid) during this temperature cycling was tracked. The change of temperature during the experiment is indicated by grey temperature triangle with a dotted line to indicate the start of the cooling period. Scale bar: 50 µm.

Besides the migration of asymmetric droplets, droplet motility of spherical droplets using fluorophilic-coated surfaces could be observed. The overall minor dislocation of the droplets was hereby expected. Nevertheless, in contrast to spherical droplets on uncoated surfaces, motility of the droplets on fluorophilic surfaces was achieved.

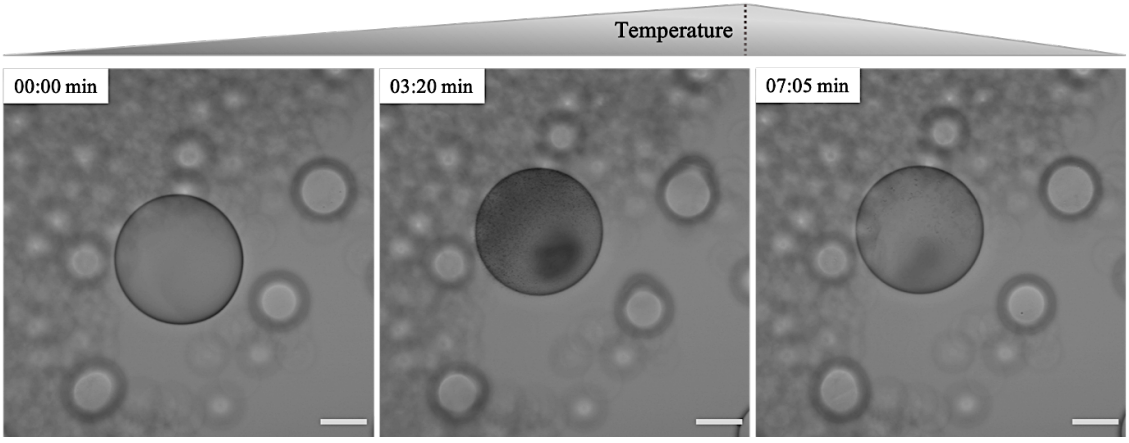

FIGURE SI 14 *MIGRATION OF SPHERICAL DROPLETS ON FLUOROPHILIC SURFACES*
Motility of a PNIPAM-containing spherical droplet on a fluorophilic-coated glass substrate. The incorporated PNIPAM-based artificial cytoskeleton was prepared with 1 mol% BIS. The droplets were heated and cooled between 25 and 60 °C. The position of the droplet during this temperature cycling at distinct time points is shown. The change of temperature is indicated by a grey temperature triangle with a dotted line to indicate the cooling period. Scale bar: 50 µm.

B – List of Publications

[1] **Désirée Sauter**, Martin Schröter, Christoph Frey, Cornelia Weber, Ulrike Mersdorf, Jan-Willi Janiesch, Ilia Platzman, Joachim P. Spatz. PNIPAM-containing droplets: the route towards an artificial cytoskeleton assembly based on synthetic and natural components. In preparation.

C – List of Figures

D – List of Tables

Bibliography

[1] Ruiz-Mirazo, K.; Peretó, J.; Moreno, A. A. Universal Definition of Life: Autonomy and Open-ended Evolution. *Origins of Life and Evolution of the Biosphere* **2002**, 34, 323-346

[2] Sagan, C.; Sagan, D.; Augustyn, A.; Das, D.; Gregersen, E.; Higgins, J.; Lotha, G.; Metych, M.; Rafferty, J. P.; Pallardy, R.; Sampaolo, M. Life. *Encyclopædia Britannica Inc*. **2020**, https://www.britannica.com/science/life

[3] Dodd, M. S.; Papineau. D.; Grenne, T.; Slack, J. F.; Rittner, M.; Pirajno, F.; O'Neil, J.; Little, C. T. S. Evidence for early life in Earth's oldest hydrothermal vent precipitates. *Nature* **2017**, 543, 60-64

[4] Peretó, J. Controversies on the origin of life. *Int. Microbiol*. **2005**, 8, 23-31

[5] Powell, K. Biology from Scratch. *Nature* **2018**, 563, 172-175

[6] Alberts, B.; Johnson, A.; Walter, P.; Lewis, J.; Raff, M.; Roberts, K. Molecular Biology of The Cell. *Garland Science, Taylor & Francis Group* **2014**, 6th Edition

[7] Pollard, T. D.; Goldmann, R. D. Overview of the Cytoskeleton from an Evolutionary Perspective. *Cold Spring Harb. Perspect. Biol.* **2018**, 10:a030288

[8] Svitkina, T. The Actin Cytoskeleton and Actin-based Motility. *Cold Spring Harb. Perspect. Biol.* **2018**, 10:a018267

[9] Jones, J. C. R.; Kam, C. Y.; Harmon, R. M.; Woychek, A. V.; Hopkinson, S. B.; Green, K. J. Intermediate Filaments and the Plasma Membrane. *Cold Spring Harb. Perspect. Biol*. **2017**, 9:a025866

[10] Sweeney, H. L.; Hammers, D. W. Muscle Contraction. *Cold Spring Harb. Perspect. Biol*. **2018**, 10(2):a023200.

[11] Hermann, H.; Aebi, U. Intermediate filaments: Structure and assembly. *Cold Spring Harb. Perspect. Biol*. **2016**, 8: a018242.

[12] Hartmann, M. A.; Spudich, J. A. The myosin superfamily at a glance. *Journal of Cell Science* **2012**, 125, 1627-1632

[13] Vincente-Manzanares, M.; Ma, X.; Adelstein, R. S.; Horwitz, A. R. Non-muscle myosin II takes centre stage in cell adhesion and migration. *Nat Rev. Mol. Cell Biol*. **2009**, 11, 778–790

[14] Cooper, G. M. The Cell: A Molecular Approach. *Sunderland (MA): Sinauer Associates*, **2000**, 2nd Edition

[15] Kaur, R.; Kaur, G.; Kaur Gill, R.; Soni, R.; Bariwal, J. Recent developments in tubulin polymerization inhibitors: An overview. *European Journal of Medicinal Chemistry* **2014**, 87, 89-124

[16] Ding, Y.; Wu, F.; Tan, C. Synthetic Biology: A Bridge between Artificial and Natural Cells. *Life* **2014**, 4(4), 1092-1116

[17] Nakanishi, T.; Fukushima, S.; Okamoto, K.; Suzuki, M.; Matsumura, Y.; Yokoyama, M.; Okano, T.; Sakurai, Y.; Kataoka, K. J. Development of the polymer micelle carrier system for doxorubicin. *Control. Release* **2001**, 74, 295-302

[18] de Menezes, D. E. L.; Pilarski, L. M.; Allen, T. M. In vitro and in vivo targeting of immunoliposomal doxorubicin to human B-cell lymphoma. *Cancer Res*. **1998**, 58, 3320-3330

[19] Chang, T. M. S. Semipermeable Microcapsules. *Science* **1964**, 146, 524-525

[20] Chang T. M. S. Artificial Cells for Blood Substitutes, Enzyme Therapy, Cell Therapy and Drug Delivery. In: Nedović V., Willaert R. (eds) *Applications of Cell Immobilisation Biotechnology. Focus on Biotechnology* **2005**, vol 8B. Springer, Dordrecht

[21] Chang, T. M. S. Artificial cells with emphasis on cell encapsulation of genetically engineered cells. A*rtif. Organs* **1998**, 22, 958-965

[22] Bruni, S.; Chang, T. M. S. Kinetic Analysis of UDP-Glucuronosyltransferase in Bilirubin Conjugation by Encapsulated Hepatocytes for Transplantation into Gunn Rats. *Artif. Organs* **1995**, 19, 449-457

[23] Trubetskoy, V. S. Polymeric micelles as carriers of diagnostic agents. *Adv. Drug Deliv. Rev.* **1999**, 37, 81-88

[24] Delgado, A.; Soriano, I.; Sanchez, E.; Oliva, M.; Evora, C. Radiolabelled biodegradable microspheres for lung imaging. *Eur. J. Pharm. Biopharm*. **2000**, 50, 227-236

[25] Chang, T. M. S. ARTIFICIAL CELL evolves into nanomedicine, biotherapeutics, blood substitutes, drug delivery, enzyme/gene therapy, cancer therapy, cell/stem cell therapy, nanoparticles, liposomes, bioencapsulation, replicating synthetic cells, cell encapsulation/scaffold, biosorbent/immunosorbent haemoperfusion/plasmapheresis, regenerative medicine, encapsulated microbe, nanobiotechnology, nanotechnology. *Artificial Cells, Nanomedicine and Biotechnology* **2019**, 47, 997-1013

[26] Bershadsky, A. D.; Kozlov, M. M. Crawling cell locomotion revisited. *PNAS* **2011**, 108, 20275-20276

[27] Xu, C.; Hu, S.; Chen, X. Artificial cells: from basic science to applications. *Mater Today (Kidlington)* **2016**, 19, 516-532

[28] Buddingh, B. C.; van Hest, J. C. M. Artificial Cells: Synthetic Compartments with Life-like Functionality and Adaptivity. *Acc. Chem. Res*. **2017**, 50, 769-777

[29] Yoo J.-W.; Irvine, D. J.; Discher, D. E.; Mitragotri, S. Bio-inspired, bioengineered and biomimetic drug delivery carriers. *Nat. Rev. Drug Discov.* **2011**, 10, 521-535

[30] Rideau, E.; Dimova, R.; Schwille, P.; Wurm, F. R.; Landfester, K. Liposomes and polymersomes: a comparative review towards cell mimicking. *Chem. Soc. Rev.* **2018**, 47, 8572-8610

[31] Soppimath, K. S.; Aminabhavi, T. M.; Kulkarni, A. R.; Rudzinski, W. E. J. Biodegradable polymeric nanoparticles as drug delivery devices. *Control. Release* **2001**, 70, 1-20

[32] Chang, T. M. S. Semipermeable Microcapsules. *Science* **1964**, 146, 524-525

[33] Chang, T. M. S. "Attempts to find a method to prepare artificial hemoglobin corpuscles". *Biomater. Artif. Cells Artif. Organs.* **1988**, 16, 1-9

[34] Luisi, P. L.; Walde, P.; Oberholzer, T. Lipid vesicles as possible intermediates in the origin of life. *Curr. Opin. Colloid Interface Sci*. **1999**, 4, 33-39

[35] Browning, S. T.; Shuler, M. S. Towards the development of a minimal cell model by generalization of a model of Escherichia coli: Use of dimensionless rate parameters. *Biotechnol. Bioeng.* **2001**, 76, 187-192

[36] Lachance, J.-C.; Rodrigue, S.; Palsson, B. O. Synthetic biology: Minimal cells, maximal knowledge. *eLife* **2019**; 8: e45379

[37] Rasmussen, S.; Chen, L.; Nilsson, M.; Abe, S. Bridging nonliving and living matter. *Artif. Life* **2003**, 9, 269-316

[38] Tamate, R.; Ueki, T.; Yoshida, R. Evolved Colloidosomes Undergoing Cell-like Autonomous Shape Oscillations with Buckling. *Angew.Chem.* **2016**,128,5265–5269

[39] Rodríguez-Arco, L.; Li, M.; Mann, S. Phagocytosis-inspired behaviour in synthetic protocell communities of compartmentalized colloidal objects. *Nature Materials* **2017**, 16, 857-864

[40] Langecker, M.; Arnaut, V.; Martin, T. G.; List, J.; Renner, S.; Mayer, M.; Dietz, H.; Simmel, F. C. Synthetic Lipid Membrane Channels Formed by DNA Nanostructures. *Science* **2012**, 338, 932-936

[41] Czogalla, A.; Franquelim, H. G.; Schwille, P. DNA Nanostructures on Membranes as Tools for Synthetic Biology. *Biophysical Journal* **2016**, 110, 1698–1707

[42] Mahinroosta, M.; Farsangi, Z. J.; Allahverdi, A.; Shakoori, Z. Hydrogels as intelligent materials: A brief review of synthesis, properties and applications. *Materials Today Chemistry* **2018**, 8, 42-55

[43] Erol, O.; Pantula, A.; Liu, W.; Gracias, D. H. Transformer Hydrogel: A Review. *Adv. Mater. Technol*. **2019**, 4, 1900043

[44] Anisha, S.; Kumar, S. P.; Kumar, G. V.; Garima, G. Hydrogels: a review. *Int. J. Pharmaceut. Sci. Rev. Res.* **2010**, 4, 97-105

[45] Mehrdad, H.; Amir, A.; Pedram, R. Hydrogel nanoparticles in drug delivery. *Adv. Drug Deliv. Rev.* **2009**, 60, 1638-1649

[46] Van der Linden, H. J.; Herber, S.; Olthuis, W.; Bergveld, P. Patterned dual pH responsive core shell hydrogels with controllable swelling kinetics and volume. *Analyst* **2003**, 128, 325-331

[47] Ling, Z.; Kuifeng, L.; Wenqian, X.; Li, Z.; Yumei, X.; Hongsong, F.; Zhang, X. Preparation of collagen-chondroitin sulfate-hyaluronic acid hybrid hydrogel scaffolds and cell compatibility in vitro. *Carbohydr. Polym.* **2011**, 84, 118-125

[48] Justin, S. M.; David, F. W. Hydrogels in Regenerative Medicine. Principles of Regenerative Medicine, *Academic Press (San Diego)* **2011**, 2nd Edition

[49] Panprung, S.; Uracha, R.; Pitt, S. Preparation and characterization of asiaticosid-loaded alginate films and their potential for use as effectual wound dressings. *Carbohydr. Polym.* **2011**, 83, 1457-1469

[50] Otero, T. F.; Sansinena, J. M. Soft and wet conducting polymers for artificial muscles. *Adv. Mater.* **1998**, 10, 491-494

[51] Warren, D. S.; Sutherland, S. P. H.; Kao, J. Y.; Weal, G. R.; Mackay, S. M. The Preparation and Simple Analysis of a Clay Nanoparticle Composite Hydrogel. *J. Chem. Educ.* **2017**, 94, 1772−1779

[52] Ahmed, E. M. Hydrogel: Preparation, characterization, and applications: A review. *Journal of Advanced Research* **2015**, 6, 105-121

[53] Cai, W.; Gupta, R. B. Thermosensitive and ampholytic hydrogels for salt solution. *J. Appl. Polym. Sci.* **2003**, 88, 2032-2037

[54] Takashi, L.; Hatsumi, T.; Makoto, M.; Takashi, I.; Takehiko, G.; Shuji, S. Synthesis of porous poly(N-isopropylacrylamide) gel beads by sedimentation polymerization and their morphology. *J. Appl. Polym. Sci.* **2007**,104, 842-850

[55] Yang, L.; Chu, J.S.; Fix, J. A. Colon-specific drug delivery: new approaches and in vitro/in vivo evaluation. *Int. J. Pharm.* **2002**, 235, 1-15

[56] Maolin, Z.; Jun. L.; Min, Y.; Hongfei, H. The swelling behaviour of radiation prepared semi-interpenetrating polymer networks composed of polyNIPAAm and hydrophilic polymers. *Radiat. Phys. Chem.* **2000**, 58, 397-400

[57] Hacker, M. C.; Mikos, A. G. Synthetic polymers. Principles of Regenerative Medicine, *Academic Press (San Diego)* **2011**, 2nd Edition

[58] Zhao, W.; Jin, X.; Cong, Y.; Liu, Y.; Fu, J. Degradable natural polymer hydrogels for articular cartilage tissue engineering. *J. Chem. Technol. Biotechnol*. **2013**, 88, 327-339

[59] Ebdon, J. R. Developments in polymerization. New Methods of Polymer Synthesis. *Blackie Academic & Professional* **1991**

[60] Cowie, J. M. G.; Arrighi, V. Polymers: Chemistry and Physics of Modern Materials. *Scotland: CRC Press* **2007**, 3rd Edition

[61] Hill, A. F. π-Coordination of C-C multiple bonds. Organotransition Metal Chemistry. *New York: Wiley-InterScience* **2002**, 1st Edition

[62] Echeverria, C.; Fernandes, S. N.; Godinho, M. H.; Borges, J. P.; Soares, P. I. P. Functional Stimuli-Responsive Gels: Hydrogels and Microgels. *Gels* **2018**, 54, 151-187

[63] Dai, S.; Ravi, P.; Tam, K. C. pH-Responsive polymers: synthesis, properties and applications. *Soft Matter* **2008**, 4, 435-449

[64] Davis, D. A.; Hamilton, A.; Yang, J.; Cremar, L. D.; Van Gough, D.; Potisek, S. L.; Ong, M. T.; Braun, P. V.; Martínez, T. J.; White, S. R.; Moore, J. S.; Sottos, N. R. Force-induced Activation of Covalent Bonds in Mechanoresponsive Polymeric materials. *Nature* **2009**, 459, 68-72

[65] Tanaka, T.; Nishio, I.; Sun, S. T.; Ueno-Nishio, S. Collapse of Gels in an Electric Field. *Science* **1982**, 218, 467-469

[66] Thévenot, J.; Oliveira, H.; Sandre, O.; Lecommandoux, S. Magnetic responsive polymer composite materials. *Chem. Soc. Rev.* **2013**, 42, 7099-7116

[67] Irie, M. Properties and applications of photoresponsive polymers. *Pure Appl. Chem.* **1990**, 62, 1595-1502

[68] Heskins, M.; Guillet, J. E. Solution Properties of Poly(N-isopropylacrylamide). *J. Macromol. Sci. Chem* **1968**, 2, 1441-1455

[69] Zourob, M.; Ong, K. G.; Zeng, K. F.; Mouffouk, F.; Grimes, C. A. A wireless magnetoelastic biosensor for the direct detection of organophosphorus pesticides. *Analyst* **2007**, 132, 338-343

[70] Simoes, S.; Figueiras, A.; Francisco, V. Modular hydrogels for drug delivery. *J. Biomater. Nanobiotechnol*. **2012**, 3, 185-199

[71] van der Linden, H.; Westerweel, J. Temperature-sensitive Hydrogels. Encyclopedia of Microfluidics and Nanofluidics. *Springer Science + Business Media New York* **2014**

[72] Niskanen, J.; Tenhu, H. How to manipulate the upper critical solution temperature (UCST)? *Polym. Chem.* **2017**, 8, 220-232

[73] McNaught, A. D.; Wilkinson, A. IUPAC. Compendium of Chemical Terminology. *Blackwell Scientific Publications* **1997**, 2nd Edition ("Gold book")

[74] Zhang, Q.; Weber, C.; Schubert, U. S.; Hoogenboom, R. Thermoresponsive polymers with lower critical solution temperature: from fundamental aspects and measuring techniques to recommended turbidimetry conditions. *Mater. Horiz.* **2017**, 4, 109-116

[75] Bischofberger, I.; Trappe, V. New aspects in the phase behaviour of poly-N-isopropyl acrylamide: systematic temperature dependent shrinking of PNiPAM assemblies well beyond the LCST. *Scientific Reports* **2015**, 5, 15520-15530

[76] Zhang, J.; Pelton, R.; Deng, Y. Temperature-Dependent Contact Angles of Water on Poly(N-isopropylacrylamide) Gels. *Langmuir* **1995**, 11, 2301-2302

[77] Tauer, K.; Gau, D.; Schulze, S.; Völkl, A.; Dimova, R. Thermal property changes of poly(N-isopropylacrylamide) microgel particles and block copolymers. *Colloid. Polym. Sci.* **2009**, 287, 299-312

[78] Islam, M. R.; Ahiabu, A.; Li, X.; Serpe, M. J. Poly (N-isopropylacrylamide) Microgel-Based Optical Devices for Sensing and Biosensing. *Sensors (Basel)* **2014**, 14, 8984-8995

[79] Cao, M.; Wang, Y.; Hu, X.; Gong, H.; Li, R.; Cox, H.; Zhang, J.; Waigh, T. A.; Xu, H.; Lu, J. R. Reversible Thermoresponsive Peptide–PNIPAM Hydrogels for Controlled Drug Delivery. *Biomacromolecules* **2019**, 20, 3601-3610

[80] Park, N.; Kim, J. Hydrogel-Based Artificial Muscles: Overview and Recent Progress. *Adv. Intell. Syst.* **2020**, 2, 1900135

[81] Lee, E.; Kim, D.; Kim, H.; Yoon, J. Photothermally driven fast responding photo-actuators fabricated with comb-type hydrogels and magnetite nanoparticles. *Scientific Reports* **2015**, 5, 15124-15132

[82] Liu, J.; Weizhong, X.; Kuang, Z.; Dong, P.; Yao, Y.; Wu, H.; Liu, A.; Ye, F. Gradient porous PNIPAM-based hydrogel actuators with rapid response and flexibly controllable deformation. *J. Mater. Chem. C* **2020**, 8, 12092-12099

[83] Kim, H.; Kim, K.; Lee, S. J. Nature-inspired thermo-responsive multifunctional membrane adaptively hybridized with PNIPAm and PPy. *NPG Asia Materials* **2017**, 9, 445-454

[84] Kratz, K.; Hellweg, T.; Eimer, W. Influence of charge density on the swelling of colloidal poly(Nisopropylacrylamide-co-acrylic acid) microgels. *Colloid Surf. A* **2000**, 170, 137-149

[85] Debord, J. D.; Lyon, L. A. Synthesis and characterization of pH-responsive copolymer microgels with tunable volume phase transition temperatures. *Langmuir* **2003**, 19, 7662-7664

[86] Culver, H. R.; Sharma, I.; Wechsler, M. E.; Anslyn, E. V.; Peppas, N. A. Charged poly(N-isopropylacrylamide) nanogels for use as differential protein receptors in a turbidimetric sensor array. *Analyst* **2017**, 142, 3183-3193

[87] Zhou, S. Q.; Chu, B. Synthesis and volume phase transition of poly(methacrylic acid-co-N-isopropylacrylamide) microgel particles in water. *J. Phys. Chem. B* **1998**, 102, 1364-1371

[88] Khan, A.; Alhoshan, M. Preparation and characterization of pH-responsive and thermoresponsive hybrid microgel particles with gold nanorods. *J. Polym. Sci. A* **2013**, 51, 39-46

[89] Liu, Y. Y.; Liu, X. Y.; Yang, J. M.; Lin, D. L.; Chen, X.; Zha, L. S. Investigation of Ag nanoparticles loading temperature responsive hybrid microgels and their temperature controlled catalytic activity. *Colloid Surf. A* **2012**, 393, 105-110

[90] Chen, T.; Cao, Z.; Guo, X.; Nie, J.; Xu, J.; Fan, Z.; Du, B. Preparation and characterization of thermosensitive organic–inorganic hybrid microgels with functional Fe3O4 nanoparticles as crosslinker. *Polymer* **2011**, 52, 172-179

[91] Regmi, R.; Bhattarai, S. R.; Sudakar, C.; Wani, A. S.; Cunningham, R.; Vaishnava, P. P.; Naik, R.; Oupicky, D.; Lawes, G. Hyperthermia controlled rapid drug release from thermosensitive magnetic microgels. *J. Mater. Chem.* **2010**, 20, 6158-6163

[92] Li, Z. B.; Chen, T. Y.; Nie, J. J.; Xu, J. T.; Fan, Z. Q.; Du, B. Y. P(Nipam-co-Tmspma)/silica hybrid microgels: Structures, swelling properties and applications in fabricating macroporous silica. *Mater. Chem. Phys.* **2013**, 138, 650-657

[93] Karg, M.; Wellert, S.; Prevost, S.; Schweins, R.; Dewhurst, C.; Liz-Marzan, L. M.; Hellweg, T. Well defined hybrid PNIPAM core-shell microgels: Size variation of the silica nanoparticle core. *Colloid Polym. Sci*. **2011**, 289, 699-709

[94] Amendola, V.; Pilot, R.; Frasconi, M.; Maragò, O. M.; Iatì, M. A. Surface plasmon resonance in gold nanoparticles: a review. *J. Phys.: Condens. Matter* **2017**, 29, 203002

[95] Maier, S. A. Plasmonics: Fundamentals and Applications. *Springer Science + Business Media LLC* **2007**

[96] Kelly, K. L.; Coronado, E.; Zhao, L. L.; Schatz, G. C. The Optical Properties of Metal Nanoparticles: The Influence of Size, Shape, and Dielectric Environment. *J. Phys. Chem. B* **2003**, 107, 668-677

[97] Mayer, K. M.; Hafner, J. H. Localized surface plasmon resonance sensors. *Chem. Rev.* **2011**, 111, 3828-3857

[98] Yang, Y.; Chen, M.; Wang, B.; Wang, P.; Liu, Y.; Zhao, Y; Li, K.; Song, G.; Zhang, X. B.; Tan, W. NIR-II Driven Plasmon-Enhanced Catalysis for a Timely Supply of Oxygen to Overcome Hypoxia-Induced Radiotherapy Tolerance. *Angew. Chem. Int. Ed Engl.* **2019**, 58, 15069-15075

[99] Dodekatos, G.; Schünemann, S.; Tüysüz, H. Surface Plasmon-Assisted Solar Energy Conversion. *Top Curr. Chem.* **2016**, 371, 215-52

[100] Zijlstra, P.; Chon, J. W.; Gu, M. Five-dimensional optical recording mediated by surface plasmons in gold nanorods. *Nature* **2009**, 459, 410-413

[101] Singh, P.; Pandit, S.; Mokkapati, V. R. S. S.; Garg, A.; Ravikumar, V.; Mijakovic, I. Gold Nanoparticles in Diagnostics and Therapeutics for Human Cancer. *Int. J. Mol. Sci.* **2018**, 19, 1979

[102] Darweesh, R. S.; Ayoub, N. M.; Nazzal, S. Gold nanoparticles and angiogenesis: molecular mechanisms and biomedical applications. Int. J. Nanomedicine 2019, 14, 7643-7663

[103] Daraee, H.; Eatemadi, A.; Abbasi, E.; Fekri Aval, S.; Kouhi, M.; Akbarzadeh, A. Application of gold nanoparticles in biomedical and drug delivery. *Artif. Cells. Nanomed. Biotechnol.* **2016**, 44, 410-422

[104] Golchin, K.; Golchin, J.; Ghaderi, S.; Alidadiani, N.; Eslamkhah, S.; Eslamkhah, M.; Davaran, S.; Akbarzadeh, A. Gold nanoparticles applications: from artificial enzyme till drug delivery. *Artif. Cells Nanomed. Biotechnol.* **2018**, 46, 250-254

[105] Butler, H. J.; Fogarty, S. W.; Kerns, J. G.; Martin-Hirsch, P. L.; Fullwood, N. J.; Martin, F. L. Gold nanoparticles as a substrate in bio-analytical near-infrared surface-enhanced Raman spectroscopy. *Analyst* **2015**, 140, 3090-3097

[106] Convery, N.; Gadegaard, N. 30 years of microfluidics. *Micro and Nano Engineering* **2019**, 2, 76-91

[107] Terry, S. C.; Herman, J. H.; Angell, J. B. A gas chromatographic air analyzer fabricated on a silicon wafer. *IEEE Trans Electron Devices* **1979**, 26, 1880-1886

[108] McDonald, J. C.; Duffy, D. C.; Anderson, J. R.; Chiu, D. T.; Wu, H.; Schueller, O. J. A.; Whitesides, G. M. Fabrication of microfluidic systems in poly(dimethylsiloxane). *Electrophoresis* **2000**, 21, 27-40

[109] Lorenz, H.; Despont, M.; Fahrni, N.; Brugger, J.; Vettiger, P.; Renaud, P. High-aspect ratio, ultrathick, negative-tone near-UV photoresist and its applications for MEMS. *Sensors Actuators A Phys*. **1998**, 64, 33-39

[110] Manz, A.; Harrison, D. J.; Verpoorte, E. M. J.; Fettinger, J. C.; Paulus, A.; Ludi, H.; Widmer, H. M. Planar chips technology for miniaturization and integration of separation techniques into monitoring systems. Capillary electrophoresis on a chip. *Journal of Chromatography* **1992**, 593, 253-258

[111] Bhatia, S. N.; Ingber, D. E. Microfluidic organs-on-chips. *Nat. Biotechnol.* **2014**, 32, 760-772

[112] Demello, A. J. Control and detection of chemical reactions in microfluidic systems. *Nature* **2006**, 442, 394-402

[113] Valencia, P. M.; Pridgen, E. M.; Rhee, M.; Langer, R.; Farokhzad, O. C.; Karnik, R. Microfluidic platform for combinatorial synthesis and optimization of targeted nanoparticles for cancer therapy. *ACS Nano* **2013**, 7, 10671-10680

[114] Chin, C. D.; Laksanasopin, T.; Cheung, Y. K.; Steinmiller, D.; Linder, V.; Parsa, H.; Wang, J.; Moore, H.; Rouse, R.; Umviligihozo, G.; Karita, E.; Mwambarangwe, L.; Braunstein, S. L.; van de Wijgert, J.; Sahabo, R.; Justman, J. E.; El-Sadr, W.; Sia, S. K. Microfluidics-based diagnostics of infectious diseases in the developing world. *Nat. Med.* **2011**, 17, 1015-1019

[115] Khan, I. U.; Serra, C. A.; Anton, N.; Vandamme, T. F. Production of nanoparticle drug delivery systems with microfluidics tools. *Expert Opin. Drug. Deliv.* **2015**, 12, 547-562

[116] Bhatia, S. N.; Ingber, D. E. Microfluidic organs-on-chips. *Nat. Biotechnol.* **2014**, 32, 760-772

[117] Aryasomayajula, A.; Bayat, P.; Rezai, P.; Selvaganapathy, P. R. Microfluidic Devices and Their Applications. Springer Handbook of Nanotechnology. *Springer-Verlag GmbH Germany* **2017**, 4th Edition

[118] Sackmann, E. K., Fulton, A. L.; Beebe, D. J. The present and future role of microfluidics in biomedical research. *Nature* **2014**, 507, 181–189

[119] Squires, T. M.; Quake, S. R. Microfluidics: Fluid physics at the nanoliter scale. *Rev. Mod. Phys*. **2005**, 77, 977-1026

[120] Reynolds, O. An experimental investigation of the circumstances which determine whether the motion of water shall be direct or sinuous, and of the law of resistance in parallel channels. *Philos. Trans. R. Soc. London.* **1883**, 174, 935-982

[121] Hardt, S.; Schönfeld, F. Microfluidics: Fundamentals and Engineering Concepts. Microfluidic Technologies for Miniaturized Analysis Systems. *Springer Science + Business Media, LLC* **2007**, 1-58

[122] Tabeling, P. Introduction to Microfluidics. *Oxford University Press* **2005**, 1st Edition

[123] Berry, J. D.; Neeson, M. J.; Dagastine, R. R.; Chan, D. Y. C.; Tabor, R. F. Measurements of surface and interfacial tension using pendant drop tensiometry. *J. Colloid Interface Sci*. **2015**, 454, 226-237

[124] Eggers, J. Nonlinear dynamics and breakup of free-surface flows. *Rev. Mod. Phys.* **1997**, 69, 865-929

[125] Roach, L. S., Song, H.; Ismagilov, R. F. Controlling nonspecific protein adsorption in a plug-based microfluidic system by controlling interfacial chemistry using fluorous-phase surfactants. *Anal. Chem.* **2005**, 77, 785-796

[126] Jin, F., Balasubramaniam, R.; Stebe, K. J. Surfactant adsorption to spherical particles: The intrinsic length scale governing the shift from diffusion to kinetic-controlled mass transfer. *J. Adhes.* **2004**, 80, 773-796

[127] Kamalakshakurup, G.; Vallejo, D.; Lee, A. Microfluidic Micro/Nano Droplets. Springer Handbook of Nanotechnology. *Springer-Verlag GmbH Germany* **2017**, 4th Edition

[128] Bibette, J.; Leal-Calderon, F.; Poulin, P. Emulsions: basic principles. *Rep. Prog. Phys.* **1999**, 62, 969-1033

[129] Dai, B.; Leal, L. G. The mechanism of surfactant effects on drop coalescence. *Phys. Fluids* **2008**, 20, 040802

[130] Theberge, A.; Courtois, F.; Schaerli, Y.; Fischlechner, M.; Abell, C.; Hollfelder, F.; Huck, W. Mikrotröpfchen in Mikrofluidiksystemen: eine Technik für Entdeckungen in der Chemie und Biologie. *Angewandte Chemie* **2010**, 122, 5982-6005

[131] Roach, L. S.; Song, H.; Ismagilov, F. Controlling Nonspecific Protein Adsorption in a Plug-Based Microfluidic System by Controlling Interfacial Chemistry Using Fluorous-Phase Surfactants. *Anal. Chem.* **2005**, 77, 785-796

[132] Bibette, J.; Leal-Calderon, F. Surfactant-stabilized emulsions. *Current Opinion in Colloid & Interface Science* **1996**, 1, 746-751

[133] Tadros, T. Gibbs Adsorption Isotherm. Encyclopedia of Colloid and Interface Science. *Springer, Berlin, Heidelberg* **2013**, https://doi.org/10.1007/978-3-642-20665-8_97

[134] Diamant, H.; Ariel, G.; Andelman, D. Kinetics of Surfactant Adsorption: The Free Energy Approach. *Colloid Surf. A* **2001**, 259, 183-185

[135] Nagarajan, R., Ruckenstein, E.; Nagarajan, R. Critical micelle concentration. A transition point for micellar size distribution. *J. Phys. Chem.* **1975**, 79, 2622-2626

[136] Holt, D. J.; Payne, R. J.; Chow, W. Y.; Abell, C. Fluorosurfactants for microdroplets: Interfacial tension analysis. *Journal of Colloid and Interface Science* **2010**, 350, 205-211

[137] Goodman, S. R. Cell (biology). *AccessScience* **2019**. Retrieved November 4, 2020, from https://doi.org/10.1036/1097-8542.116000

[138] Bearer, E. L. Role of Actin Polymerization in Cell Locomotion: Molecules and Models. *Am. J. Respir. Cell Mol. Biol.* **1993**, 8, 582-591

[139] Lodish, H.; Berk, A.; Zipursky ,S. L. The Dynamics of Actin Assembly. Molecular Cell Biology. *New York: W. H. Freeman* **2000**, 4th Edition, Section 18.2

[140] Zaidel-Bar, R.; Zhenhuan, G.; Luxenburg, C. The contractome – a systems view of actomyosin contractility in non-muscle cells. *Journal of Cell Science* **2015**, 128, 2209-2217

[141] Sanghavi-Shah, R.; Weber, G. F. Intermediate Filaments at the Junction of Mechanotransduction, Migration, and Development. *Front. Cell Dev. Biol.* **2017**, 5:81, 10.3389

[142] Gardel, M. L.; Schneider, I. C.; Aratyn-Schaus, Y.; Waterman, C. M. Mechanical Integration of Actin and Adhesion Dynamics in Cell Migration. *Annu. Rev. Cell Dev. Biol.* **2010**, 26, 315-333

[143] Raftopoulou, M.; Hall, A. Cell migration: Rho GTPases lead the way. *Dev. Biol.* **2004**, 265, 23-32

[144] Bueso, F. Y.; Tangney, M. Synthetic Biology in the Driving Seat of the Bioeconomy. *Trends in Biotechnology* **2017**, 35, 373-378

[145] Elani, Y. Construction of membrane-bound artificial cells using microfluidics: a new frontier in bottom-up synthetic biology. *Biochem. Soc. Trans.* **2016**, 44, 723-730

[146] Supramaniam, P.; Ces, O.; Salehi-Reyhani, A. Microfluidics for Artificial Life: Techniques for Bottom-Up Synthetic Biology. *Micromachines (Basel)* **2019**, 10(5):299

[147] Majumder, S.; Liu, A. P. Bottom-up synthetic biology: modular design for making artificial platelets. *Phys. Biol.* **2017**, 15(1):013001

[148] Yang, K.; Han, Q.; Chen, B.; Zheng, Y.; Zhang, K.; Li, Q.; Wang, J. Antimicrobial hydrogels: promising materials for medical application. *Int. J. Nanomedicine* **2018**, 13, 2217-2263

[149] Yang, J.; Zhang, Y. S.; Yue, K.; Khademhosseini, A. Cell-laden hydrogels for osteochondral and cartilage tissue engineering. *Acta Biomater*. **2017**, 57, 1-25

[150] Vasile, C.; Pamfil, D.; Stoleru, E.; Baican, M. New Developments in Medical Applications of Hybrid Hydrogels Containing Natural Polymers. *Molecules* **2020**, 25(7):1539

[151] Cliffe, A.; Doupé, D. P.; Song, H.; Lim, I. K. H.; Ong, K. H.; Cheng, L.; Yu, W. Quantitative 3D analysis of complex single border cell behaviors in coordinated collective cell migration. *Nature Communications* **2017**, 8, 14905-14918

[152] Trepat, X.; Chen, Z.; Jacobson, K. Cell Migration. *Comprehensive Physiology* **2012**, 2, 2369–2392

[153] Geiger, B.; Spatz, J. P.; Bershadsky, A. D. Enviromental sensing through focal adhesions. *Nature Reviews Molecular Cell Biology* **2009**, 10, 21-33

[154] Laboratory Water. Its Importance and Applications. *National Institutes of Health* **2003**,
https://www.orf.od.nih.gov/TechnicalResources/Documents/DTR%20White%20Papers/Laboratory%20Water-Its%20Importance%20and%20Application-March-2013_508.pdf

[155] Holtze, C.; Rowat, A. C.; Agresti, J. J.; Hutchison, J. B.; Angilè, F. E.; Schmitz, C. H. J.; Köster, S.; Duan, H.; Humphry, K. J.; Scanga, R. A.; Johnson, J. S.; Pisignano, D.; Weitz, D. A. Biocompatible Surfactants for Water-In-Fluorocarbon Emulsions. *Lab Chip* **2008**, 8, 1632-1639

[156] Scarabelli, L.; Sánchez-Iglesias, A.; Pérez-Juste, J.; Liz-Marzán, L. M. A „“Tips and Tricks“ Practical Guide to the Synthesis of Gold Nanorods. *J. Phys. Chem. Lett.* **2015**, 6, 4270-4279

[157] Frey, C.; Göpfrich, K.; Pashapour, S.; Platzman, I.; Spatz, J. P. Electrocoalescence of Water-in-oil Droplets with a Continuous Aqueous Phase: Implementation of Controlled Content Release. *ACS Omega* **2020** 13, 7529-7536

[158] Schindelin, J.; Arganda-Carreras, I.; Frise, E.; Kaying, V.; Longair, M.; Pietzsch, T.; Preibisch, S.; Rueden, C.; Saalfeld, S.; Schmid, B.; Tinevez, J.-Y.; White, D. J.;

Hartenstein, V.; Eliceiri, K.; Tomancak, P.; Cardona, A. Fiji: an open-source platform for biological-image analysis. *Nature Methods* **2012**, 9, 676-682

[159] OriginPro, "Version 2019". *OriginLab Corporation*, Northampton, MA, USA

[160] Hu, Z. J.; Hou, S.; Ji, Y. L.; Wen, T.; Liu, W. Q.; Zhang, H.; Shi, X. W.; Yan, J.; Wu, X. C. Fast characterization of gold nanorods ensemble by correlating its structure with optical extinction spectral features. *AIP Advances* **2014**, 4, 117137-117148

[161] Haller, B.; Göpfrich, K.; Schröter, M.; Janiesch, J.-W.; Platzman, I.; Spatz, J. P. Charge-controlled microfluidic formation of lipid-based single- and multicompartment systems. *Lab Chip* **2018**, 18, 2665-2674

[162] Abate, A. R., Hung, T., Mary, P., Agresti, J. J.; Weitz, D. A. High-throughput injection with microfluidics using picoinjectors. *Proc. Natl. Acad. Sci*. **2010**, 107, 19163–19166

[163] Pardee, J. D.; Aspudich, J. Purification of muscle actin. *Methods in Enzymology* **1982**, 85, 164-181

[164] Kron, S, J.; Toyoshima, Y. Y.; Uyeda, T. Q. P.; Spudich, J. A. Assays for actin sliding movement over myosin-coated surfaces. *Methods in Enzymology* **1991**, 196, 399-416

[165] Chugh, P.; Paluch, E. K. The actin cortex at a glance. *Journal of Cell Science* **2018**, 131, jcs186254

[166] Lepore, S. D.; He, Y. Use of Sonication for the Coupling of Sterically Hindered Substrates in the Phenolic Mitsunobu Reaction. *J. Org. Chem*. **2003**, 68, 8261-8263

[167] Gottlieb, H. E.; Kotlyar, V.;Nudelman, A. NMR Chemical Shifts of Common Laboratory Solvents as Trace Impurities. *J. Org. Chem.* **1997**, 62, 7512–7515

[168] Gruner, P.; Riechers, B.; Semin, B.; Lim, J.; Johnston, A.; Short, K.; Baret, J.-C. Controlling molecular transport in minimal emulsions. *Nat. Commun.* **2016**, 7, 10392

[169] Berry, J. D.; Neeson, M. J.; Dagastine, R. R.; Chan, D. Y. C.; Tabor, R. F. Measurement of Surface and Interfacial Tension Using Pendant Drop Tensiometry. *Journal of Colloid and Interface Science* **2015**,454, 226–237

[170] Abbott, L. J.; Tucker, A. K.; Stevens, M. J. Single Chain Structure of a Poly(N-isopropylacrylamide) Surfactant in Water. *J. Phys. Chem. B* **2015**, 119, 3837−3845

[171] Eötvös, R. Ueber den Zusammenhang der Oberflächenspannung der Flüssigkeiten mit ihrem Molecularvolumen. *Ann. Der Physik* **1886**, 27, 448-459

[172] Palit, S. R. Thermodynamic Interpretation of the Eotvos Constant. *Nature* **1956**, 177, 1180

[173] Ye, X.; Jin, L.; Caglayan, H.; Chen, J.; Xing, G.; Zheng, C.; Doan-Nguyen, V.; Kang, Y.; Engheta, N.; Kagan, C. R.; Murray, C. B. Improved Size-Tunable Synthesis of Monodisperse Gold Nanorods through the Use of Aromatic Additives. *ACS Nano* **2012**, 6, 2804-2817

[174] Bischofberger, I.; Trappe, V. New aspects in the phase behaviour of poly-N-isopropyl acrylamide: systematic temperature dependent shrinking of PNiPAM assemblies well beyond the LCST. *Scientific Reports* **2015**, 5, 15520-15530

[175] Zarzyka, I.; Pyda, M.; Di Lorenzo, M. L. Influence of crosslinker and ionic comonomer concentration on glass transition and demixing/mixing transition of copolymers poly(N-isopropylacrylamide) and poly(sodium acrylate) hydrogels. *Colloid Polym Sci* **2014**, 292, 485–492

[176] Kretschmer, S.; Ganzinger, K. A.; Franquelim, H. G.; Schwille, P. Synthetic cell division via membrane-transforming molecular assemblies. *BMC Biology* **2019**, 17, 43

[177] Zhang, X.-Z.; Wu, D.-Q.; Chu, C.-C. Effect of the crosslinking level on the properties of temperature-sensitive poly(N-isopropylacrylamide) hydrogels. *Journal of Polymer Science: Part B: Polymer Physics* **2003**, 41, 582-593

[178] Wang, J.-Q.; He, L.-N.; Miao, C.-X. Polyethylene glycol radical-initiated oxidation of benzylic alcohols in compressed carbon dioxide. *Green Chem*. **2009**, 11, 1013-1017

[179] Bortel, E.; Hodorowicz, S.; Lamot, R. Relation Between Crystallinity Degree and Stability in Solid State of High Molecular Weight Poly(ethy1ene oxide)s. *Makromol. Chem.* **1979**,180, 2491-2498

[180] Göpfrich, K.; Haller, B.; Staufer, O.; Dreher, Y.; Mersdorf, U.; Platzman, I.; Spatz, J. P. One-Pot Assembly of Complex Giant Unilamellar Vesicle-based Synthetic Cells. *ACS Synth. Biol.* **2019**, 8, 937−947

[181] Deshmukh, S. A.; Sanakaranarayanan, S. K. R. S.; Suthar, K.; Mancini, D. C. Role of Solvation Dynamics and Local Ordering of Water in Inducing Conformational Transitions in Poly(N-isopropylacrylamide) Oligomers through the LCST. *J. Phys. Chem. B* **2012**, 116, 2651-2663

[182] Zimmels, Y. Generalized buoyancy forces in dispersions. *Journal of Applied Physics* **1990**, 68, 2007

[183] Kaplan, J. H.; Forbush, B. III; Hofman, J. F. Rapid photolytic release of adenosine 5'-triphosphate from a protected analog: utilization by the sodium:potassium pump of human red blood cell ghosts. *Biochemistry* **1978**, 17, 1929-1935

[184] Burridge, K. Focal adhesions: a personal perspective on a half century of progress. *The FEBS Journal* **2017**, 284, 3355-3361

[185] Wu, C. Focal Adhesion: A Focal Point in Current Cell Biology and Molecular Medicine. *Cell Adh. Migr.* **2007**, 1, 13-18

[186] Fallesen, T.; Roostalu, J.; Duellberg, C.; Pruessner, G.; Surrey, T. Ensembles of Bidirectional Kinesin Cin8 Produce Additive Forces in Both Directions of Movement. *Biophys. J.* **2017**, 113, 2055-2067

[187] Holt, D. J.; Payne, R. J.; Chow, W. Y.; Abell, C. Fluorosurfactants for microdroplets: Interfacial tension analysis. *Journal of Colloid and Interface Science* **2010**, 350, 205-211

[188] Shinoda, K.; Hato, M.; Hayashi, T. Physicochemical properties of aqueous solutions of fluorinated surfactants. *The Journal of Physical Chemistry* **1972**, 76, 909-914

[189] Geankopolis, C. J. Transport Processes and Separation Process Principles. *Prentice Hall Professional Technical References* **2003**, 4th Edition

[190] Stone, H. A. Introduction to Fluid Dynamics for Microfluidic Flows. CMOS Biotechnology. *Boston, MA: Springer US* **2007**, 5-30

[191] Köhler, S.; Lieleg, O.; Bausch, A. R. Rheological Characterization of the Bundling Transition in F-Actin Solutions Induced by Methylcellulose. *PLoS ONE* **2008**, 3(7): e2736

[192] Haller, B.; Jahnke, K.; Weiss, M.; Göpfrich, K.; Platzman, I.; Spatz, J. P. Autonomous Directional Motion of Actin-Containing Cell-Sized Droplets. *Adv. Intell. Syst.* **2020**, 2000190

[193] Jahnke, K.; Weiss, M.; Weber, C.; Platzman, I.; Göpfrich, K.; Spatz, J. P. Engineering Light-Responsive Contractile Actomyosin Networks with DNA Nanotechnology. *Adv. Biosys.* **2020**, 2000102

[194] Tsuji, M.; Kabir, A. Md. R.; Ito, M.; Inoue, D.; Kokado, K.; Sada, K.; Kakugo, A. Motility of Microtubules on the Inner Surface of Water-in-Oil Emulsion Droplets. *Langmuir* **2017**, 33, 12108-12113

[195] Platzman, I.; Janiesch, J.-W.; Spatz, J. P. Synthesis of Nanostructured and Biofunctionalized Water-in-Oil Droplets as Tools for Homing T Cells. *J. Am. Chem. Soc.* **2013**, 135, 3339−3342

[196] Shah, L. A.; Farooqi, Z. H.; Naeem, H.; Shah, S. H.; Siddiq, M. Synthesis and Characterization of Poly(N-isopropylacrylamide) Hybrid Microgels with different Cross-linker Contents. *J.Chem.Soc.Pak.* **2013**, 35, 1522-1529

[197] Zhang, H. T.; Hiiragi, T. Symmetry Breaking in the Mammalian Embryo. *Annual Review of Cell and Developmental Biology* **2018**, 34, 405-426

[198] Goryachev, A. B. Symmetry Breaking as an Interdisciplinary Concept Unifying Cell and Developmental Biology. *Cells* **2021**,10, 86

Abbreviations

^{1}H	Hydrogen-1-core
5-BrSA	5-bromosalicylic acid
AA	Ascorbic acid
AC	Alternating electrical field
ADP	Adenosine diphosphate
ASB	Angle selective backscattered electron
ATP	Adenosine triphosphate
AuNRs	Gold nanorods
AuS	Gold-linked surfactant
BIS	N,N‘-methylenbis(acrylamide)
Bo	Bond number
CAD	Computer-aided design
$CDCl_3$	Deuterated chloroform
CMC	Critical micellar concentration
Com.	Commercial
CS	Commercial fluorosurfactant
CTAB	Cetyltrimethylammonium bromide
D1173	Darocur 1173 (2-Hydroxy-2methyl-propiophenone)
DCM	Dichloromethane
DHB	Dihydroxybenzoic acid
DLS	Dynamic light scattering
DNA	Deoxyribonucleic acid
Dowsil™ RSN-0749	Commercial silicone-based surfactant
DTT	1,4-dithiothreitol
ECM	Extracellular matrix
EGTA	Ethylene glycolbis(aminoethyl ether)-N,N,N',N'-tetraacetic acid
ER	Endoplasmic reticulum
ESID	Electronically switchable illumination and detection module

F-actin	Filamentous actin
FA	Focal adhesion
FC-40	1,1,2,2,3,3,4,4,4-nonafluoro-N-(1,1,2,2,3,3,4,4,4-nonafluorobutyl)-N- (1,1,2,2-tetrafluoroethyl)butan-1-amine
FE	Field emission
FTIR spectroscopy	Fourier-transformed infrared spectroscopy
G-actin	Globular actin
GTP	Guanosine triphosphate
HEPES	4-(2-hydroxyethyl)-1-piperazineethanesulfonic acid
HFE7100	Methoxyperfluorobutane
HFE7500	3-ethoxyperfluoro(2-methylhexane)
HFIP	1,1,1,3,3,3-hexafluoro-2-propanol
HLB	Hydrophilic-lipophilic balance
Hz	Hertz
IFT	Interfacial tension
IR	Infrared
LC-MS	Liquid chromatography – mass spectrometry
LCST	Lower critical solution temperature
LissRhodPE	1,2-dioleoyl-sn-glycero-3-phosphoethanolamine-N-(lissamine rhodamine B sulfonyl) (ammonium salt)
MALDI	Matrix-assisted laser desorption ionization
MeOH	Methanol
mm	Millimeter
mol%	mol percent
MS	Mass spectrometry
MTOC	Microtubule-organizing center
NHS	N-hydroxy succinimide
NIPAM	N-isopropylacrylamide
nm	Nanometer
NMR	Nuclear magnetic resonance
PBS	Phosphate buffered saline
PCR	Polymerase chain reaction
PDMS	Polydimethylsiloxane

Pe	Péclet number
PEG	Polyethylene glycol
PFPE-carboxylic acid	Krytox
PNIPAM	Poly(N-isopropylacrylamide)
PNS	PNIPAM-based surfactant
POPC	1-palmitoyl-2-oleoyl-glycero-3-phosphocholine
POPG	1-palmitoyl-2-oleoyl-sn-glycero-3-phospho-(1'-rac-glycerol) (sodium salt)
ppm	Parts per million
PTFE	Polytetrafluoroethylene
Re	Reynolds number
Rho6G	Rhodamine 6G
SE	Secondary electron
SEM	Scanning electron microscopy
T	Temperature
t	Time
TEM	Transmission electron microscopy
THF	Tetrahydrofuran
TOF	Time-of-flight
T_T	Transition temperature
UCST	Upper critical solution temperature
UV	Ultraviolet
UV Vis spectroscopy	Ultraviolet visible light spectroscopy
wt%	Weight percent
µm	Micrometer

ACKNOWLEDGEMENTS

I would like to express my deep gratitude to my advisor Prof. Joachim Spatz for providing me the chance to work on this fascinating interdisciplinary topic. Without his advice and the support throughout my Ph.D, I would have never come so far. I am also grateful for all the possibilities he offered during my research: the well-equipped labs, the possibility to attend further education and training courses and the annual retreats in Antholz with inspiring scientific discussions, winter sports and enjoying the time with all the colleagues. Thanks for giving me the chance to be part of your amazing group and the freedom to develop myself.

I would like to thank Prof. Reiner Dahint for kindly accepting to review my thesis.

My sincere gratitude belongs to Dr. Ilia Platzman, project leader of the "Construction of cells"-subgroup for his great supervision, valuable discussions and his constant advice. I am grateful for all his encouragement and his well elaborated questions that were challenging but which, at the end, led to a deeper understanding of my research. Besides the scientific aspects, there was always an open ear when needed.

I would like to thank all the technicians and facilities at the MPI for Medical Research in Heidelberg and the MPI for Intelligent Systems in Stuttgart for their help and support. Especially, I would like to thank Cornelia Weber, who provided the actin and helped a lot with the actin experiments. Ulrike Mersdorf is gratefully acknowledged for performing TEM measurements of the gold nanorods. Raimund Jung, who helped a lot with safety measures in the labs. Annette Fautsch and Sabine Grünewald, who made sure that everything needed during a normal day in the lab was provided. I would like to thank Carmen Sahm for her support, advice and cheering me up in the first to years of my Ph.D. I look forward to seeing you again.

Many thanks to Jan-Willi Janiesch for introducing me to the microfluidic technology and all the help in the first year of my research. Additionally, I would also like to thank Christoph Frey for providing the microfluidic device wafers.

I want to acknowledge the best office mates someone could have: Cornelia Zapp, Martin Schröter and Yannik Dreher. Thank you for all the coffee breaks, all the discussions, your support and becoming dear friends over the years. Thanks for all the hours together, not only at work but also playing board games, bouldering, cooking or just sitting together. I will miss seeing you on a daily basis, but we can still have Zoom coffee or lunch breaks. I would like to especially thank Cornelia Zapp for proof-reading my thesis. Although our office change over the years (locally and people-wise), I am honored that you are still my office mate, even though I can talk a lot ;-). I would like to thank Martin Schröter for helping me with the MALDI and NMR measurements and for the introduction to Exit and fancy board games. I am really glad to have you in my life.

Special thanks to Dr. Rebecca Medda, who not only proof-read my thesis but was also there for me when I needed it. Thank you for your advice, your support, the many meetings and conversions and for helping me to find my way for my further professional future. Without your faith in me and your support, I would not have come so far.

I want to thank the whole Spatz group for the nice and friendly atmosphere. It was a pleasure to come to the institute every day and you have made a major contribution. I enjoyed all the lunch and coffee breaks, the cake and all the meetings and chats with you guys.

The Max Planck Society is appreciated for its general support in all aspects of the presented research.

I would like to thank my former chemistry teacher, Dr. Thomas Heinlein for supporting me. Without him, I would have never studied chemistry.

Studies have shown that friendships formed during the time at the university are deeply rooted and long-lasting, so it is not surprising that I met my best friend at university. Patrick, thank you for accompanying me throughout my entire studies. Without you, being in the lab and the lectures would not have been so much fun. Thank you for cheering me up the whole time. I am grateful and honored to have met you and although you are doing

your Ph.D in Dortmund and we do not see each other regularly, it feels the same as it did when you were still here. Thank you for this unique friendship.

I am deeply grateful to my family for all their support. My parents, thank you for allowing me to find my way and walk without having to worry because you were always there for me. My sister Sarah, thank you for always being in my team and the great support throughout all the years and hopefully also in the future.

Finally, I want to thank the most important person in my life, my husband Eric. Thank you for always being there for me. Even in difficult times, you manage to cheer me up. Your faith in me makes me stronger and without your support, I would not have achieved so much. Whatever the future may hold, I am grateful to have you by my side.